




# A critical review on the effects of process-induced porosity on the mechanical properties of alloys fabricated by laser powder bed fusion

Wen Hao Kan<sup>1,2,\*</sup> , Louis Ngai Sam Chiu<sup>1,2</sup>, Chao Voon Samuel Lim<sup>1,2</sup>, Yuman Zhu<sup>1,2</sup>, Yang Tian<sup>1,2</sup>, Derui Jiang<sup>1,2</sup>, and Aijun Huang<sup>1,2,\*</sup>

<sup>1</sup> Monash Centre for Additive Manufacturing, Monash University, Notting Hill, VIC 3168, Australia

<sup>2</sup> Department of Materials Science and Engineering, Monash University, Clayton, VIC 3800, Australia

Received: 22 October 2021

Accepted: 8 February 2022

Published online:

11 March 2022

© The Author(s) 2022

## ABSTRACT

Laser powder bed fusion (LPBF) is an emerging additive manufacturing technique that is currently adopted by a number of industries for its ability to directly fabricate complex near-net-shaped components with minimal material wastage. Two major limitations of LPBF, however, are that the process inherently produces components containing some amount of porosity and that fabricated components tend to suffer from poor repeatability. While recent advances have allowed the porosity level to be reduced to a minimum, consistent porosity-free fabrication remains elusive. Therefore, it is important to understand how porosity affects mechanical properties in alloys fabricated this way in order to inform the safe design and application of components. To this aim, this article will review recent literature on the effects of porosity on tensile properties, fatigue life, impact and fracture toughness, creep response, and wear behavior. As the number of alloys that can be fabricated by this technology continues to grow, this overview will mainly focus on four alloys that are commonly fabricated by LPBF—Ti-6Al-4 V, Inconel 718, AISI 316L, and AlSi10Mg.

## Introduction

Additive manufacturing (AM) refers to a group of technologies defined by the ability to fabricate near-net-shaped components using 3D model data by joining materials layer by layer [1, 2]. Various AM

technologies typically used for metal fabrication are shown in Fig. 1. Laser powder bed fusion (LPBF, also commonly known as selective laser melting and direct metal laser sintering [1]), with a schematic shown in Fig. 2, fabricates components by spreading metal powder across a bed/platform using a recoater (or rake), layer by layer, such that the

Handling Editor: M. Grant Norton.

Address correspondence to E-mail: wenhao.kan@monash.edu; aijun.huang@monash.edu

region(s) of interest at each powder layer is melted and fused using a high-powered laser.

Process-induced porosity remains one of the major limitations of LPBF-processed alloys. Gas pores form when gas is trapped in the molten metal as it rapidly solidifies. The gas either originates from within the powder particles (due to powder porosity or introduced from the atomization process) or from the space that surrounds them [3, 4]. When an excessively high energy input is used, the evaporation of the metal can occur which then leads to keyhole formation within the melt pool where the cavity is kept open as a result of the vapor pressure [5]. As the laser beam passes, the keyhole would collapse, and molten metal would flow into the cavity. Since solidification occurs from the bottom of the melt-pool, there is often sufficient time for trapped vapor near the top of the melt-pool to float upwards and escape before the melt-pool solidifies, but this may not be the case for vapor trapped near the bottom of the melt-pool, in which case a large, typically spherical, pore(s) will remain within the solidified melt-pool and such pores are termed keyhole pores.

Lack of fusion (LoF) pores occur when the energy input is insufficient to fully melt the current powder layer along with the prior solidified layer(s) to produce an adequate bond between them [3, 6, 7], and therefore, they are often located between scan tracks and deposited layers. While LoF pores may or may not contain unmelted powder, the presence of unmelted powder is clear evidence of LoF. The energy input, in this context, is usually expressed in terms of the volumetric laser energy density  $E_{volumetric} = P/(V \cdot h \cdot t)$  where  $E$  is the energy density,  $P$  is the laser power,  $h$  is the hatch spacing, and  $t$  is the layer thickness [8]. Occasionally, the linear laser energy density function  $E_{linear} = P/V$  is used [9]. In general,

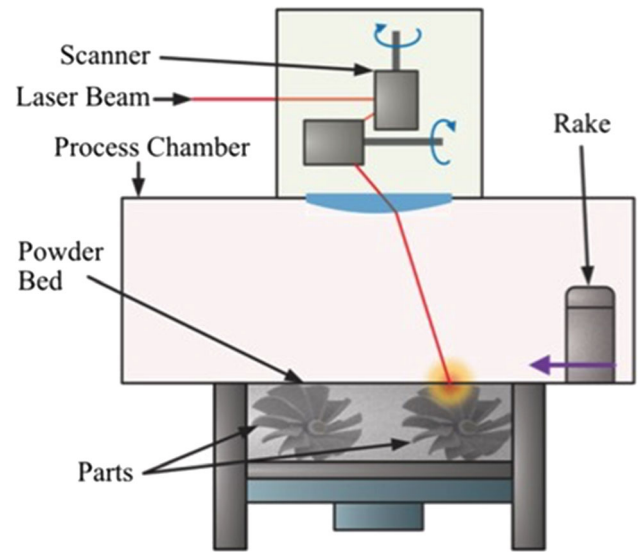
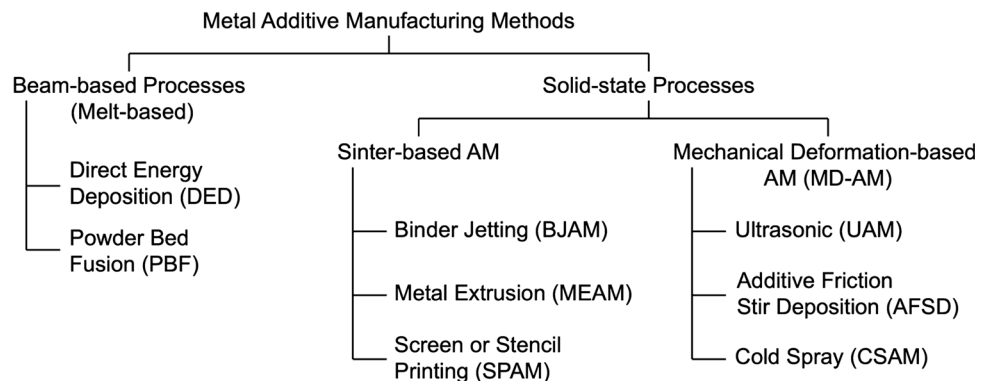


**Figure 2** Schematic of a typical laser powder bed fusion system. Reproduced with permission from [44] (Copyright 2021, Elsevier).

the three types of porosity can be distinguished by their morphology [10]. Gas pores tend to be small (< 100 μm) and spherical [3, 10]. LoF pores, on the other hand, tend to be much larger and have an irregular shape (large aspect ratio, low sphericity) [3, 10]. Keyhole pores are generally large and spherical [10]. Figure 3 illustrates how LoF and keyhole pores can be distinguishable by pore length and roundness via 2D imaging analysis. Figure 4 shows what these pores typically look like when observed in an LPBF-processed alloy.

To measure porosity in an LPBF part, there are three common approaches—(i) microscopy imaging (typically optical microscopy, OM), (ii) μ-computed tomography (μ-CT) and (iii) the Archimedes method. The OM approach is the simplest method for providing detailed porosity information, but it is

**Figure 1** A summary of various types of metal AM technologies based on the material joining mechanism, as reproduced with permission from [2] (Copyright 2020, Springer Nature).



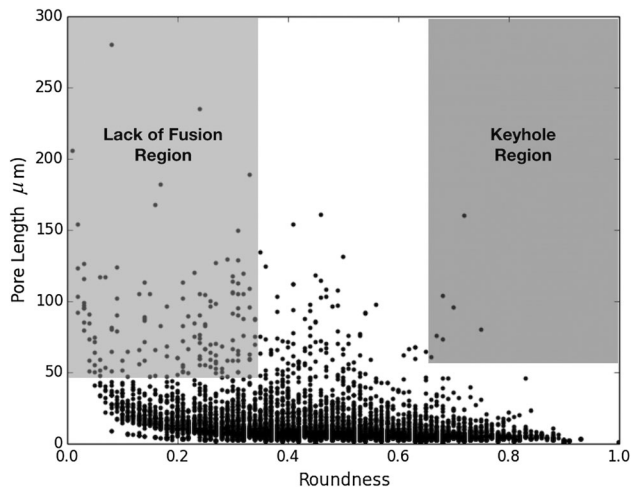
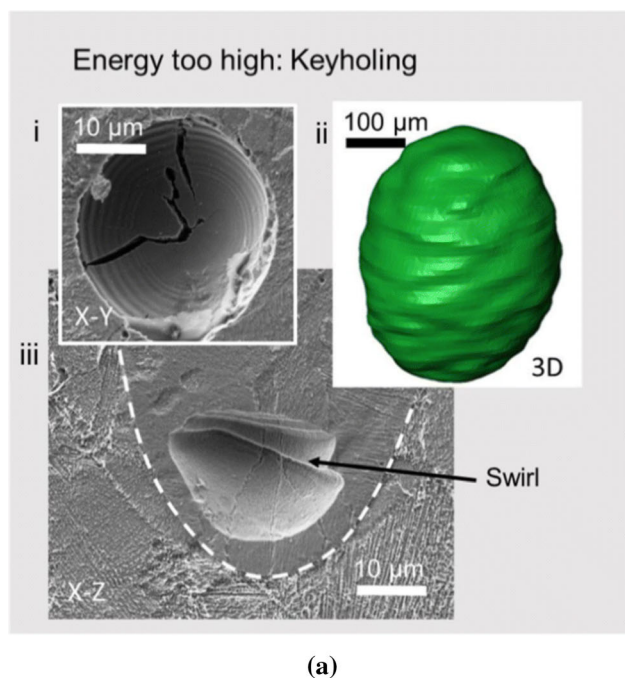
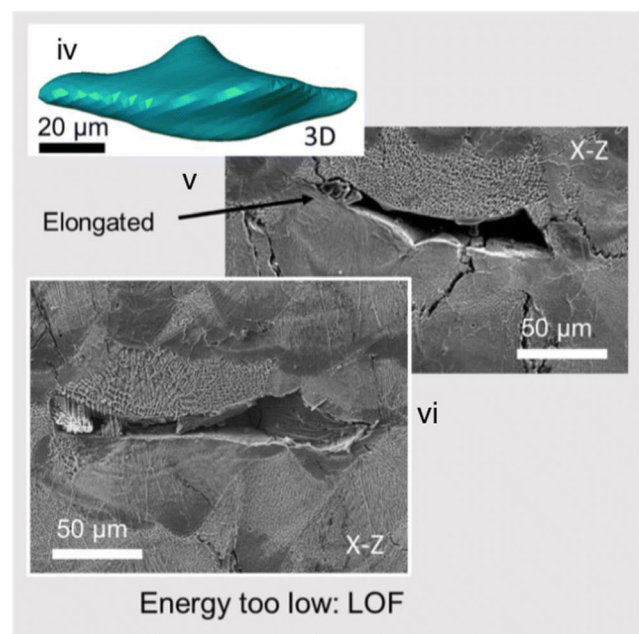


**Figure 3** Relationship between pore roundness and pore length from a sample set of 2D pore data where the authors investigated various computational methods to accurately identify different types of pores in Ti and Ni alloys from 2D optical micrographs. The regions where pores are typically classified as LoF or keyhole are also illustrated in the diagram. This figure was reproduced in grayscale from [10] which was published under the Creative Commons Attribution 4.0 International License (<http://creativecommons.org/licenses/by/4.0/>).

destructive as it involves the cutting and polishing of samples. Additionally, it is fundamentally a 2D technique that is also more prone to selection bias [11]. On the other hand,  $\mu$ -CT is a complex non-destructive 3D technique, with the main disadvantage being that its accuracy is often a compromise between porosity resolution, the volume to be analyzed and cost, which can lead to an underestimation of the porosity level [11], and noise reduction through filter algorithms often needs to be done at the expense of image clarity [12]. A recent study, however, has shown that for a given sample volume,  $\mu$ -CT is generally more cost-effective and more accurate than OM for porosity analysis [13]. Lastly, the Archimedes approach is also non-destructive, but its accuracy is more limited for near fully dense parts because the true theoretical density of an AM alloy is often not known and the measurement can be affected by surface quality [11, 12]. Furthermore, this approach does not provide any information on the nature, distribution and size of the pores [14]. Therefore, in acknowledging that there are slight differences in the accuracy of these methods, whenever a porosity level



(a)



(b)

**Figure 4** Typical morphology of (a) a keyhole pore and (b) an LoF pore found in LPBF Inconel 713C as obtained using  $\mu$ -CT and scanning electron microscopy (SEM). Reproduced from [10] which was published under the Creative Commons Attribution 4.0

International License (<http://creativecommons.org/licenses/by/4.0/>). The swirl identified in (a) was caused by turbulent flow during fabrication in [166].

(assumed to be the volume percentage of pores in the context of this review) is reported from a cited work, the measurement method will also be provided.

Even though porosity formation can be greatly minimized by choosing optimal LPBF parameters, it must be emphasized that there is no guarantee that using the same set of processing parameters would always result in the same type(s) and amount of pores since LPBF production is known to suffer from poor repeatability [15] and porosity distribution can also be affected by other factors such as part geometry [16, 17], feedstock powder particle size [18], powder bed temperature [19], heat treatment (which can cause gas pore to enlarge) [20–22], and gas flow behavior [23]. In fact, pores may not necessarily be uniformly distributed within a single part [24] and LPBF parameters optimized for part density often involve an undesirable trade-off with production speed [25]. Additionally, post-fabrication pore closure strategies often have limitations. For instance, hot isostatic pressing (HIP) is commonly used to close pores across an entire part, but this approach also alters the material's microstructure and may not necessarily close all pores due to trapped gases [26]. HIP is also more limited in closing irregular-shaped pores, and spherical pores that fail to close may actually end up being more elongated [27]. While surface treatment methods such as shot-peening can close surface and sub-surface pores (which tend to be more detrimental to mechanical properties as compared to pores within the bulk material) [28], this approach only works on accessible surfaces of a given component.

Considering that porosity is unavoidable in LPBF alloys and mitigation/reduction strategies often have limitations, understanding how pores affect various mechanical properties is particularly important for damage tolerant component design, service life expectations, risk management, and the pursuit of faster LPBF production speeds. To this end, this review provides a concise overview of how process-induced porosity affects the tensile behavior, impact toughness, fracture toughness, creep response, wear, and fatigue of LPBF alloys. While the number of alloys that can be fabricated by LPBF has grown in recent years, this review will focus on the most commonly investigated alloy from four different alloy classes—Ti-6Al-4 V, Inconel 718, AISI 316L, and AlSi10Mg. Thus, this review differs from other similar articles such as [29–31]. Additionally, there are

also other reviews that cover various aspects of these LPBF alloys such as [32–43] for Ti-6Al-4 V, [32, 33, 44–47] for Inconel 718, [32–37, 48, 49] for AISI 316L and [33, 50–56] for AlSi10Mg.

## Alloy overview

Ti-6Al-4 V, herein referred to as Ti64, has received significant attention for LPBF fabrication particularly in the aerospace industry as this alloy accounts for more than half of Ti usage, and AM substantially reduces machining costs and material wastage (Ti is expensive and also costly to machine) [39, 57]. The fast cooling rate of LPBF fabrication will often result in a strong but brittle  $\alpha'$  martensitic structure, as shown in Fig. 5a. Thus, a post-process heat treatment is often required to decompose this phase into the more desirable  $\alpha + \beta$  lamellar or bimodal microstructure, as shown in Fig. 5b–e and 6 [58–60].

Alloy GH4169, or Inconel 718 (herein referred to as IN718), is the most widely used superalloy due to a combination of good strength, good corrosion resistance, weldability and long term stability at moderately high temperatures ( $\sim 650$  °C) [61–63]. It is often strengthened through intermetallic precipitation—namely,  $\text{Ni}_3(\text{Al}, \text{Ti}, \text{Nb})$ ,  $\text{Ni}_3\text{Nb}$  (body-centered tetragonal), and  $\text{Ni}_3\text{Nb}$  (orthorhombic). These phases are referred to as  $\gamma'$ ,  $\gamma''$ , and  $\delta$ , respectively [63]. As the amount of solid solution Nb is an important consideration for the formation of the strengthening phases [64], an initial heat treatment step to dissolve any precipitated Laves or  $\delta$  phases is crucial to increase and possibly homogenize the amount of Nb in solution. The homogenization step (if performed) is done at  $\sim 1080$  °C, followed by solution treatment at  $\sim 980$  °C, and finally, two subsequent aging steps at 720 °C and 620 °C are usually performed to precipitate the strengthening phases. Figures 7 and 8 show the typical microstructures of LPBF IN718 in the as-built and solution-treated + double-aged conditions, respectively. Figure 8 also shows forged and cast IN718 for comparison.

AISI 316L is a comparatively simple alloy as it is not strengthened by the presence of hard phases or by the microstructural manipulation of multiple metallic phases. Conventionally, heat treatments are mainly done to homogenize alloying elements in solution, for hot working, for stress relieving, and/or to undo the effects of cold working [65]. Thus,



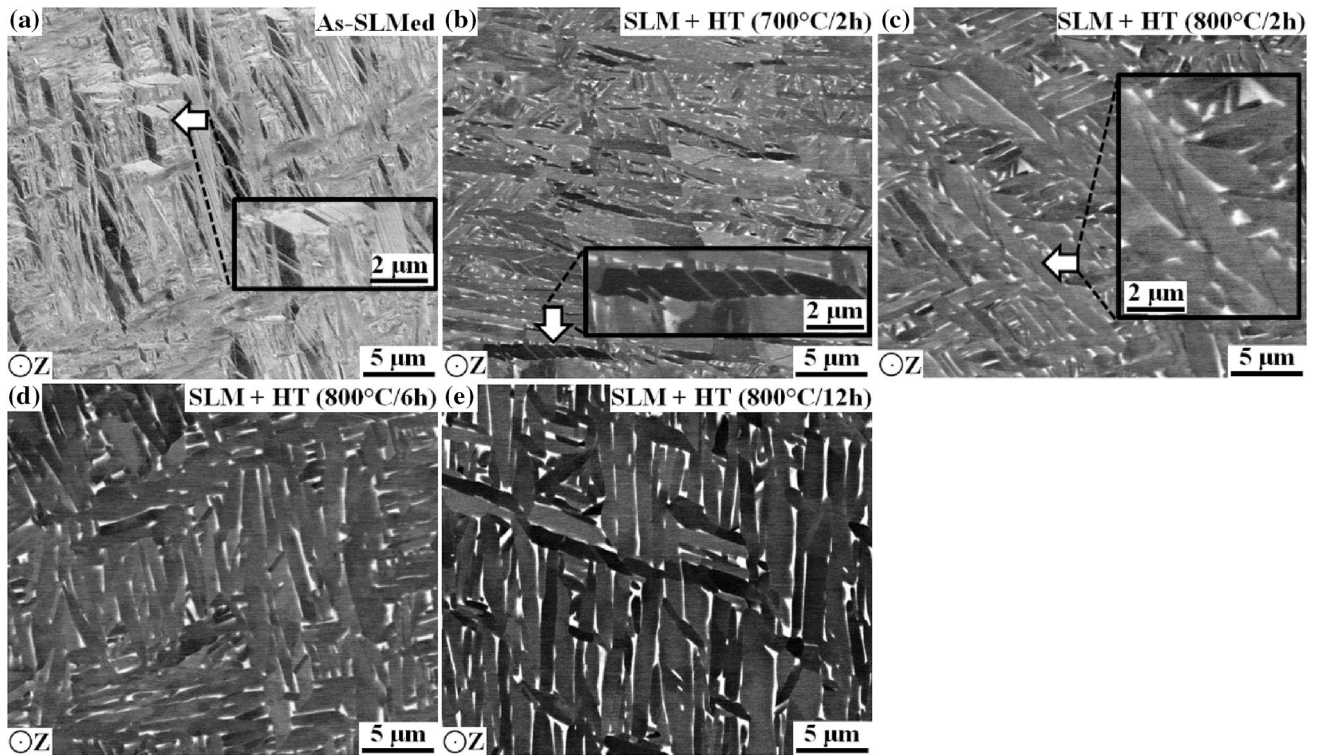


**Figure 5** SEM images taken on the horizontal plane of LPBF Ti64 samples showing (a) the as-built  $\alpha'$  martensitic structure, and (b–e) the effect of various decomposition heat-treatment parameters on the resulting  $\alpha + \beta$  microstructure. The authors found that a higher heat treatment temperature or a longer

treatment time resulted in coarser  $\alpha$  grains and an increase in  $\beta$  volume fraction and thus, decreased yield and tensile strengths in exchange for improved ductility. Reproduced with permission from [58] (Copyright 2018, Elsevier).

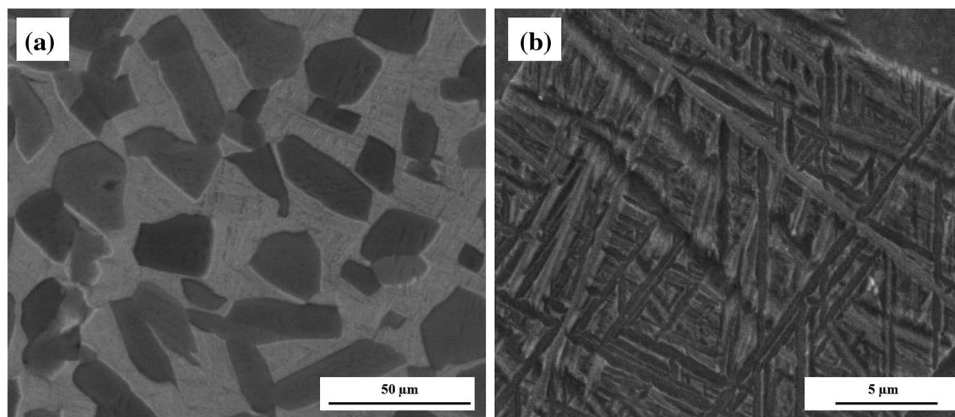


**Figure 6** SEM images showing the bimodal microstructure of LPBF Ti64 where (a) shows the globularized  $\alpha$  and (b) shows the Widmanstätten morphology of the grains between the globularized

$\alpha$ . This microstructure was obtained through thermal cycling between 875 °C and 975 °C for 24 h followed by air cooling. Adapted with permission from [60] (Copyright 2019, Elsevier).

whether a (typical) heat treatment is applied or not, LPBF 316L will generally be a single-phase austenitic alloy [66].

Al alloys are very challenging materials for LPBF production due to their high thermal conductivity,

reflectivity and propensity for oxidation [53, 67, 68]. Thus, cast Al alloys have received significant focus as their excellent castability and weldability allow for easier LPBF processing [69], with AlSi10Mg being one of the most common. In the as-built condition,

**Figure 7** Typical microstructure of as-built LPBF IN718 where (a) and (b) show the melt-pool boundaries from the side and top views, respectively, and (c) and (d) show the grains located at the layer—layer melt-pool boundaries and at the track—track boundaries, respectively. The yellow arrows show the dendrite growth directions and BD is the building direction. Reproduced with permission from [167] (Copyright 2017, Elsevier).

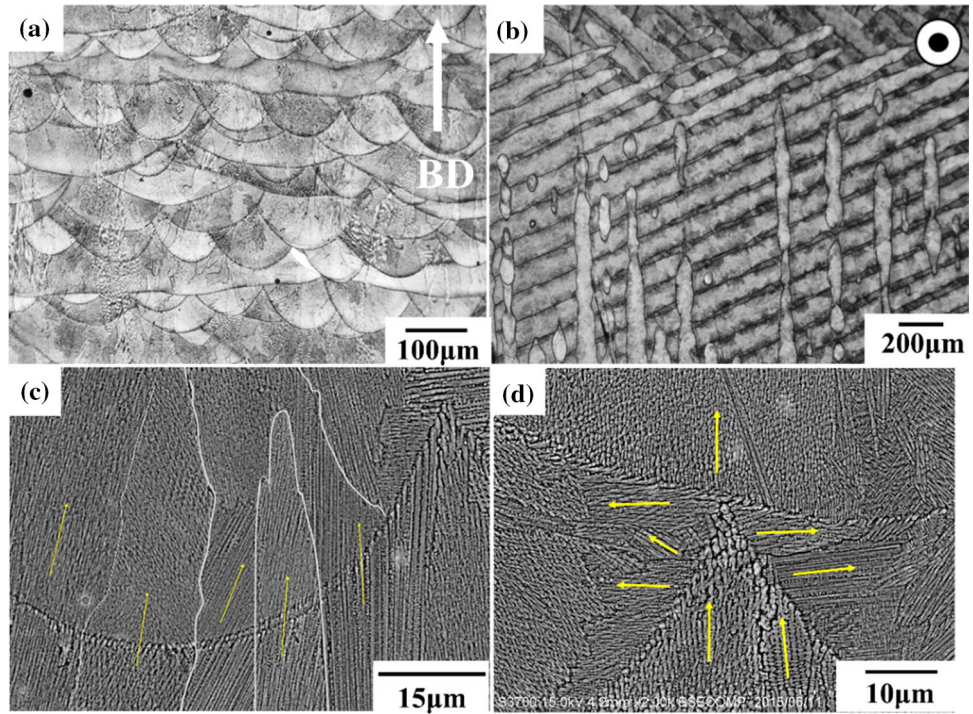
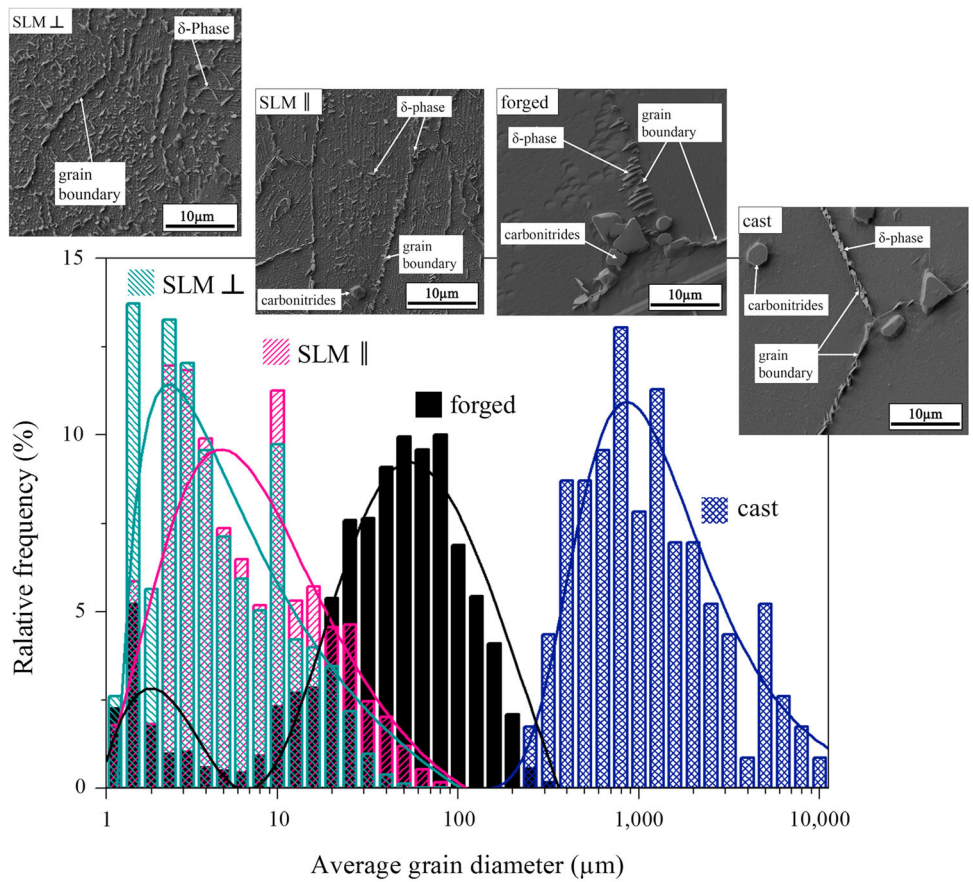


**Figure 8** Microstructure comparison of LPBF-processed, forged, and cast IN718. The  $\parallel$  and  $\perp$  symbols represent measurements and images taken on sample planes parallel and perpendicular to the LPBF building direction, respectively. The authors found that LPBF processing resulted in much finer microstructures as compared to conventional manufacturing methods. The LPBF IN718 was solution-treated and double-aged. Reproduced with permission from [168] (Copyright 2016, Elsevier).





AlSi10Mg has a hierarchical microstructure where large Al grains present a fine cellular–dendritic solidification structure with submicron-sized primary Al-cells and an intercellular Si network. The T6 is very commonly investigated for this alloy, which involves a solution treatment followed by an artificial ageing step [70–83]. This causes the re-organization of the Si phase which goes from being a nano-scale precipitate arranged in a cellular network to coarse Si particles that are several microns large, as shown in Fig. 9a and b. As T6 has often been found to be detrimental to strength, other authors have investigated other heat treatment strategies such as direct-ageing/T5 [84–86]. Figure 9c shows the effect of such a treatment where the as-built Si morphology is retained but with additional precipitation of nano-scale Si particles.

## Tensile properties

Figures 10, 11, 12, 13 provide an indication of the expected yield strength and ductility of LPBF Ti64, IN718, 316L, and AlSi10Mg, respectively. For LPBF Ti64, the yield strength generally ranges from 700 to 1300 MPa depending on the heat treatment involved. In general, the as-built  $\alpha'$  microstructure confers high strength but poorer elongation (typically above 1000 MPa and less than 10%, respectively) [38]. Heat treatment substantially increases elongation (up to  $\sim 22\%$ ) though this is often accompanied by a decrease in yield strength. Standard heat treatments for LPBF IN718 can substantially improve yield strength (from  $\sim 700$  MPa to above 1000 MPa) at the

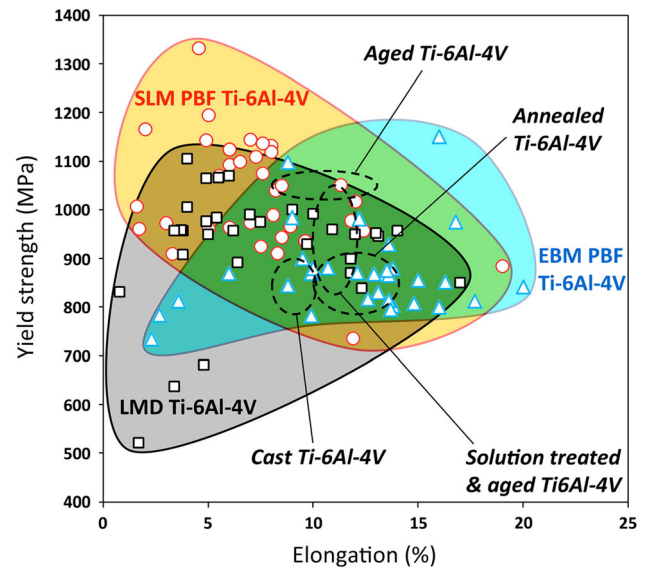


**Figure 10** Yield strength and elongation relationship of various AM-fabricated (where EBM stands for electron beam melting and LMD for laser metal deposition) and conventionally processed Ti64 as compiled from several sources by, and reproduced from, [37], which was published under the Creative Commons Attribution 4.0 International License (<http://creativecommons.org/licenses/by/4.0/>).

expense of elongation (generally 20% or less after heat treatment). LPBF 316L is by far the most ductile of the four alloys, with elongation values exceeding 50% (note that Fig. 12 displays uniform, not total, elongation). The as-built yield strength of this alloy is generally marginally lower than that of as-built IN718, but this alloy cannot be strengthened by heat treatment. Lastly, as-built LPBF AlSi10Mg has the lowest yield strength and elongation of the four

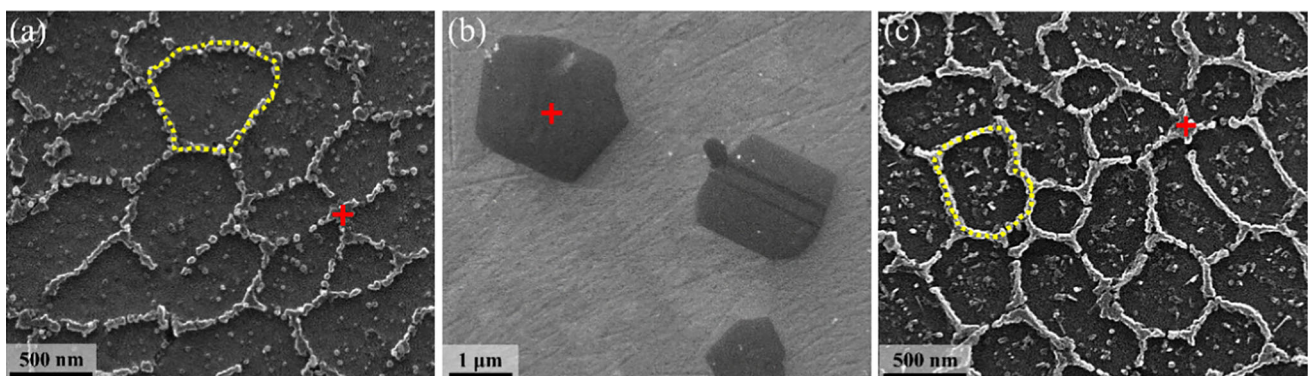


**Figure 9** Morphology of the Si phase in LPBF AlSi10Mg where (a) is the as-built condition, (b) is the T6 condition, and (c) is the direct-aged condition. Since the T6 heat treatment involves a solution treatment step, the as-built Si network is completely

dissolved into the matrix and subsequent ageing causes Si to precipitate as coarse discrete particles. With direct ageing, the as-built Si morphology is retained. Adapted with permission from [84] (Copyright 2021, Elsevier).

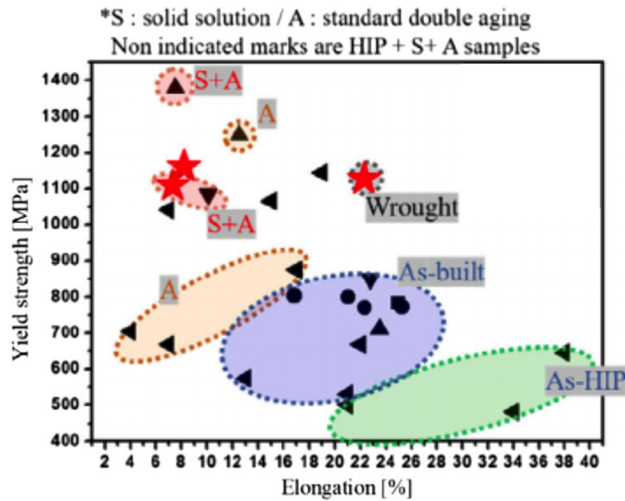


**Figure 11** Effect of various heat treatments on the yield strength and elongation of LPBF IN718, with the result of a wrought alloy also included for comparison as compiled from several sources by, and reproduced with permission from, [150] (Copyright 2020, John Wiley and Sons).

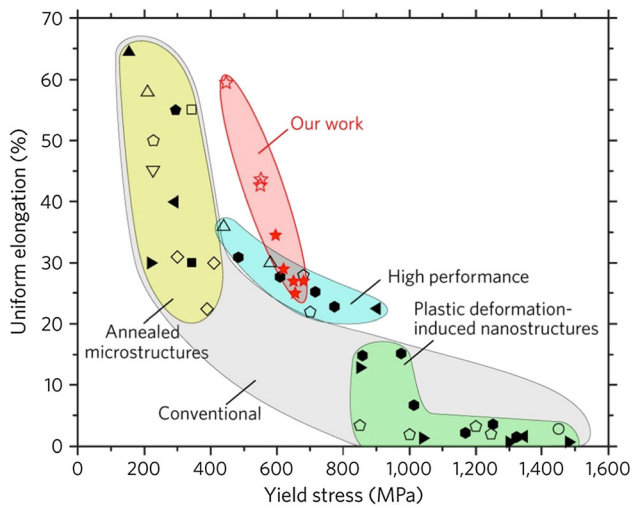


**Figure 12** Capability of LPBF 316L in breaking the strength/ductility trade-off that is often encountered in conventional processing of 316L, as compiled from several sources by, and reproduced from, [169], which was published under the Creative Commons Attribution 4.0 International License (<http://creativecommons.org/licenses/by/4.0/>).

alloys at ~ 300 MPa and ~ 5% ductility, respectively. As shown in Fig. 13, solution treatment substantially improves ductility at the expense of strength. As mentioned in the previous section, subsequent ageing (i.e. T6) may nor may not fully restore that strength.

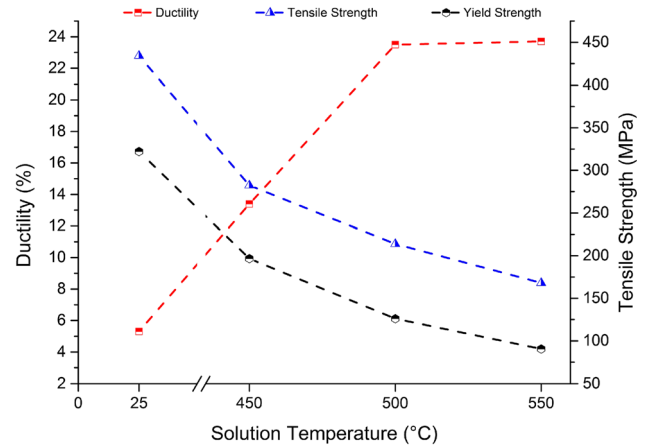


**Figure 13** Effect of solution treatment temperature on the yield strength, tensile strength, and ductility of LPBF AlSi10Mg. Reproduced from [56] which was published under the Creative Commons Attribution 4.0 International License (<http://creativecommons.org/licenses/by/4.0/>).

Table 1 summarizes the influence that porosity plays on the tensile properties of LPBF-processed Ti64, IN718, 316L, and AlSi10Mg, respectively, as reported in recent literature. As can be observed, elongation at fracture is generally reported to be far more sensitive to porosity level as compared to strength. The detrimental nature of pores is typically explained through (i) a reduction in the true load-bearing area, (ii) the facilitation of pore coalescence leading to premature failure, (iii) increased stress-concentration points, (iv) acting as initiation sites for micro-cracking, and (iv) providing a preferential path for crack propagation [75, 83, 87–95]. These issues are frequently reported to be worse for vertically built samples due to the orientation of LoF pores and/or interlayer pores (i.e., pores that are distributed along layer boundaries) [75, 90, 96–102].

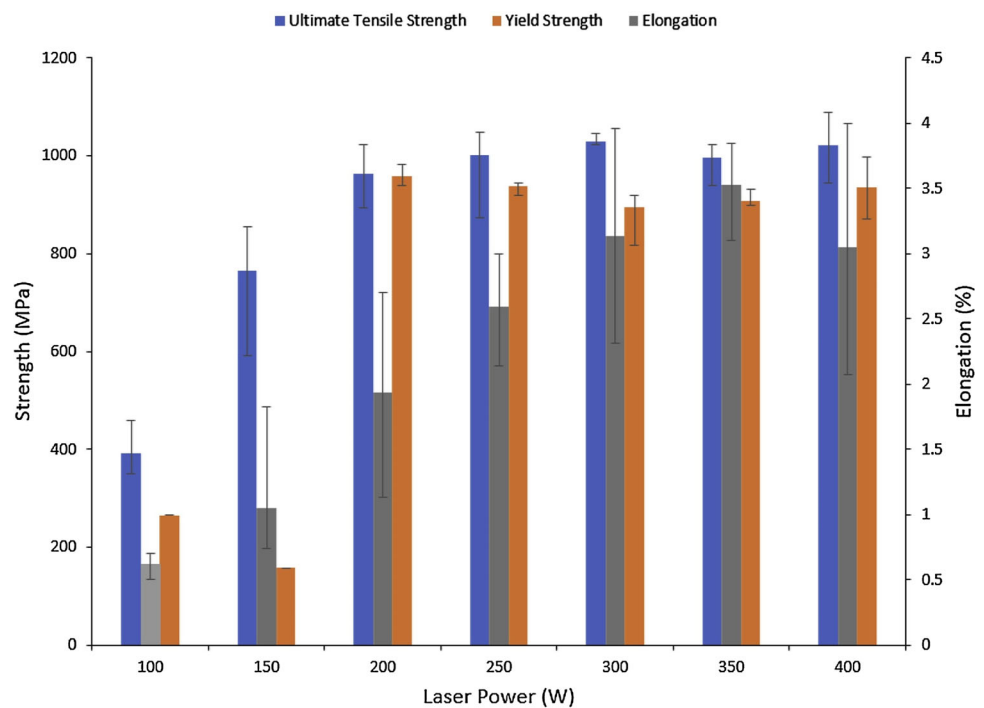
As can also be observed in the table, a number of studies have confirmed for these LPBF alloys that as porosity is decreased, tensile behavior generally improves, but at low porosity levels, there may be no correlation to porosity. This is because, as porosity approaches zero, microstructure begins to overtake porosity to become the dominant factor that determines tensile behavior [25, 94]. For instance, Kan et al. noted that this transition occurred when the porosity in LPBF Ti64 is reduced below 1% (OM method) [25]. Kaschel, Celikin, and Dowling also highlight this for LPBF Ti64 as shown in Fig. 14, where porosity reduced from ~ 0.27% to ~ 0.02% (CT method) as laser power increased to 250 W (with



**Table 1** Observations of how porosity affects the tensile behavior of LPBF alloys either as reported or inferred from the recent literature

Influence of porosity on tensile behavior	Material	References
Poor elastic modulus, yield strength, tensile strength and/or elongation at fracture attributed to porosity	IN718 AlSi10Mg	[125] [8, 18, 171–174]
At high porosity levels, decreasing porosity improves elastic modulus, yield strength, tensile strength, and/or elongation at fracture. At low porosity levels, these properties may show no correlation with the amount of porosity present	Ti64 IN718 316L AlSi10Mg	[7, 25, 103, 175] [9, 102, 116] [176, 177] [92, 178–180]
Elongation at fracture is particularly sensitive to the amount of porosity present as compared to strength	Ti64 IN718 316L AlSi10Mg	[7, 25, 88, 94, 105, 181] [104] [16, 176, 182] [92, 183]
LoF pores are more detrimental to the modulus, strengths and/or ductility as compared to other pore types	Ti64 IN718 AlSi10Mg	[7, 25, 87] [104, 184–186] [187]
LoF or interlayer pores are far more detrimental to elastic modulus, strengths, and/or elongation at fracture for vertically built samples as compared to other orientations	Ti64 IN718 316L AlSi10Mg	[90, 96–99] [9, 102] [14, 17, 100, 101, 106, 107, 188, 189] [75, 76, 183]
Smaller sample sizes lead to increasing pore fraction at the cross-section, resulting in poorer strength and ductility	Ti64	[190]

**Figure 14** Tensile results of a study that investigated the effects of laser energy input on the mechanical properties and microstructure of LPBF Ti64 where the energy input was varied by adjusting laser power while keeping all other LPBF parameters kept constant. The 100 W, 250 W and 400 W samples have approximately 0.27, 0.02 and 0.05% porosity (CT method), respectively. Reproduced with permission from [103] (Copyright 2020, Elsevier).



other LPBF parameters kept constant), and the poor performance of the 100 and 150 W samples was attributed high porosity levels [103]. However, at low porosity levels, their results showed that the amount of porosity did not influence tensile properties, as

shown by the results of the 250 W and 400 W samples in the figure where the latter had a higher porosity level than the former ( $\sim 0.05\%$  vs  $\sim 0.02\%$ , respectively). Yi et al. investigated various line laser energy densities for LPBF IN718, as shown in Fig. 15,

and attributed improved strength and elongation performance to the reduction in size and amount of pores present, with the 0.2 J/mm condition being optimal [9].

However, the type, rather than amount, of pores may matter more, as LoF pores are frequently reported to be far more detrimental to tensile properties as compared to gas/keyhole pores. Montalbano et al. investigated LPBF Ti64 samples containing up to ~ 8% porosity (CT method) where these samples either contained predominately LoF pores or keyhole pores, with the tensile results shown in Fig. 16 [7]. The authors found that LoF samples with ~ 1% porosity had similar modulus to keyhole samples of comparable porosity levels, but LoF samples with more than 4% porosity performed worse. In terms of strength, LoF samples performed worse than KH samples across all porosity levels. Furthermore, when the authors corrected these results to account for the reduction in load bearing caused by porosity fraction, they found that the modulus and strength of keyhole samples were reduced as expected, but the reduction was worse than expected for LoF samples. The authors attributed this to the increase in stress concentrations caused by the irregular shapes of LoF pores. It should be noted that these samples were printed horizontally, or specifically, along the recoating direction, which minimizes the detrimental influence of LoF pores. The study by Kantzos et al. also highlights this for LPBF IN718 as shown in Fig. 17 [104]. Despite Parameter Set 5 containing the highest amount and the largest of (keyhole) pores,

Parameter Set 2 had the lowest average elongation because it contained LoF pores, though elongation of Parameter Set 5 displayed considerable scatter.

Both Figs. 16 and 17 also show the sensitivity of elongation to porosity as compared to strength. In the former, elongation was greatly reduced as porosity increased even for samples that only contained keyhole pores. In the latter, the scatter in strength is far less than the scatter in elongation. Similarly, Mathe et al. show that even with a very small increase in porosity, the elongation of LPBF Ti64 was substantially reduced, as shown in Fig. 18 [105]. The authors noted that the Archimedes measurements were taken on machined samples while the CT measurements were taken with as-built surfaces, which could account for the discrepancy in the data in addition to the limitations of each measurement method. Another example, for LPBF IN718 with porosity levels up to 1.2% (Archimedes method), as shown by the 650 °C tensile tests conducted by Hilaire, Andrieu, and Wu in Fig. 19 [102], only the strain to failure decreased with increasing porosity level (with vertical samples being more sensitive due to LoF pore orientation) while yield and tensile strengths had no relation, at least with the samples containing 1% or less porosity. Likewise, with the results shown in Fig. 20, Laursen et al. found that porosity (both in terms of fracture surface and bulk material porosities) had a much stronger correlation with elongation than with stiffness or strength for LPBF AlSi10Mg for porosity levels of up to 5% (Archimedes method) [92].

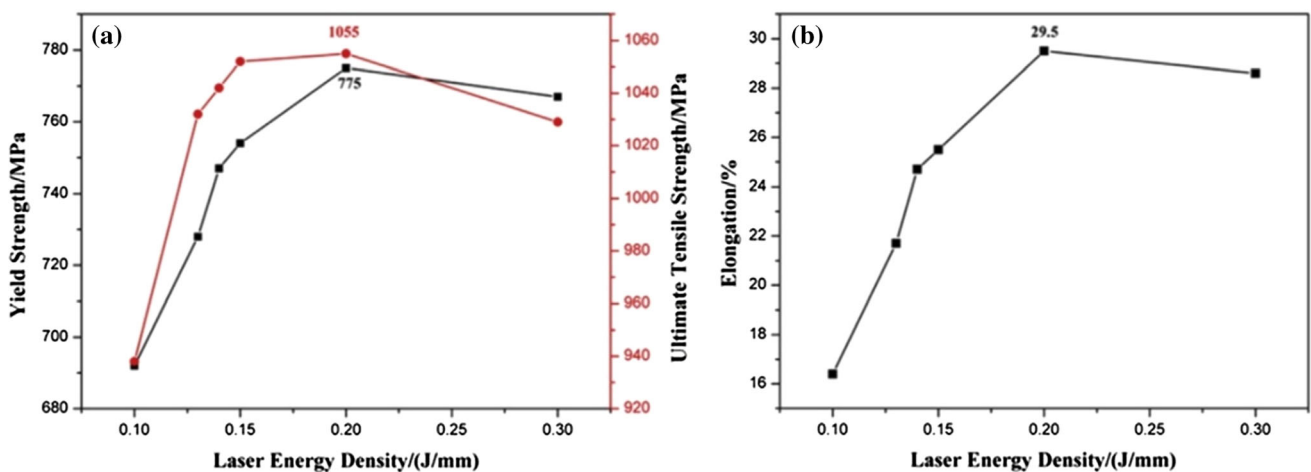


**Figure 15** Tensile results of a study that investigated the effects of laser energy input, as defined using linear laser energy density calculations, on the mechanical properties and microstructure of

as-built LPBF IN718 bars: (a) ultimate tensile strength/MPa and yield strength/MPa; and (b) elongation. Reproduced with permission from [9] (Copyright 2019, Elsevier).

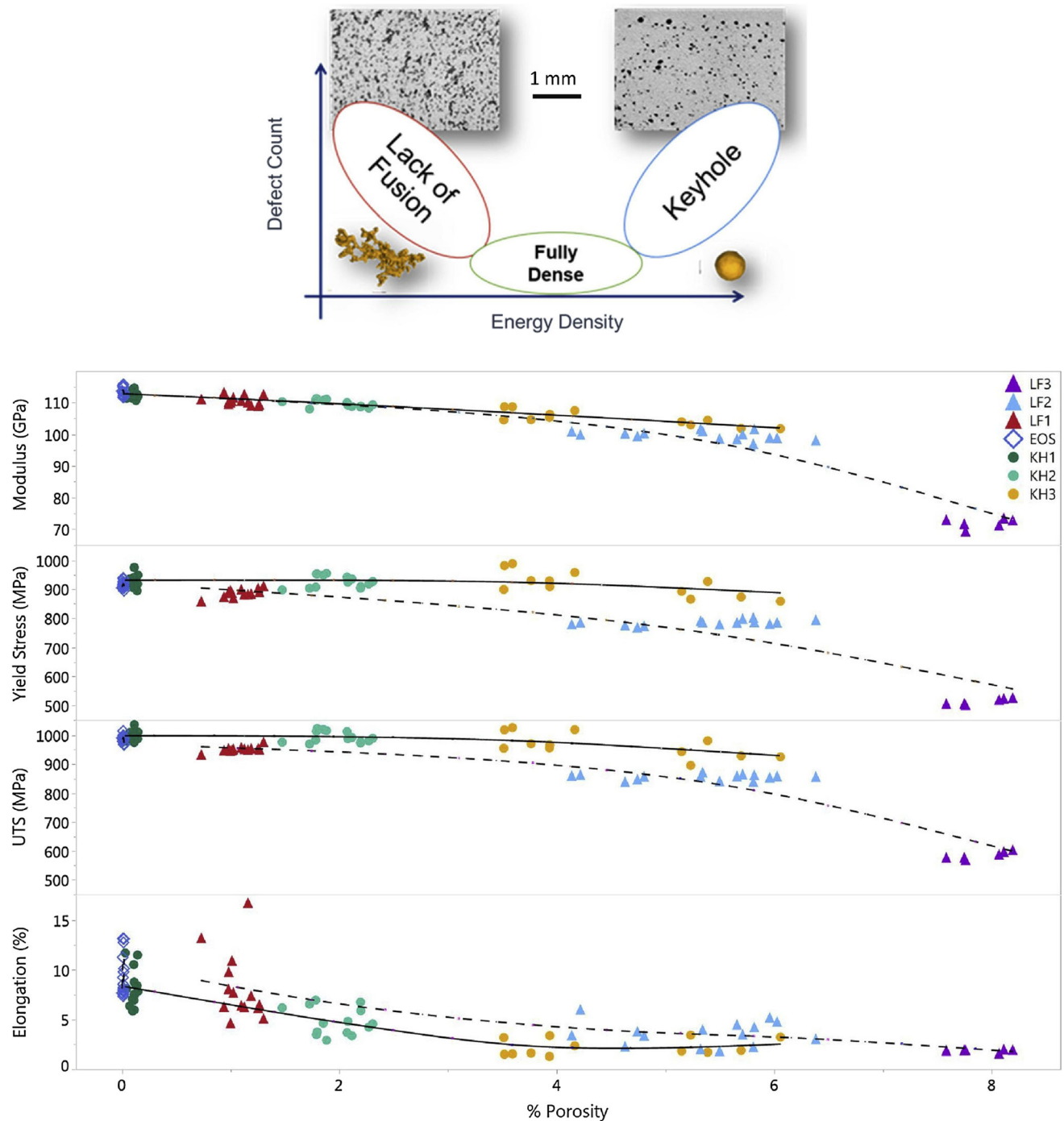


**Figure 16** Results of a study that investigated the effects of increasing keyhole (KH) or LoF (LF) porosity on microstructure and mechanical properties of LPBF Ti64. The relationship between laser energy density and the type of pores formed is shown on the

top and their subsequent influence on tensile properties is shown on the bottom. Adapted with permission from [7] (Copyright 2021, Elsevier).

LoF pores being particularly detrimental to vertically built samples were explained by Ronneberg, Davies and Hooper, in their study on LPBF 316L, to be due to how the major axis of LoF pores is oriented

relative to the tensile axis as illustrated in Fig. 21 [106]. As observed in Fig. 21b, not only is the actual load-bearing cross-sectional area much smaller, the pore is “stretched apart” perpendicularly to its major

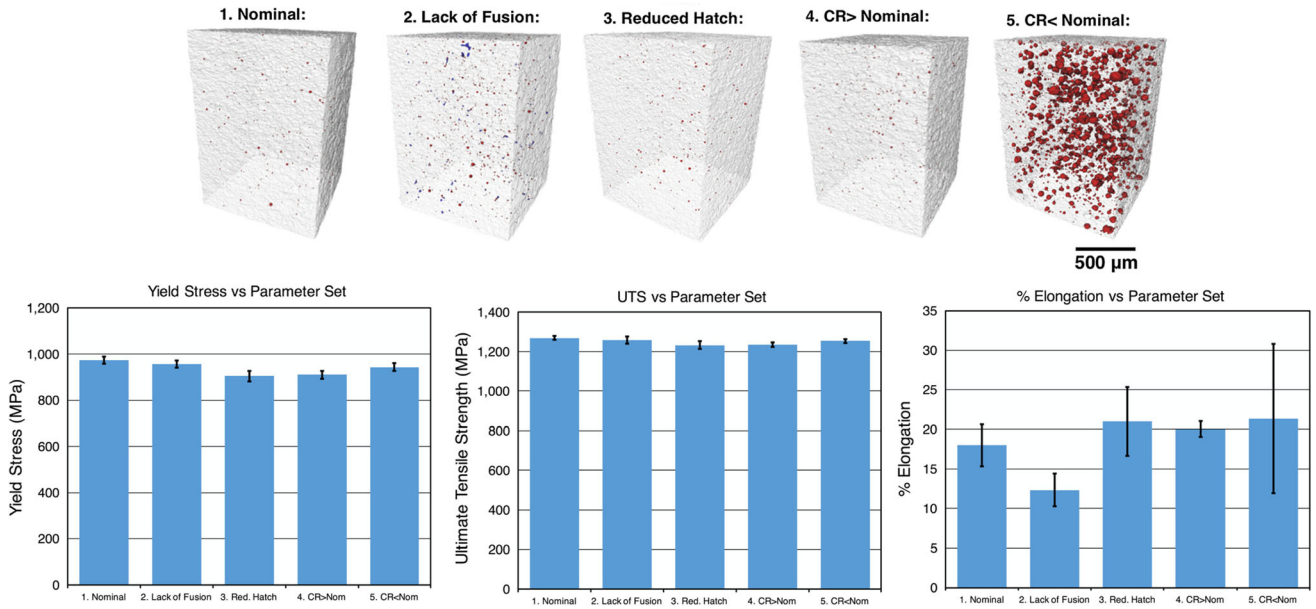


**Figure 17** Results of a study that investigated the effects of LPBF parameters on the microstructure, porosity and mechanical properties of IN718. All samples were heat-treated (986 °C for 1 h followed by 718 °C for 9 h). The porosity distribution results of the five different processing parameters used, as obtained

through synchrotron-based  $\mu$ -CT analysis, is shown at the top, and their resulting tensile properties are shown at the bottom, as adapted with permission from [104] (Copyright 2019, Springer Nature).

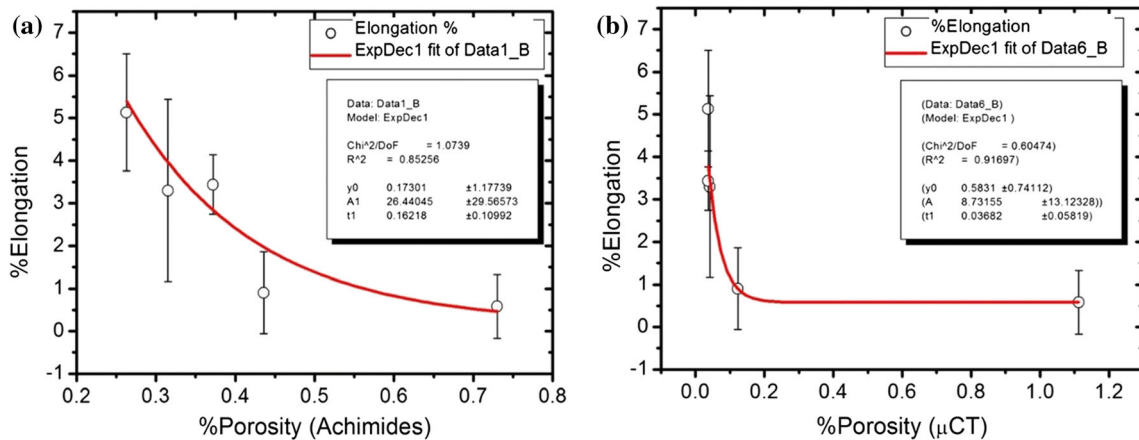


**Figure 18** Ductility results of a study investigating the effects porosity on the ductility of LPBF Ti64 where porosity was measured using two different methods—(a) Archimedes and (b)  $\mu$ -CT. The authors noted the discrepancies between the two porosity

measurement methods which could have also been affected by the fact that the Archimedes samples had machined surfaces, but the  $\mu$ -CT samples were measured as-built. Reproduced with permission from [105] (Copyright 2021, Springer Nature).

axis in tension and can lead to crack initiation. This is less of an issue for horizontal samples, since the tensile load will tend to cause the pore to close, as illustrated in Fig. 21c. This is highlighted in greater detail in Fig. 22 by Choo et al. where the evolution of pores during tensile testing of LPBF 316L was investigated [107]. As can be observed, for vertical samples, LoF pores easily grow and cause crack

initiation. The cracks quickly link up neighboring pores, and they quickly coalesce and fracture prematurely with minimal necking. However, for horizontal samples, the LoF pores rarely interact with neighboring pores and cracks do not propagate, allowing the material to neck considerably more. This inability to neck might also be the reason why pores tend to affect elongation more than strength, and



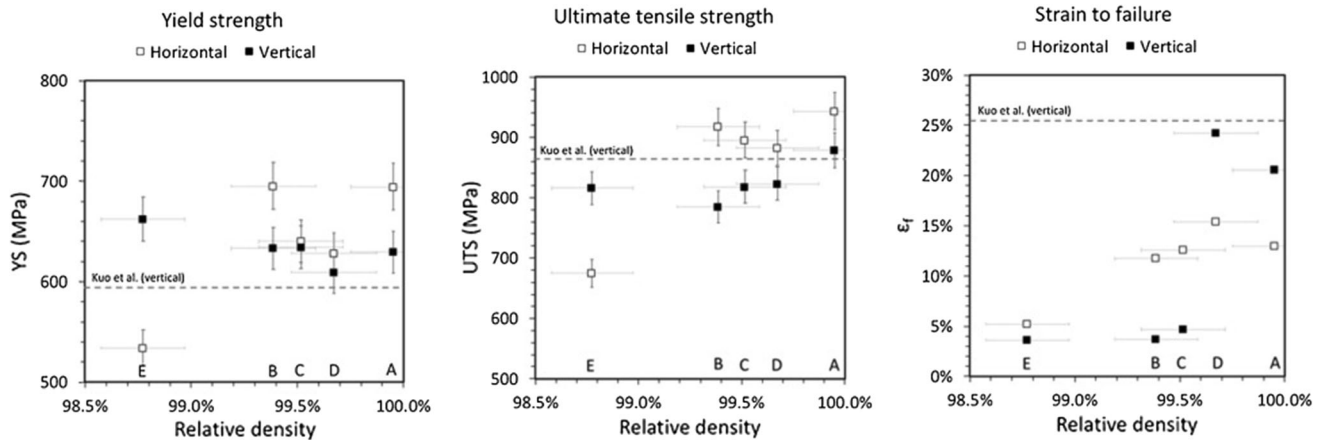


**Figure 19** High temperature tensile results (650 °C), as a function of the corresponding sample's relative density, of a study that investigated the effects of LPBF parameters and building direction

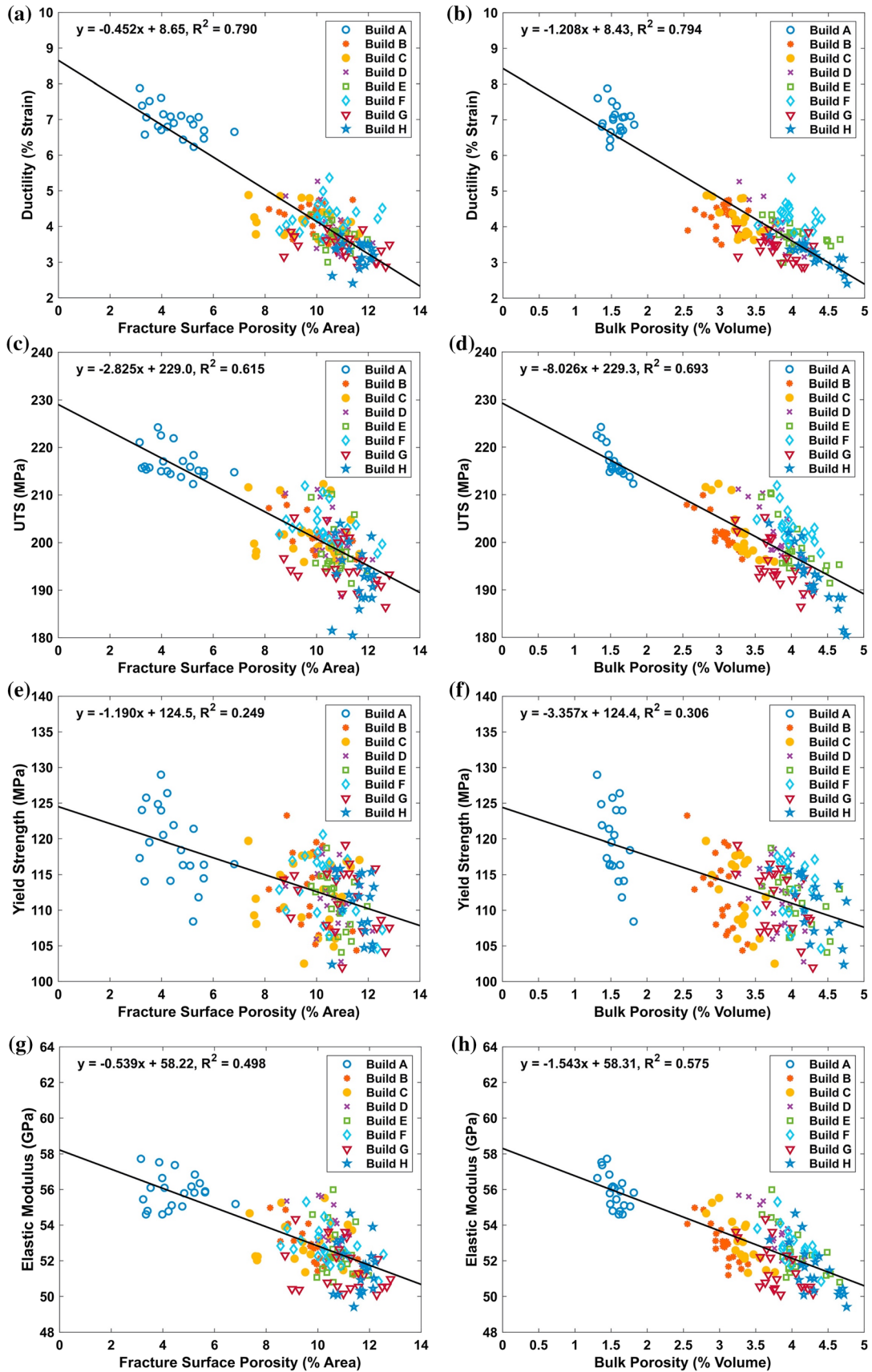
strength is generally only affected if reduction in the true load-bearing area exceeds that which can be compensated for by microstructure.

The aforementioned observation where tensile behavior transitions from being microstructure controlled to a porosity controlled when the porosity level exceeds a certain threshold highlights the fact that tensile properties are generally not significantly influenced by specific microstructure—porosity interactions, and therefore, the detrimental influence of porosity can be deduced purely from a structural perspective. For instance, as porosity is increased and the true load-bearing area is decreased as a result, then a corresponding decrease in strength should follow assuming that the microstructure is relatively unchanged. This was highlighted in the work by Kan et al. for LPBF Ti64 containing up to 14% porosity (OM method) where the decrease in elastic modulus, yield strength, and tensile strength can be more closely correlated with the porosity fraction without a consideration to microstructure effects using the linear rule of mixtures as long as the pores are spherical [25]. The authors noted that for samples containing predominately LoF pores, the rule of mixtures approach will need to be corrected for pore shape irregularities. This result is consistent with those of Montalbano et al., which, as mentioned earlier, found that the reduction in modulus and strength of LPBF Ti64 samples containing keyhole pores is directly correlated with the loss in the load-bearing area that corresponds to a given porosity level [7]. However, for samples containing LoF pores, these properties

on the mechanical properties of LPBF IN718. The relative densities were measured using the Archimedes method. Adapted with permission from [102] (Copyright 2019, Elsevier).

were found to be lower than expected even after taking the reduced load bearing area into account. It should also be emphasized that both studies investigated horizontally built samples which meant that the detrimental effect of LoF pore orientation could not be fully mitigated even when the tensile axis is aligned parallel with the major axis of the pores.

As pore growth and coalescence typically occur during the necking portion of a tensile test (i.e., after the ultimate tensile strength is reached), yield and tensile strengths can be said to be fundamentally affected by the initial porosity levels, while total elongation will be affected by the way pores grow, coalesce, and initiate and propagate cracks. Since pore fraction increases dramatically once necking occurs [94], elongation at fracture should behave far worse than what the rule of mixtures, where calculations are based on initial porosity levels, would suggest, as was reported by Kan et al. [25]. For example, Fig. 20 shows that for LPBF AlSi10Mg, fracture surface porosity can be  $\sim 3 \times$  higher than the initial bulk porosity level. Since the ease of pore growth and coalescence, and porosity-assisted crack initiation and propagation involve some interaction with the matrix, the elongation at fracture of a more ductile or tougher microstructure could potentially be less sensitive to the presence of porosity. This was confirmed by Smith et al., where the authors showed that the ductility of LPBF 316L was far less affected by process-induced porosity (as well as artificially built geometric defects) as compared to as-built and heat-treated LPBF AlSi10Mg [108]. Based on Figs. 10,



◀ **Figure 20** Effect of fracture surface porosity (a, c, e, g) and bulk porosity (b, d, f, h) on tensile properties of LPBF AlSi10Mg as obtained from a study that aimed to model the effects of porosity on tensile properties for LPBF-processed and cast AlSi10Mg alloys. Fracture surface porosity was measured using SEM imaging after the tensile tests while bulk porosity was measured using the Archimedes method, also after the tensile tests. Reproduced with permission from [92] (Copyright 2020, Elsevier).

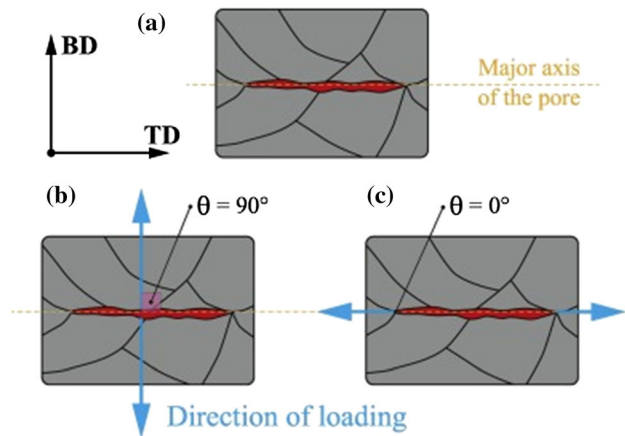


**Figure 21** A schematic illustration of the (a) relationship between LoF pore orientation and the building direction, and the direction of the tensile axis with respect to the pore orientation in (b) vertically built samples and (c) horizontally built samples. Reproduced from [106], which was published under the Creative Commons Attribution 4.0 International License (<http://creativecommons.org/licenses/by/4.0/>) and where the objective of the study was to determine the effects of microstructure and porosity on the mechanical properties of LPBF 316L.

11, 12, 13, LPBF AlSi10Mg and 316L should be the least and most tolerant to porosity (i.e., as porosity is increased, the corresponding relative decrease in elongation should be lower for the latter), respectively. In the as-built condition, LPBF Ti64 is expected to be more sensitive to porosity than LPBF IN718 while the reverse may be true if these alloys are heat-treated.

As mentioned earlier, HIP is often proposed as a way to close pores after LPBF production. The main issue with HIP is that pore closure is only effective when a high temperature is used, and this approach will remove the as-built microstructure of the alloy which is often known to confer high strength. For Ti64, a post-process heat treatment will decompose the as-built  $\alpha'$  microstructure into a dual-phase lamellar  $\alpha + \beta$  microstructure (if performed below

the  $\beta$  transus) which typically trades strength for improved ductility, a process that is further accelerated at higher temperatures. Thus, if a lamellar microstructure is desired, the decomposition treatment is typically done between 700 and 800 °C [58], and strength substantially falls due to significant coarsening of the microstructure if the heat treatment temperature approaches 900 °C [109]. Since HIP is often done above 900 °C for this alloy, the compromise to strength can be a major concern [110, 111]. With regards to 316L, the LPBF process results in a high dislocation density, fine grain size and the segregation of solutes into a cellular structure, all of which contribute to high strength [112]. As high-temperature heat treatments would annihilate dislocations and dissolve its cellular structure, a substantial reduction in strength usually follows [113] and this presents a problem with HIP since it is often performed above 1100 °C [100, 114]. Likewise, the nano-crystalline cellular structure of as-built LPBF AlSi10Mg will go into solution during HIP, and subsequent ageing, which results in the precipitation of coarse Si particles, will typically only restore a portion of its initial strength [75].

Unlike the other three alloys where the drawback of HIP can be quite substantial, LPBF IN718 stands to benefit the most from HIP, at least from a microstructural perspective. As was discussed in the preceding section, the as-built microstructure of LPBF IN718 is generally undesirable and the precipitation of the main strengthening phase(s) of this alloy requires homogenization and/or solution treatment to be conducted before the ageing treatments. Indeed, HIP is typically performed just slightly above the temperature normally used for homogenization treatments ( $\sim 1080$  °C). Ideally, HIP followed by rapid cooling is preferred to resemble the homogenized microstructure, which then allows ageing to be performed directly after HIP [115]. Thus, in addition to pore closure, HIP followed by subsequent ageing treatments of LPBF IN718 is often reported to result in better yield and tensile strengths, though at the expense of ductility, as compared to the as-built condition [115, 116]. As for the other three alloys, the main consideration whether to perform HIP, at least purely from a tensile perspective, is perhaps to reduce the scatter in (and potentially improve) ductility results that can be caused by even small amounts of porosity. This may be less of an issue for LPBF 316L because it is a much more ductile



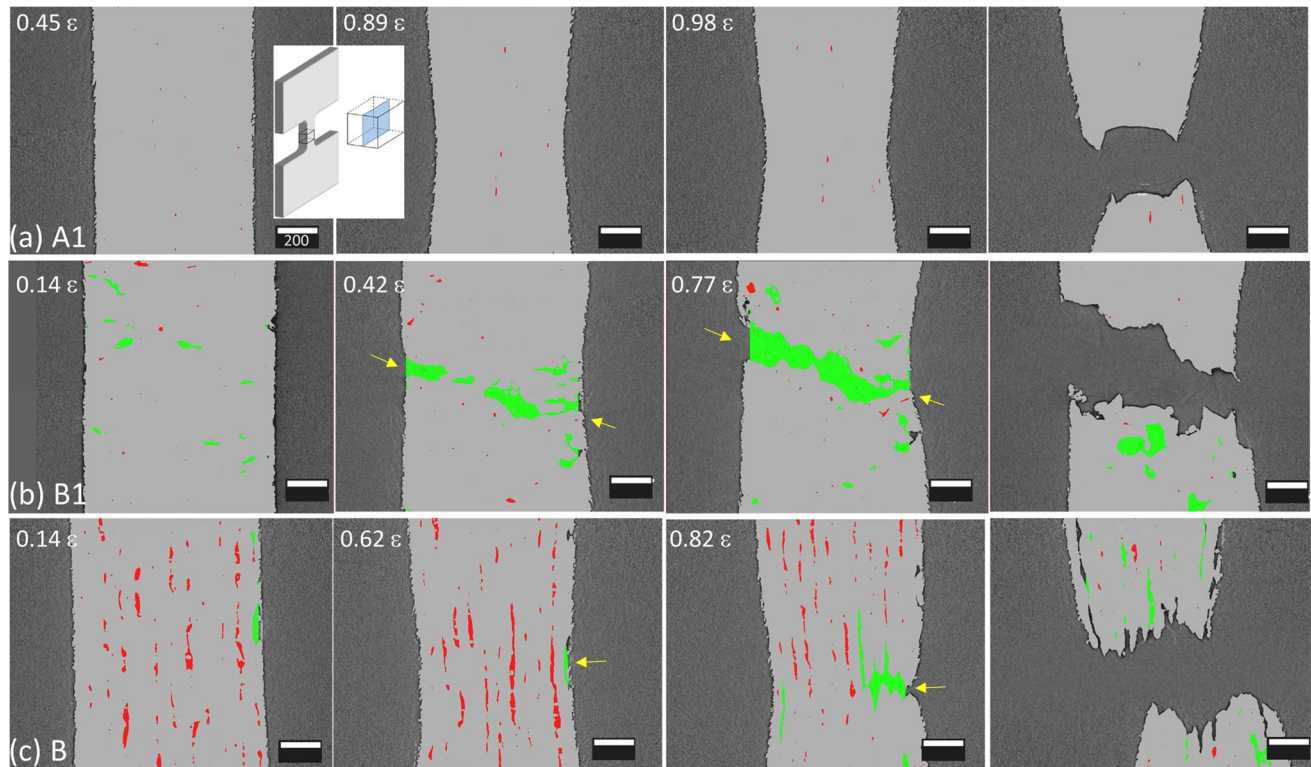


**Figure 22** 2D images, obtained using in-situ Synchrotron X-ray Computed  $\mu$ -Tomography, showing the evolution of the longitudinal cross-section during tensile loading to failure where (a) shows a near-fully dense sample, (b) shows LoF pores perpendicular to the loading direction, and (c) shows LoF pores

parallel to the loading direction. Open pores are illustrated in green while closed pores are in red. Reproduced with permission from [107] where the authors investigated the deformation and fracture behavior of LPBF 316L (Copyright 2021, Elsevier).

material, though pore closure could be beneficial for corrosion resistance. If heat treatments are necessary for LPBF AlSi10Mg, then HIP might have the added benefit of restricting pore growth during heat treatment, a phenomenon commonly reported for this alloy [20–22].

## Fatigue life

Table 2 summarizes the key findings of how porosity can influence fatigue life in LPBF-processed Ti64, IN718, 316L and AlSi10Mg alloys as reported in or inferred from recent literature. While fatigue behavior can be affected by a multitude of factors such as microstructure, composition, heat treatment, test frequency, surface finish and compressive residual stresses, it should be noted that the purpose of Table 2 is just to summarize key observations of how porosity affects fatigue behavior rather than to summarize the key findings of each reviewed study, and

therefore, information such as heat treatment or surface finish is only listed if it is relevant to the influence of porosity. Jian et al. conducted fatigue testing of LPBF AlSi10Mg at different stress ratios and found that the material behaved much better under compression-tension fatigue ( $R = -1$ ) as opposed to pure tension fatigue ( $R = 0$  or  $0.5$ ). The authors noted that this was likely because in the former case, pore closure occurs during the compression phase of each fatigue cycle. For this reason, the stress ratios are also included in Table 2.

Assuming that crack initiation is not caused by surface roughness, the table highlights several key observations regarding how porosity influences the fatigue life of these alloys. Most notably, fatigue life improvements due to machining are often limited because sub-surface pores will simply be exposed as the material between them and the surface is removed [117–121]. Additionally, microstructure/strength is often the dominant factor that determines high-stress (low-cycle) fatigue performance, while



**Table 2** Observations of how porosity affects the fatigue behavior of LPBF alloys either as reported or inferred from recent literature. The fatigue stress ratios ( $R$ ) are also listed

Ref.	Material	Stress Ratio	Effect of porosity on fatigue life of LPBF Ti64
[191]	Ti64	$R = 0.1$	Without surface machining, internal pore closure using HIP alone does not improve fatigue life With HIP and machining, LPBF Ti64 can outperform an annealed one in high-cycle fatigue despite a coarser microstructure
[111]	Ti64	$R = -1$	Effect of pore closure can be compared between heat-treated and HIPed samples where both were conducted at 920 °C/2 h but the latter with a pressure of 100 MPa which reduced porosity from $\sim 0.01\%$ to $\sim 0.001\%$ and the average pore diameter from $\sim 30 \mu\text{m}$ to $\sim 15 \mu\text{m}$ The heat treatment improved fatigue life from a fatigue limit of $< 300 \text{ MPa}$ to $350\text{--}400 \text{ MPa}$ , but HIP improved it to $450\text{--}500 \text{ MPa}$
[117]	Ti64	$R = 0.1$	Surface machining is crucial for improving fatigue life, though sub-surface pores exposed from the machining process can lead to fatigue failure
[118]	Ti64	$R = -1$	Polishing alone does not significantly improve fatigue life as exposed sub-surface pores still lead to fatigue failure HIP improved fatigue life but still resulted in considerable scatter while subsequent polishing reduced scatter and achieved 70% fatigue strength of a wrought equivalent was achieved
[192]	Ti64	$R = -1$	Pore morphology is less critical than pore location relative to the surface
[193–196]	Ti64	$R = 0, -1, 0.1$	LoF pores, especially if exposed, are more detrimental than other pores as they often act as crack nucleation sites that lead to fatigue failure
[129, 197]	Ti64	$R = 0.1, 0.2$	LoF pores result in poorer fatigue life for vertically built samples as compared to horizontal ones
[122–124]	Ti64	$R = -1$	Below very high-cycle fatigue regime, surface properties and surface/sub-surface pores dictate fatigue life At very high-cycle fatigue, bulk porosity becomes more relevant
[145]	Ti64	$R = -1$	Porosity closure through HIP can improve fatigue life
[198]	Ti64	$R = -1$	Small irregular-shaped pores can be as detrimental as large ones if the resulting stress-concentration is similar
[199]	Ti64	$R = -1$	Microstructure is more important than pore closure in low-cycle fatigue
[132]	IN718	$R = 0.1$	Sub-surface pores are detrimental to fatigue life
[200]	IN718	$R = 0.1$	If LoF pores are aligned parallel to the loading axis, fatigue life can be predicted based on the size of the spherical pores
[201]	IN718		For an average as-built IN 718 grain size of $48 \mu\text{m}$ , the critical pore size is $20 \mu\text{m}$ or $10 \mu\text{m}$ if the distance between pores is closer than $15 \mu\text{m}$ due to pore-to-pore interactions
[139, 140]	IN718	$R = 0.1, -1$	Using an appropriate heat treatment, the detrimental nature of pores can be suppressed to an extent through the formation of fine acicular $\delta$
[202]	IN718	$R = 0.1$	Surface LoF pores are extremely detrimental to fatigue life at $650 \text{ }^\circ\text{C}$ Pore shape is more important when the pore depth is less than $200 \mu\text{m}$ Machining and polishing can improve fatigue strength by $\sim 50\%$
[125]	IN718	$R = -1$	Transition from surface-induced failure to internal defect (typically pores, but also inclusions and microstructural discontinuities) failure at $\sim 10^8$ cycles at room temperature and at $650 \text{ }^\circ\text{C}$
[128]	IN718	$R = 0.1$	HIP can be detrimental despite porosity reduction if microstructure contains brittle phases and inclusions, and if yield strength is reduced Shot-peening only improves fatigue life only if HIP was not done prior
[203]	IN718	$R = 0.1$	Double-ageing after HIP resulted in better fatigue life than HIP alone Performance was still worse than wrought since HIP could not close surface pores

Table 2 continued

Ref.	Material	Stress Ratio	Effect of porosity on fatigue life of LPBF Ti64
[204]	IN718		Surface pore closure with HIP was achieved by applying a Ni-20Cr coating prior After HIP and ageing, low-cycle fatigue life deteriorated as it was determined by microstructure and not porosity
[126]	316L	$R = 0.1,$ $-1$	Fatigue cracks initiate from the surface under the high cycle fatigue regime but under the very high cycle fatigue regime, cracks initiated from internal unmelted particles, inclusions or LoF pores
[127]	316L	$R = 0.1$	Fatigue cracks initiate from internal LoF pores under high loads, but from the surface under low loads (transition occurred at $\sim 10^5$ cycles)
[119]	316L	$R = 0.1$	Machining can expose sub-surface/internal porosity that can become responsible for fatigue failure Small sub-surface LoF pores (contour area) can dominate over much larger internal pores
[205]	316L	$R = -1$	Porosity increases the scatter in fatigue results which can mask other factors that influence fatigue life
[206]	316L	$R = -1$	Fatigue cracks that initiate at sub-surface pores propagate without much resistance as the as-built microstructural features are unable to act as barriers to crack propagation or arrest cracks
[176]	316L	$R = 0.1$	Samples with high porosity performed worse in fatigue tests as the fatigue life was driven by porosity Fatigue life of dense samples ( $\sim 1\%$ porosity, Archimedes method) was dictated by ductility under low-stress loading and by tensile strength at high-stress loading
[207]	316L	$R = 0.1$	Defects, sample orientation and surface quality are less influential in high-stress fatigue For low-stress fatigue, cracks initiate from sub-surface pores for machined or surface-treated samples
[101]	316L	$R = -1$	For low-stress amplitudes, vertically built samples have higher pore tolerance due to better hardening potential to withstand localized stresses At high-stress amplitudes, vertically built samples perform worse due to poor yield strength
[208]	316L	$R = -1$	Stress-relief can improve pore tolerance for horizontal samples to improve fatigue life, but this is effect is more limited on vertical samples
[188]	316L	$R = 0.1$	Horizontal samples perform better than vertical samples across all stress levels regardless of whether stress-relief treatment was done With machining, cracks initiated from sub-surface LoF pores. Otherwise, cracks initiated from the surface
[209]	316L	$R = 0.1$	Machining can improve fatigue life by reducing roughness, removing surface pores, and introducing compressive residual stresses
[210]	316L	$R = 0.1$	The presence of small LoF pores or gas pores are not critical for high-stress fatigue loading as this is microstructure-driven
[147]	316L	$R = 0.1$	A transition from porosity-driven fatigue failure (under fixed cyclic loading at 438 MPa) to a microstructural one was observed as density was improved from 98.88% to 99.92% A critical pore size causing this transition was proposed, which could be relative to the length scales of various localized microstructural features
[211]	316L	$R = -1$	Pore closure with HIP improves fatigue life at low-stress levels HIP limited fatigue improvements at higher-stress levels due to a substantial reduction in yield strength

Table 2 continued

Ref.	Material	Stress Ratio	Effect of porosity on fatigue life of LPBF Ti64
[212]	316L		Stress concentration effects relative to the loading axis are different for LoF pores and spherical pores Horizontally built samples had better fatigue life than vertically or diagonally built samples Large LoF pores are more critical than surface roughness or spherical pores The projected area occupied by the LoF pores relative to the loading plane generally reflected its fatigue life
[146]	316L	$R = -1$	Miniaturized fatigue samples free of defects were used to investigate microstructural effects on fatigue crack initiation and growth In the absence of significant porosity, cracks tend to initiate from dislocation interactions along slip bands The as-built cellular substructure caused by solute segregation as found to significantly delay fatigue crack initiation and crack growth Thermal treatments, including HIP, weakened fatigue life by eliminating the cellular substructure and coarsening the microstructure
[213]	AlSi10Mg	$R = 0.1$	Oxides can contribute LoF pore formation
[82, 130, 142, 213–215]	AlSi10Mg	$R = -1, 0, 0.1, 0.5$	LoF pores are more detrimental to vertically built samples
[216]	AlSi10Mg	$R = 0.1$	Porosity causes worse performance than cast AlSi10Mg
[217, 218]	AlSi10Mg	$R = -1$	With optimized LPBF parameter sets and good surface finish, LPBF AlSi10Mg can outperform wrought and machined Al6061 even with some LoF pores
[136–138]	AlSi10Mg	$R = -1$	Fatigue life can be predicted from pore size
[75]	AlSi10Mg	$R = -1$	Horizontal and vertical samples containing large LoF pores had similar fatigue performance HIP was unable to close the pores but could alter the localized geometries of the pores Localized geometrical features of the LoF pores were considered to be more critical than pore size or orientation due to stress concentration effects
[219]	AlSi10Mg	$R = -1$	LoF pores can be modeled as with simpler 3D shapes to predict fatigue life Porosity location and orientation must also be accounted for
[220]	AlSi10Mg	$R = 0$	LoF pores account for nearly all fatigue failure
[221]	AlSi10Mg	$R = -1$	LoF pores account for nearly all fatigue failure
[19]	AlSi10Mg	$R = -1$	Platform heating caused pores to be more spherical, leading to fatigue life improvements
[143]	AlSi10Mg	$R = -1$	Heat treatment resulted in poorer fatigue life in machined samples While cracks often initiate from surface/sub-surface pores, yield strength governed the fatigue life and globularization of Si was detrimental
[86]	AlSi10Mg	$R = 0.1$	While globularized Si can impede crack propagation, T6 was still found to be detrimental
[222]	AlSi10Mg	$R = 0.1$	Fatigue crack initiates either at a surface/sub-surface Si phase or pore
[218]	AlSi10Mg	$R = -1$	In near-net shaped samples (as-built, vibratory-polished or jet blasted surfaces), cracks initiated from surface pores In milled-finished samples, cracks initiated from internal pores
[18]	AlSi10Mg	$R = -1, 0, 0.5$	Internal porosity becomes more critical than surface quality or surface/sub-surface pores at very high-cycle fatigue (i.e., approaching $10^{10}$ cycles) Noted that fatigue performance is better when $R = -1$ possibly due to pore closure under compression
[20]	AlSi10Mg	$R = 0.1$	Sub-surface pores can be more detrimental than a rough as-built surface in low-cycle fatigue

Table 2 continued

Ref.	Material	Stress Ratio	Effect of porosity on fatigue life of LPBF Ti64
[144, 223]	AlSi10Mg	$R = 0.2, -1$	In fatigue tests under 400 °C, porosity was found to play a critical role Porosity is less critical at 400 °C as fatigue failure is caused by void formation due to Si particle coarsening
[141]	AlSi10Mg	$R = -1$	HIP reduced porosity by 64% and the average pore equivalent circle diameter by 11% HIP + ageing treatment resulted in better fatigue life than as-built Crack initiation occurred in sub-surface pores for as-built samples and in sub-surface coarsened Si or intermetallic precipitates in HIP + aged samples While coarsened precipitates caused crack initiation, they also impeded crack propagation
[224]	AlSi10Mg	$R = -1$	HIP can cause metal above sub-surface defects to deform inward, resulting in surface defects Additional surface machining after HIP is required to further improve fatigue life
[120]	AlSi10Mg	$R = 0.1$	Machining improves fatigue life, but pores exposed by machining will become responsible for fatigue failure
[121]	AlSi10Mg	$R = 0.1$	Improvements to fatigue life is limited by machining due to exposure of previously sub-surface/internal pores
[28]	AlSi10Mg	$R = -1$	Shot-peening can reduce sub-surface porosity and also causes the spheroidization of sub-surface LoF pores Shot-peening improved fatigue life
[225]	AlSi10Mg	$R = -1$	Improvement to fatigue life by shot-peening was attributed to compressive surface stresses rather than any influence on surface/sub-surface porosity
[226, 227]	AlSi10Mg	$R = 0.1$	Friction stir welding as a surface treatment was found to improve fatigue life by closing surface pores and globularizing the Si phase
[142]	AlSi10Mg	$R = 0.1$	Heat treatment that coarsens the Si phase improves fatigue life

surface/sub-surface pores are generally more critical at high-cycle fatigue. However, as the stress loading is further reduced (i.e., very high-cycle fatigue), it appears that there is another transition toward bulk porosity (or other defects) being critical, as was observed in [122–124] for Ti64, in [125] for IN718, in [18] for AlSi10Mg and in [126] for 316L. However, it is unclear if this is always true for LPBF 316L as Solberg et al. showed that under higher loads (still in the high-cycle fatigue regime), fatigue cracks initiated from internal LoF pores, but as load decreased, crack initiation occurred from the surface [127]. This can potentially be explained by the fact that their samples contained significant amounts of large LoF pores (~ 5.4% porosity, CT method) [127]. While the authors did not mention the material's yield strength, they noted an ultimate tensile strength of 437 MPa, which is noticeably lower than the expected yield strength of optimal LPBF 316L samples (refer to Fig. 12). Even though the cycles to failure for all samples were above  $10^4$  and were classified as high

cycle fatigue by the authors, the samples that failed from internal LoF pores were tested above ~ 280 MPa. It is likely that the high localized stress-concentrations surrounding the irregular LoF pores caused fatigue cracks to initiate from these pores as opposed to from the surface at these higher high loads.

Therefore, when considering post-processing treatments, the intended fatigue application must be considered. For example, if cracks initiate from surface or sub-surface pores, then surface treatment might be more useful than HIP. However, if cracks are initiated from internal pores, then HIP becomes more relevant. This is best illustrated by the studies by Benedetti et al. as shown in Fig. 23 [122, 123] on LPBF Ti64. Below the very high-cycle fatigue regime, introducing surface compressive stresses (i.e., via shot-peening) is much more beneficial to fatigue performance relative to bulk pore closure as surface/sub-surface pores/features are more critical. However, for very high-cycle fatigue performance,



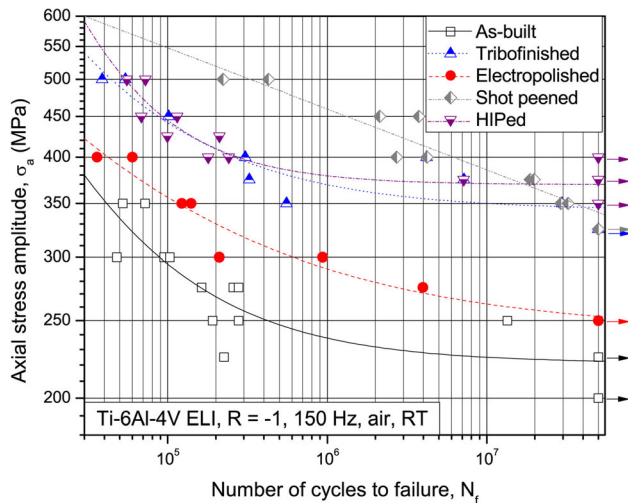


**Figure 23** Fatigue results of a study that investigated the effects of various surface finishing on LPBF Ti64 for the purposes of biomedical applications. It should be noted that all samples were subjected to a stress-relief heat treatment of 670 °C for 5 h, and electropolishing, shot peening and HIP were all performed after a tribofinish. Reproduced with permission from [122] (Copyright 2017, Elsevier).

porosity closure across the entire cross-section using HIP becomes far more effective since internal porosity becomes more critical. Similarly, for LPBF IN718, Ardi et al. found that despite porosity reduction through HIP (0.39% to 0.08%), room temperature high-cycle fatigue performance worsened due to microstructural changes while shot-peening improved fatigue life [128]. In fact, they found that HIP and shot-peening resulted in far worse fatigue life. The results are shown in Fig. 24.

Furthermore, if it is known that within a particular fatigue regime, surface/sub-surface pores are more critical than internal pores, this can also be used to improve the building speeds of LPBF components. This was highlighted by Andreau et al. where they showed that the fatigue life of LPBF 316L was very tolerant of, or generally unaffected by, the presence of internal porosity levels of up to 10% (CT method) provided the sub-surface region was sufficiently dense (which was achieved through contouring) [119]. In other words, as long as the sub-surface regions are built with highly optimized parameters, the bulk of a component can be built with faster parameters since some amount of internal porosity can be tolerated if internal pores are not critical.

As with tensile performance, LoF pores have also been found to be far more damaging to fatigue

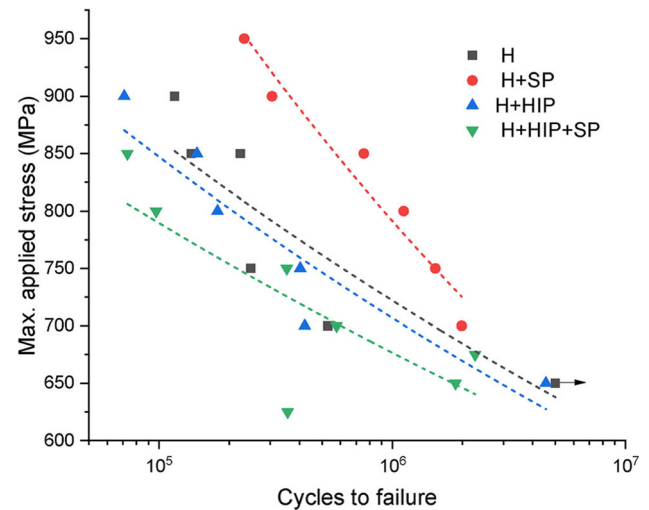
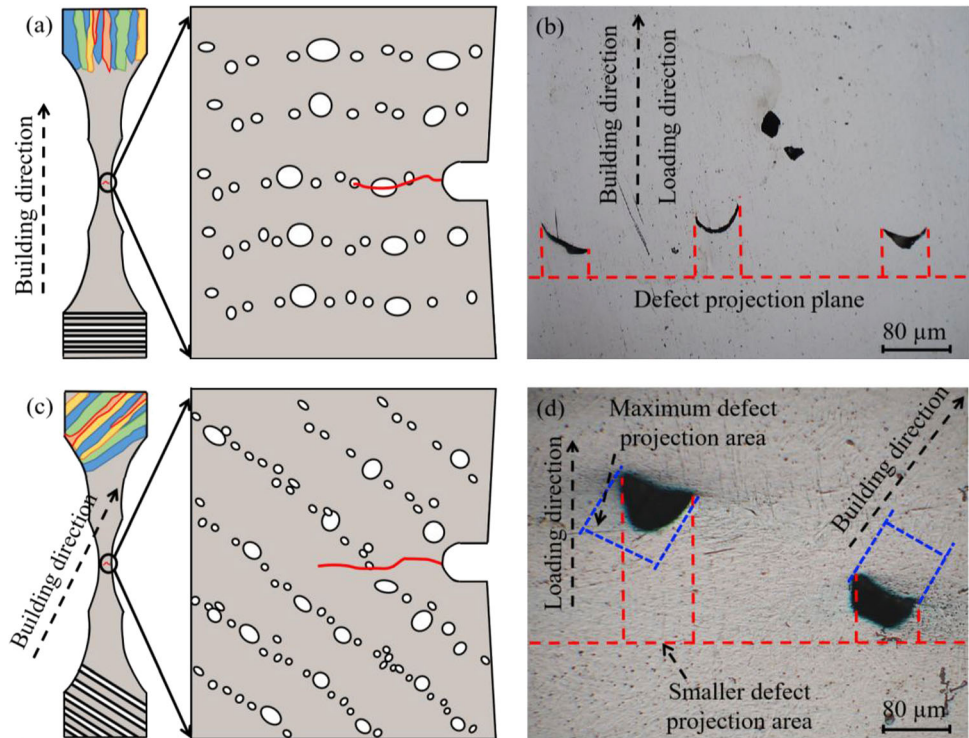


**Figure 24** Peak stress vs cycle-to-failure (S–N) plot for different types of LPBF IN718 specimens with trend lines superimposed. The black arrow indicates run-out, H stands for heat-treated (solution-treatment followed by double ageing) and SP stands for shot-peening. Reproduced with permission from [128] (Copyright 2020, Elsevier). The authors investigated HIP after standard heat treatment because a single build plate is often heat-treated after LPBF while containing a mixture of critical and non-critical components, but HIP is only needed to be performed on critical components and can often only be done after removal from the build plate.

performance, especially for vertical samples, mainly due to their irregular shape and size. This is illustrated in Fig. 25 from the LPBF Ti64 study by Xu, Liu and Wang, which shows how crack propagation is much easily facilitated by the LoF pores in vertically built samples than in diagonally built samples [129]. Similarly, Xu et al. explain that LoF pores are more detrimental to vertically built LPBF AlSi10Mg samples because of their location at melt-pool boundaries which can facilitate crack propagation during fatigue, as shown in Fig. 26 [130]. For horizontal samples, Bao et al., illustrates how LoF pores evolve during a fatigue test at 250 °C for LPBF AlSi10Mg, which is mainly driven by coalescence leading to micro-cracks as shown in Fig. 27 [131].

While a poor surface finish can often be responsible for fatigue failure, Watring et al. demonstrated that if the porosity level is high enough, sub-surface porosity can still become critical, as is shown in Fig. 28 [132]. With increasing porosity, the fatigue failure transition from being dictated by surface roughness (which is affected by building orientation) to one being driven by sub-surface porosity—namely

**Figure 25** Influence of sample orientation on the interlayer porosity distribution in LPBF Ti64 where (a) illustration showing the interlayer pore distribution in a vertically built sample, (b) shows an OM image of such LoF pores in a vertically built sample, (c) illustration showing the interlayer pore distribution in a diagonally built sample, and (d) shows an OM image of such LoF pores in a diagonally built sample. Reproduced with permission from [129] (Copyright 2019, Elsevier) where the authors investigated the effect of build direction on fatigue crack propagation behavior.



LoF and keyhole for low and high energy density parameters, respectively.

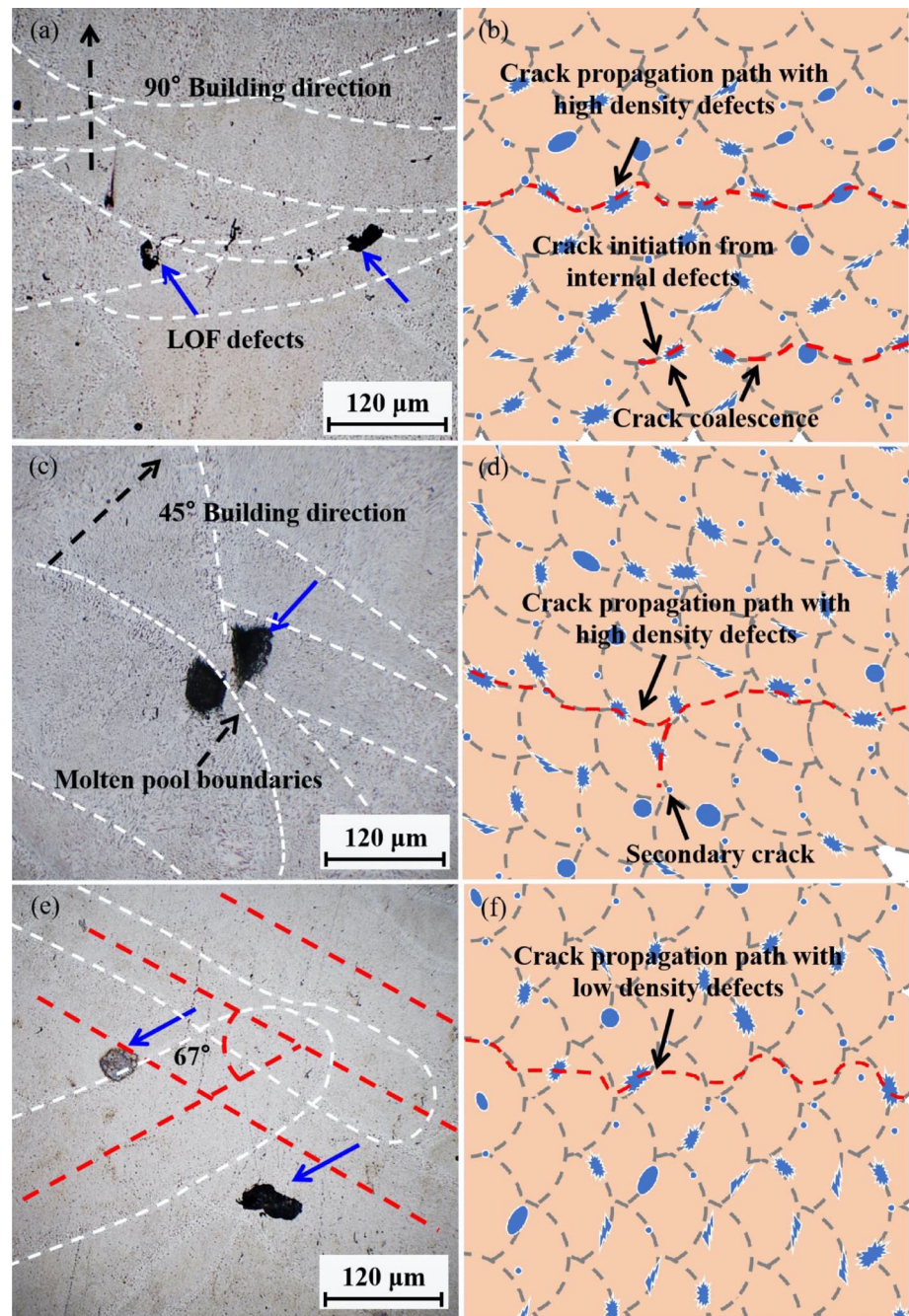
Assuming that pores cannot be closed and are unavoidable, some other strategies can also be used for the design of LPBF components in fatigue applications and to predict fatigue behavior based on the porosity present. Edwards and Ramulu suggested that a coarser LPBF Ti64 microstructure might improve ductility at the expense of strength could suppress crack initiation from the pores [133] and Kumar and Ramamurty proposed incorporating a damage tolerant design approach to LPBF Ti64 components [134]. In trying to solve the mismatch between the real size of a pore and its true effect on fatigue performance, Masuo et al. proposed that the effective area approach of considering an irregular-shaped pore or a cluster of pores for LPBF Ti64, as estimated from a fracture mechanics standpoint, as illustrated in Fig. 29 [135]. Other authors have also shown that fatigue life can be predicted on the basis of pore size, as shown in Fig. 30 by Ngnekou et al. for LPBF AlSi10Mg [136, 137], where process-induced pores were analyzed, but the data were also supplemented with machined defects, and in Fig. 31 by Romano et al., also for LPBF AlSi10Mg [138].

It should also be stated that for age-hardenable alloys, namely IN718 and AlSi10Mg, hard brittle

precipitates may be beneficial or detrimental to fatigue life since they can be considered defects as well as obstacles to dislocations and/or crack propagation. Wan et al. showed that after standard heat treatments of LPBF IN718, micro-crack formation preferentially occurs on the acicular  $\delta$  phase adjacent to a critical pore [139]. Since the ability for an initiated crack to propagate through the  $\delta$  phase is dependent on its width, if it is sufficiently fine, formed cracks would be too small to propagate into the matrix and the phase would then be able to resist dislocation movement (in a similar way to the  $\gamma$  and  $\gamma''$  precipitates) and lead to improved fatigue life. A similar finding was also confirmed by Luo et al. [140]. Similarly, the HIP and ageing study on LPBF AlSi10Mg by Schneller et al. [141] noted that while coarsened Si particles can act as crack initiation sites if competing pores are small enough, they can also impede crack propagation. On the other hand, in the as-built condition, because the fine dendritic Si phase confers high strength but easily facilitates crack propagation, the loss of this microstructure through a conventional heat treatment (where the Si phase is dissolved through solution treatment and subsequent ageing causes it to reprecipitate as coarse discrete particles) may improve fatigue life if the improved resistance to crack propagation more than compensates for the



**Figure 26** Influence of melt-pool boundaries and LoF distribution on the fatigue crack propagation in LPBF AlSi10Mg fabricated (a, b) vertically, (c, d) diagonally, (e, f) horizontally. Reproduced with permission from [130] (Copyright 2020, Elsevier) where the authors investigated the influence of porosity and build directions on the high cycle fatigue performance of stress-relieved (520 °C, 2 h) LPBF AlSi10Mg.



corresponding reduction in load bearing capacity due to reduced strength [142]. This dichotomy explains why ageing treatment was found to be beneficial in [142] but detrimental in [86, 143]. An interesting study by Bao et al. shows that the coarsening of the Si phase during a fatigue test at 400 °C can actually result in void formation that leads to fatigue failure, while fatigue life at lower temperatures was driven by existing porosity, as illustrated in Fig. 32 [144].

As the interaction between porosity and microstructure is particularly complex for the age-hardenable LPBF alloys with regards to fatigue life, post-heat treatment processes to modify hard precipitates are particularly crucial. In general, it is beneficial for the hard phases to be discontinuous since a dendritic morphology promotes crack propagation (as with the as-built Si morphology in AlSi10Mg as mentioned prior, and also with the Laves phase in as-built IN 718 [139]) while a discrete

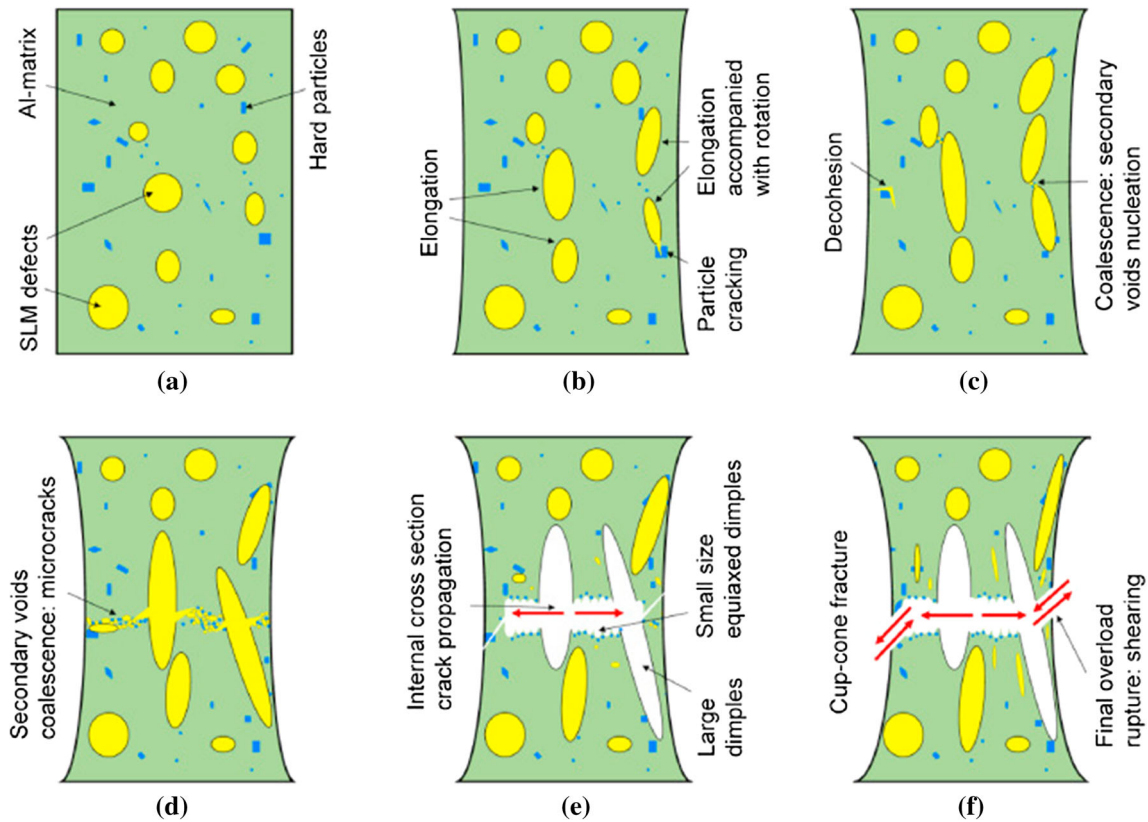
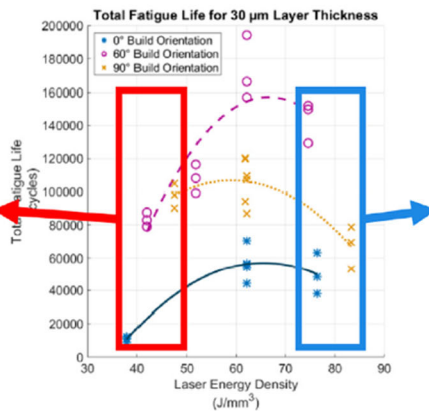
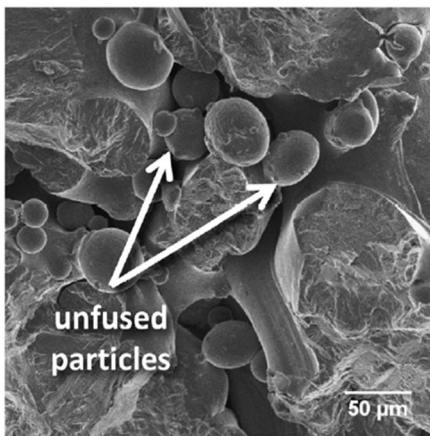


**Figure 27** Pore evolution (yellow) in LPBF AlSi10Mg during low cycle fatigue at 250 °C—(a) initial state of the samples, (b) elongation of large pores due to longitudinal strain, (c) coalescence of adjacent pores, (d) cracks initiate at the cross-section, (e) void nucleation and (f) fracture. Reproduced with permission from [131] (Copyright 2020, Elsevier).

Low energy densities



High energy densities

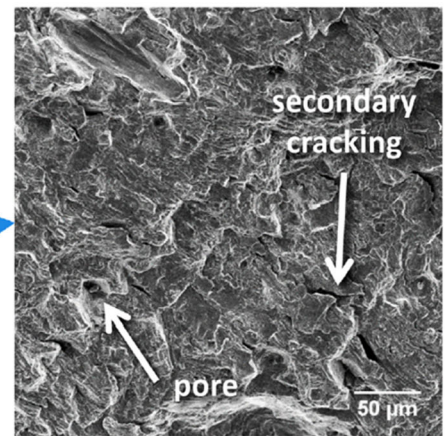


**Figure 28** High-cycle fatigue life (600 MPa,  $R = 0.1$ , 20 Hz) versus volumetric laser-energy density for 30  $\mu\text{m}$  layer thickness specimens as reproduced with permission from [132] (2019, Elsevier) where the authors investigated the effects of LPBF parameters and surface roughness on the high cycle fatigue

behavior of as-built LPBF IN718. The sample orientations are relative to the re-coater direction. Outside of the optimal energy density range, poor fatigue life is caused by sub-surface defects—namely, LoF pores if the energy density is too low, and keyhole pores and secondary cracking if the energy density is too high.



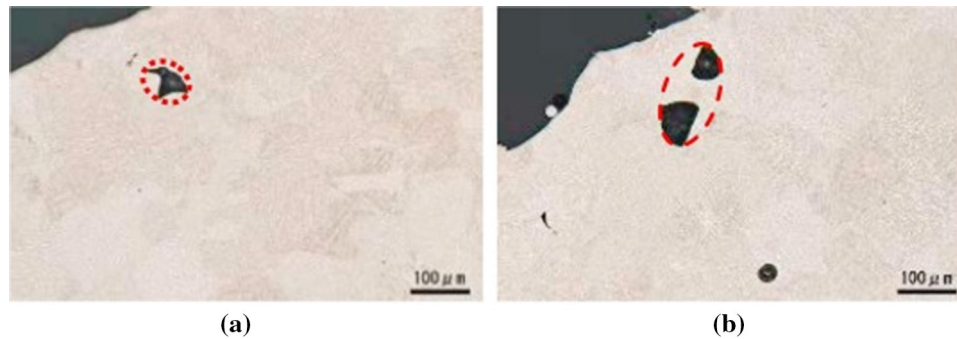


**Figure 29** Examples of the effective area estimations for (a) an irregular-shaped pore and (b) a cluster of two pores where the distance between them is smaller than the size of the smaller pore. Reproduced with permission from [135] (Copyright 2018,

Elsevier) where the authors studied the effects of surface roughness and porosity, as well as the role of HIP, on the fatigue strength of LPBF Ti64.

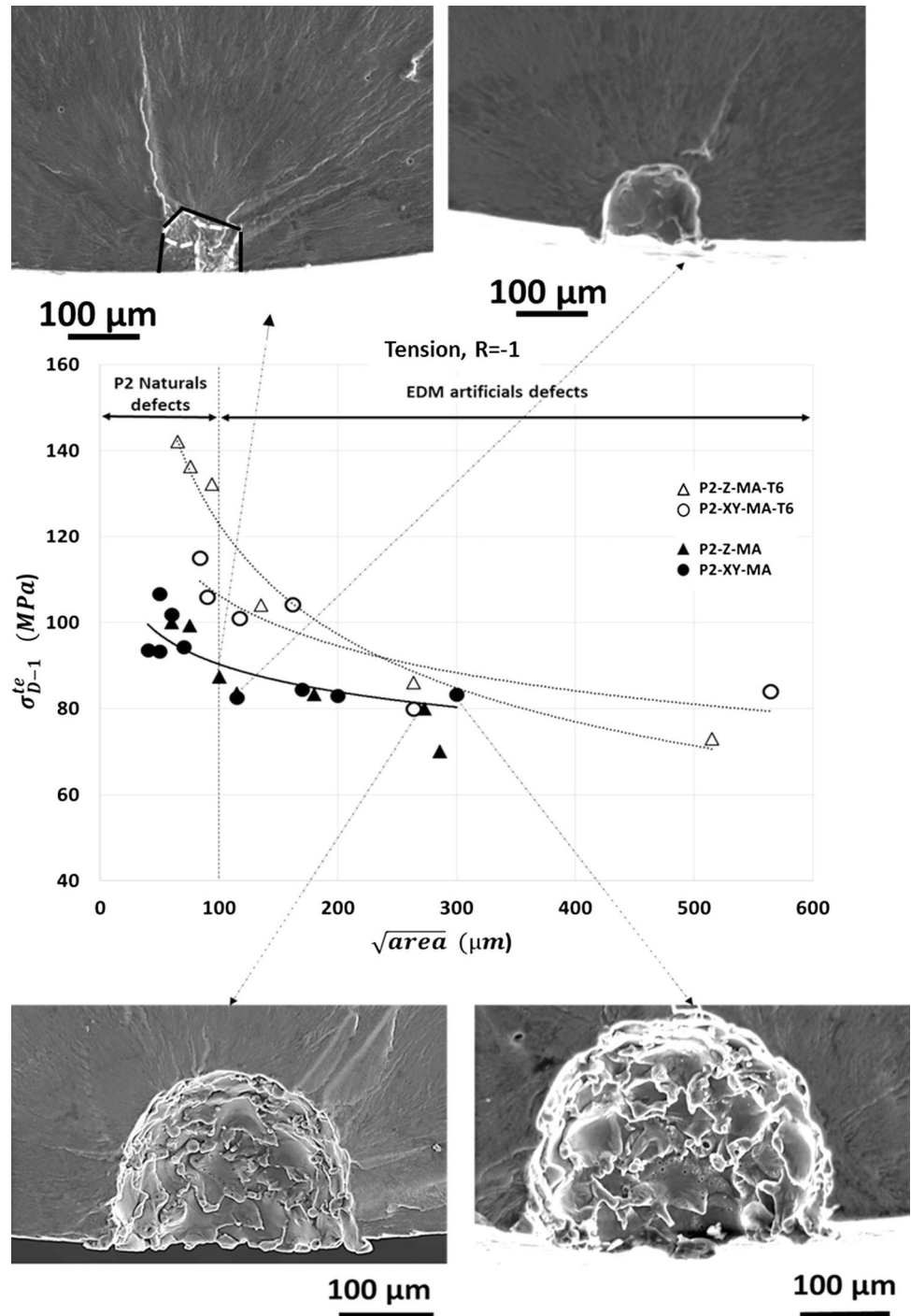
morphology improves fatigue life by being impediments to dislocation movement and crack propagation. However, the main concern with hard phases appears to be their role in facilitating crack initiation especially when interacting with an existing pore. If the pores in a given alloy are much smaller than sizes of the hard precipitates, crack initiation could simply occur from the precipitate itself. In this case, further reduction in pore size and amount (using HIP for instance) may not yield any improvement in fatigue life. This was demonstrated by Ardi et al. on LPBF IN718 where pore closure via HIP resulted in fatigue cracks originating from Nb-rich precipitates which then limited fatigue improvements [128]. It should be noted, however, that the authors did not perform the ageing treatment after HIP. If the hard phase is much smaller than the pores, then the precipitates located at the vicinity of a pore may be subjected to higher localized stresses and thus, result in micro-cracking. As the degree of cracking is dependent on the precipitate size, further reductions in size would lead to smaller and potentially non-consequential crack initiation [139]. Since, unlike the other three alloys, HIP can be implemented into the typical heat treatment cycles for LPBF IN718 to improve strength, as was noted in the preceding section, it stands to reason that LPBF IN718 can benefit the most from this process in terms of improving fatigue life.

As for LPBF Ti64, assuming that a fatigue crack is initiated due to microstructural features (i.e., not from an existing pore, inclusion or surface roughness), it is likely that the initiation would occur along the  $\alpha$  and  $\beta$  phase boundaries, as noted by Yan et al. [145]. Nonetheless, for high cycle fatigue, the authors noted that porosity (or defects) played the dominant

role in crack initiation, while variations in microstructure were primarily responsible for the rate at which the fatigue crack grew, with a coarser  $\alpha$  and  $\beta$  microstructure attributed to a slower growth rate. Naturally, the reduced strength brought about by the coarser microstructures tends to lead to poorer low cycle fatigue performance.

On the other hand, since LPBF 316L is predominantly a single-phase face-centered cubic alloy, if fatigue cracks are initiated due to microstructural features, they are likely to preferentially form along slip bands caused by the gliding of dislocations, as noted by Elangeswaran et al. [146]. The authors then proposed that if the alloy retains its cellular substructure caused by the segregation of solute atoms during LPBF production, this substructure can hinder the flow of dislocations such that the time required for dislocations to glide over a sufficient distance to accrue the required strain energy for crack initiation is increased, thus improving crack initiation life. Additionally, once initiated, the substructure also restricts the crack growth rate by deflecting its path. Most notably, the authors also showed HIP can be detrimental to fatigue life because this process removes the cellular substructure and, due to the high ductility of 316L, this alloy is already highly tolerant of (small) pores which might render pore closure unnecessary. Naturally, this only holds true if the pores are already sufficiently small such that cracks are initiated from microstructural features (indeed, the authors of the study specifically used miniaturized fatigue samples that are essentially free of porosity), and this could explain why, as summarized in Table 2, some LPBF 316L studies reported porosity-driven fatigue failure and others reported

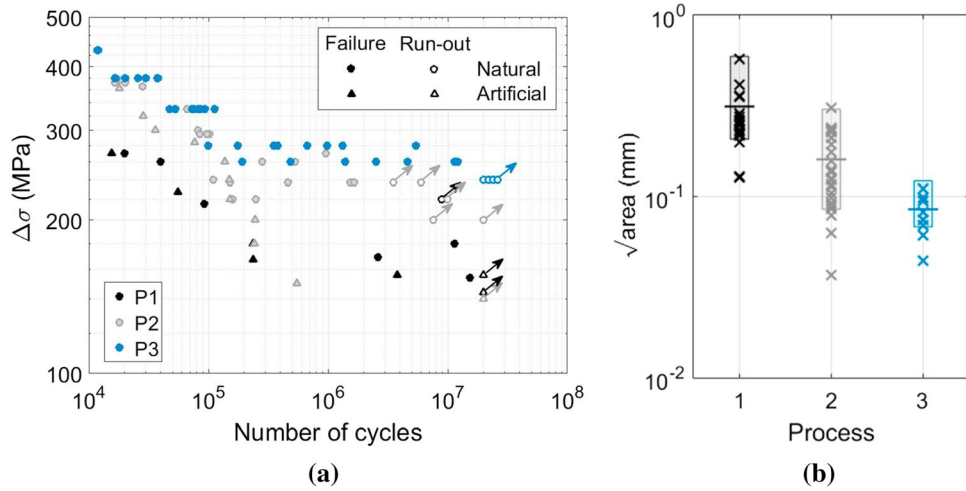
**Figure 30** Kitagawa-type diagram showing the relationship between the critical pore size and the fatigue life of LPBF AlSi10Mg. Some of the samples tested had a pore artificially machined into the sample using electric discharge machining. Reproduced with permission from [137] (Copyright 2019, Elsevier) where the authors investigated the effect of pore size on the fatigue behavior of stress-relieved (210 °C, 1 h or 300 °C, 2 h), as well as T6-treated, LPBF AlSi10Mg parts.



microstructure-driven failure. Most notably, Zhang et al. demonstrated a transition from porosity-driven fatigue failure to a microstructure-driven one as the alloy’s density increased from 98.88 to 99.92% [147].

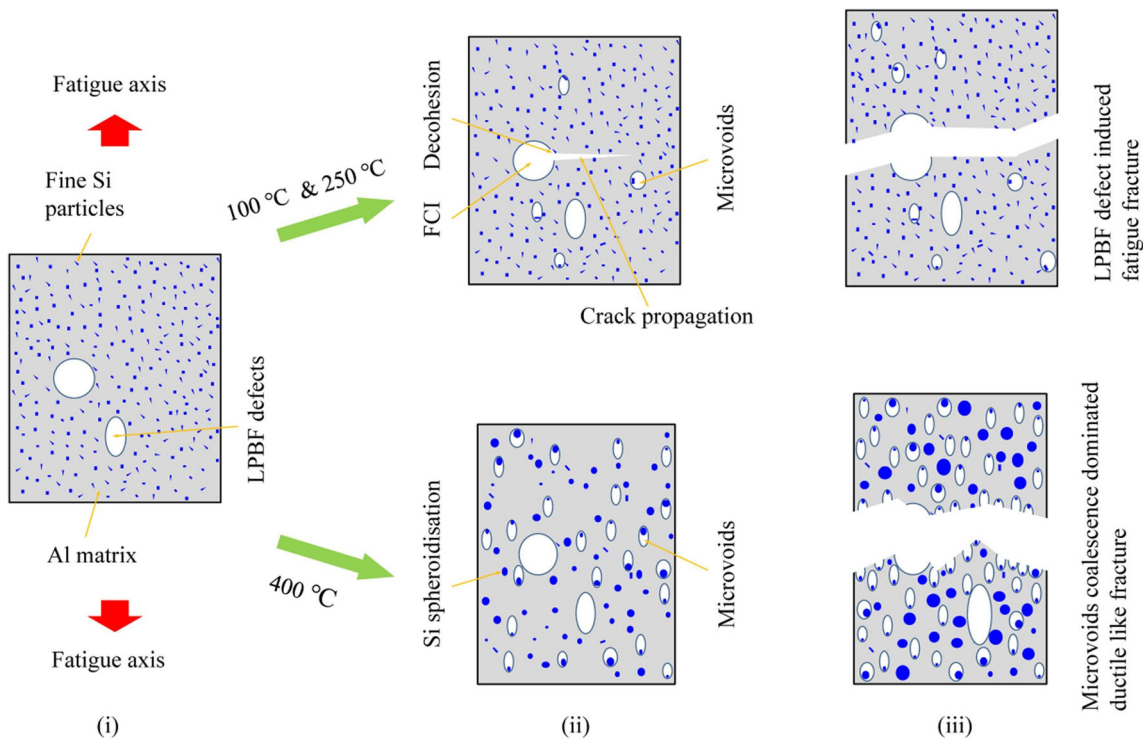
### Impact and fracture toughness

Table 3 summarizes the influence of porosity on impact and fracture toughness of the LPBF alloys discussed in this review as reported in recent literature. LoF pores are frequently noted to be particularly detrimental to crack propagation for both impact and fracture toughness, especially in samples where the



**Figure 31** (a) The S–N curve of the fatigue results ( $R = -1$ ) with the critical pore responsible for failure either from a process-induced pore or a machined pore and, (b) the relative pore sizes of the critical pores. Reproduced with permission from [138]

(Copyright 2018, Elsevier) where the authors developed a defect-based modeling approach to predict the fatigue strength of machined LPBF AlSi10Mg parts.



**Figure 32** Illustration of how existing process-induced pores in LPBF AlSi10Mg are responsible for fatigue failure in low-temperature tests while at 400 °C, the formation of voids due to Si coarsening become responsible for fatigue failure. Reproduced

with permission from [144] (Copyright 2021, Elsevier) where the authors investigated high temperature dwelling effects on the fatigue behavior of stress-relieved (300 °C, 2 h) LPBF AlSi10Mg parts.

crack propagation path runs parallel to these pores (typically vertically built notched samples). For example, Wu, Lai and Chen illustrated how LoF pore orientation could result in anisotropic notched

Charpy impact energy due to the way the pores interact with the fracture plane as shown in Fig. 33 [148]. The detrimental influence of porosity in Charpy impact tests is frequently attributed to

**Table 3** Observations of how porosity affects impact and fracture toughness of LPBF alloys either as reported or inferred from recent literature

Ref.	Alloy	Influence of porosity on impact/fracture toughness
[25]	Ti64	Investigated horizontally built samples with porosity up to 14% A sharp reduction in Charpy impact toughness with increasing pore fraction was observed
[148]	Ti64	For a given pore fraction, samples with LoF pores have much lower toughness than those with spherical pores LoF pores are much more detrimental to vertically built Charpy samples than horizontally built ones (4.9 J vs 9.6 J) Attributed to a substantially greater proportion of the cross-sectional area occupied by pores
[110]	Ti64	HIP reduced pores from 0.7% to 0.2% Substantially improved toughness attributed to microstructure Reduced isotropy attributed to pore reduction
[149]	Ti64	Coalescence of pores, and the formation and coalescence of new voids, were the main mechanisms of crack initiation in as-built and stress-relieved un-notched Charpy samples
[148]	Ti64	Vertically built samples had approximately half the fracture toughness ( $K_{IC}$ ) of horizontally built samples (65 MPa $\sqrt{m}$ , 118 MPa $\sqrt{m}$ and 132 MPa $\sqrt{m}$ , for the ZX, YX and XZ samples, respectively) Attributed to porosity, surface finish and cracks
[110]	Ti64	Porosity likely reduced fracture toughness through stress concentration points causing crack initiation
[154]	Ti64	Noted that vertically built samples should have a lower $K_Q$ but found that horizontally built samples performed slightly worse due to microstructural reasons caused by cooling rate with respect to building height
[152]	IN718	No trend in impact toughness with respect to porosity level
[150]	IN718	HIP reduced the porosity level from 1.10% to 0.06% HIP improved room temperature and cryogenic impact toughness, but the LPBF sample still performed worse than wrought IN718 Fracture path preferentially went through unmelted particles in LoF pores
[115]	IN718	Fracture toughness ( $K_Q$ ) worsened after HIP + solution treatment + double ageing despite pore closure Attributed to grain coarsening and precipitation hardening
[170]	316L	Absorbed energies of < 70 J reported in literature are due to high levels of porosity Good build qualities tend to report greater than 130 J If yield strength > 700 MPa and with ~ 0.2% porosity, toughness > 200 J can be achieved
[207]	316L	Commented that low porosity was crucial in achieving a high impact toughness (~ 150 J)
[153]	316L	Increasing density from 99.93% to 99.99% via HIP worsened toughness, attributed to the annealing effect
[14]	316L	Higher yield strength attributed to poorer fracture toughness ( $K_Q$ : 63 – 87 MPa $m^{0.5}$ ) as compared to conventional 316L ( $K_{IC}$ : 112 – 278 MPa $m^{0.5}$ ) Interconnected pores also found in the LPBF samples Fracture toughness was lower when notch was oriented parallel to melt-pool boundaries. Could be due to LoF pores located along these boundaries promoting crack propagation
[228]	316L	Commented that the result in [14] could be attributed to porosity in the LPBF samples Showed that near-fully dense samples (> 99.5% density) had better $J_{IC}$ as compared to wrought 316L due to superior resistance to crack initiation
[17]	316L	Vertical samples (ZX) had the poorest fracture toughness, horizontal XZ samples the best Results were attributed to tensile stress–strain response XZ samples were also noted to contain lower porosity
[130]	AlSi10Mg	$K_{IC}$ calculated from fatigue fracture surfaces for vertical, diagonal and horizontal samples were 12.8 MPa $m^{0.5}$ vs 13.1 MPa $m^{0.5}$ and 14.0 MPa $m^{0.5}$ , respectively LoF pores along melt-pool boundaries aided crack propagation in vertical samples
[151]	AlSi10Mg	Horizontal Charpy samples contain more gas pores but performed better than vertical samples due to microstructural reasons—cracks go across rather than along melt-pool boundaries Pores enlarged during T6 caused toughness to decrease and horizontal samples now performed worse than vertical samples Attributed to pores causing cracks to deviate from their usual path and the reduced load-bearing section area HIP + T6 mitigated the pore growth issue, but Si coarsening limited toughness improvements



Table 3 continued

Ref.	Alloy	Influence of porosity on impact/fracture toughness
[75]	AlSi10Mg	Charpy samples contained significant LoF pores, which introduced stress concentration sites As-built vertical samples performed better than horizontal ones due to microstructural reasons—as-built Si network impedes crack propagation in the former, resulting in increased tolerance of the LoF pores After T6, vertical samples performed worse due to LoF pore orientation facilitating crack propagation Results being contrary to [151] could be due to the differences in the nature of porosity which can also cause differences in the preferred crack propagation path

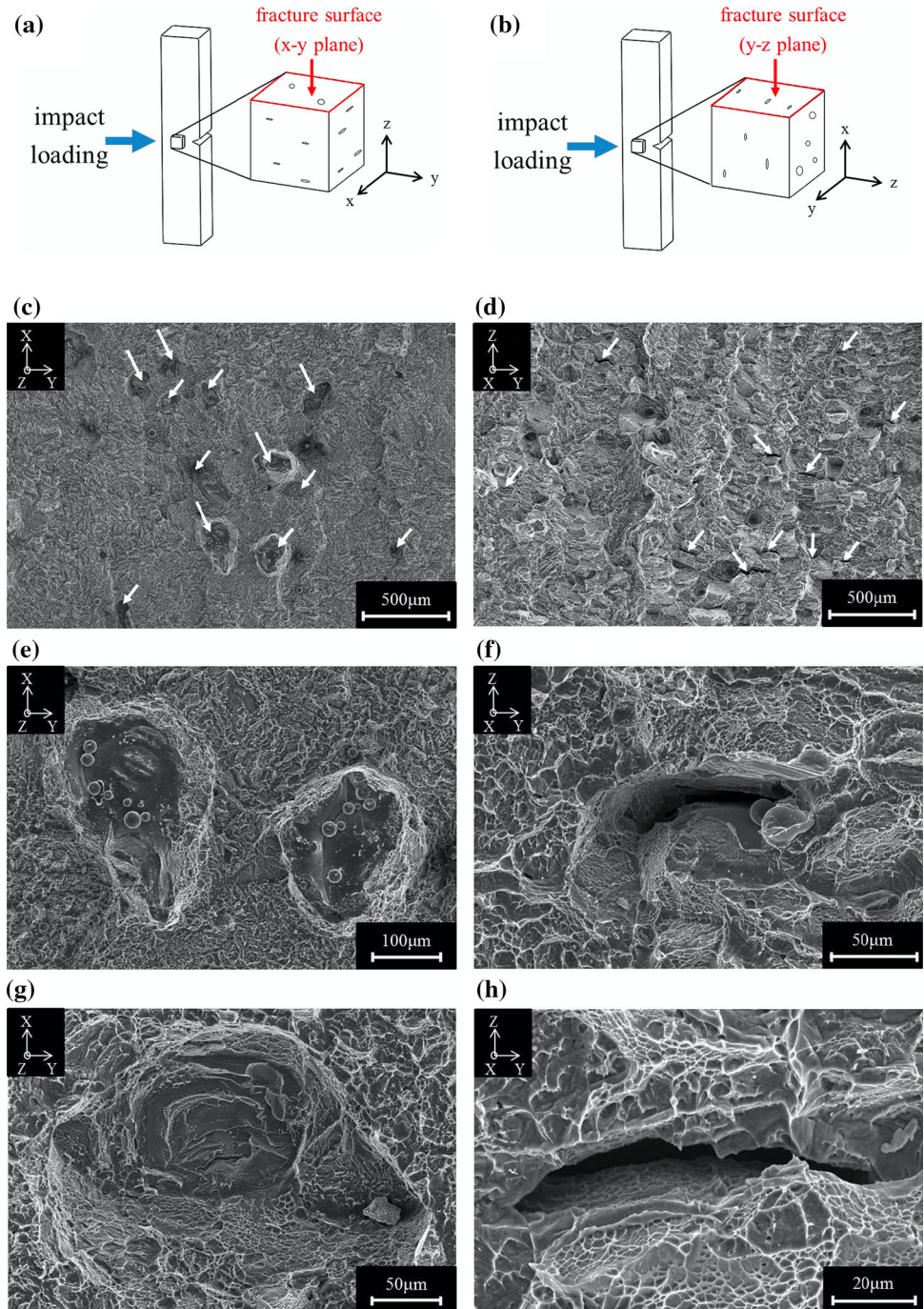
(i) coalescence of porosity during impact [149], (ii) altering of the crack propagation path from one based on microstructure toward one based on porosity distribution [150, 151], (iii) increased stress-concentration effects [75], and (iv) a substantial reduction in the actual cross-sectional area occupied by material that is available to absorb impact energy [148]. Thus, when Wang et al. surveyed existing literature on the impact toughness of LPBF 316L and found a wide scatter in the impact toughness, as shown in Fig. 34, the authors noted that studies reporting absorbed energies of 70 J or less were a result of high levels of porosity (or cracking issues) while studies with better build quality tend to report much higher (more than 130 J) absorption energies. The authors then demonstrated that it was possible to achieve toughness exceeding 200 J and yield strength exceeding 700 MPa at ~ 0.2% porosity.

Once again, as with the tensile results, if porosity is sufficiently low, microstructural effects might dominate the toughness results and the amount of energy absorbed might not correlate with minor variations in porosity, which could explain results reported by Ardila et al. for LPBF IN718 [152]. Likewise, as the Charpy impact study by Girelli et al. on LPBF AlSi10Mg shows, the crack path is affected by the melt-pool contours in the as-built condition but can be affected by porosity after heat treatment due to pore growth [151]. Similarly, Kan et al. showed that for as-built vertical AlSi10Mg Charpy samples where the LoF pores are supposed to be extremely detrimental, the nano-crystalline Si network was able to impede crack propagation more effectively, allowing it to surpass the horizontal samples [75]. Conversely, as shown by Reijonen et al. on LPBF 316L samples without HIP performed better than HIPed samples due to a finer microstructure despite having more porosity [153].

As with impact toughness, the following reasons are often provided to explain the detrimental nature of pores to fracture toughness such as (i) LoF pores promoting crack propagation along melt-pool boundaries [130], and (ii) increased stress concentration points [110]. Again, the negative influence of porosity on fracture toughness can sometimes be compensated with microstructure. For instance, in [154] where Hartunian and Eshraghi found that the vertical LPBF Ti64 samples performed better than horizontal samples despite LoF pores being present because of microstructure variations caused by the LPBF cooling rate on the latter, and in [115] where Seifi et al. found that double-ageing without prior HIP resulted in better fracture toughness despite a higher porosity level and the presence of LoF pores due to microstructural reasons.

While porosity reduction strategies are clearly beneficial for both impact and fracture toughness, microstructural features must also be considered. However, this can be complicated by the fact that heat treatments often involve trade-offs between strength and ductility, but both can be important factors here. Additionally, melt-pool contours obviously play a crucial role in crack propagation. Furthermore, this is unlike in fatigue where specific strategies can be used to improve performance depending on the fatigue regime of interest. Therefore, in this regard, more work needs to be done to understand how the unique LPBF microstructures influence impact and fracture toughness in light of the presence of porosity, and how heat treatment may be able to help mitigate these issues.

**Figure 33** Illustration of how sample orientation affects the crack propagation path relative to the orientation of the LoF pores in (a) vertical and (b) horizontal LPBF Ti64 samples. SEM images of the fracture surfaces at different magnifications showing the morphologies of the exposed LoF pores where (c, e, g) are from a vertical sample and (d, f, h) are from a horizontal sample. The white arrows in (c) and (d) indicate the location of the pores. Adapted with permission from [148] (Copyright 2016, Elsevier) where the authors investigated the anisotropic impact toughness behavior of LPBF Ti64.



### Creep response

Creep studies that discuss the influence of porosity on performance are few in literature, with Table 4 summarizing recent studies on the topic. Among the alloys reviewed in this article, IN718, being a superalloy, is intended to be used for high-temperature applications. Thus, creep studies are most relevant for this alloy and typically, large grains and grain

boundary strengthening precipitates are generally preferred [155]. As can be observed in the table, growth and coalescence of pores are often responsible for creep failure [155, 156]. Additionally, pores can also act as crack initiation sites that lead to premature creep fracture [155, 157]. For example, Xu et al. investigated the effect of heat treatment (homogenization, solution treatment and single-ageing) and surface finish on creep behavior of LPBF IN718 at

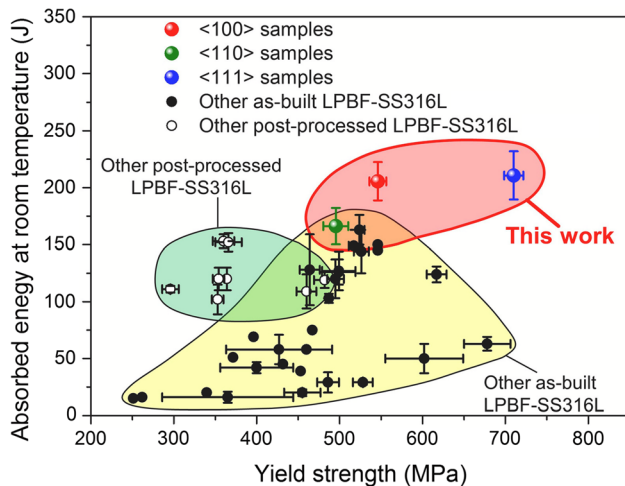


**Figure 34** Relationship between toughness and yield strength of LPBF 316L in literature as surveyed by, and reproduced with permission from, [170] (Copyright 2021, Elsevier) where the authors studied the effect of crystallographic orientation of LPBF 316L parts on Charpy impact toughness.

750 MPa and 650 °C, and found that while cracks often originate from the surface (with pre-existing cracks also caused by machining), porosity in the material can grow, coalescence and eventually lead to the fracture of the cross-section as illustrated in Fig. 35 [155]. In a separate study, they captured the evolution of porosity at various stages of creep

(650 °C, 747.45 MPa) using  $\mu$ -CT, as shown in Fig. 36 [156].

In general, there is a lack of understanding of how process-induced pores truly affect the creep performance of these alloys. For instance, it is uncertain how the overall porosity level can affect creep life and whether there is a certain threshold where microstructural features can dominate over the porosity level. One example would be a study like the one on LPBF 316L by Bae et al. as shown in Fig. 37 [157]. The authors found that the creep behavior was closely related to the density of the sample tested. Sample B06, especially, had the largest amount of process-induced pores which resulted in a tear very early in the creep test. As LPBF-processing results in unique microstructures not observed in conventional processing, an understanding of microstructural features that can provide greater tolerance of porosity needs to be developed for these alloys. Furthermore, beyond pores facilitating crack initiation and contributing to coalescence, the influence on load-bearing area is also rarely discussed. The effect of specific pore types—keyhole, LoF and gas pores, is also not very well known. Thus, for the alloys discussed herein, there remains a substantial amount of work that can be done to relate the detrimental nature of

**Table 4** Observations of how porosity affects creep response of LPBF alloys either as reported or inferred from recent literature

Ref.	Alloy	Effect of porosity on creep response
[155]	IN718	While cracks can initiate from the surface, existing pores can grow, coalescence and eventually lead to the fracture of the cross-section
[229]	IN718	Pore closure through HIP can be beneficial to creep as this can inhibit crack nucleation
[156]	IN718	Growth in pore size occurs more prominently in earlier stages of creep New pore formation typically occurs and becomes more apparent at later stages Localized porous regions within a sample (due to scan strategy and part geometry) can act as fracture initiation points during creep
[157]	316L	Creep behavior is closely related to sample density High levels of porosity act as crack initiation sites that result in a tear at the early stages of creep
[230]	316L	Horizontal samples performed worse than vertical samples Horizontal samples were found to contain more LoF pores
[231–233]	316L	Pores result in worse creep performance by accelerating creep cavitation damage
[234]	AlSi10Mg	Fracture surfaces revealed LoF pores Authors commented that the pores only occupied a small fraction of the cross-section and were unlikely to have affected the load-bearing area significantly
[235]	AlSi10Mg	Commented that the larger pores observed after creep testing were thermally induced pores Based on fractography images of the room temperature samples, it is likely that the thermally induced pores started as gas pores and grew during high-temperature creep



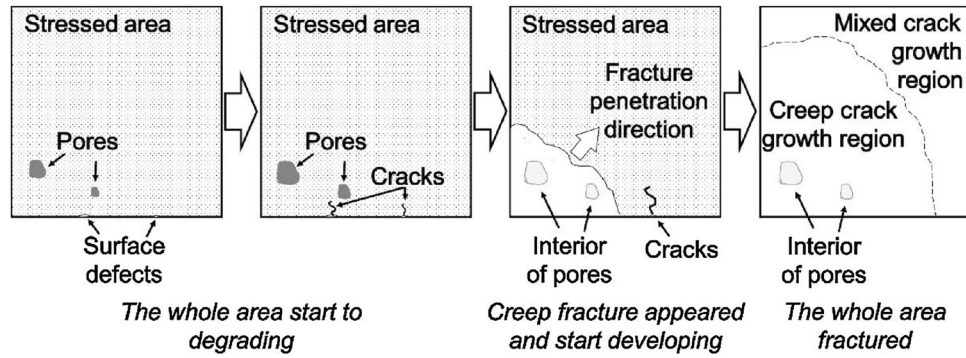


**Figure 35** Schematic showing the development of fractures during creep testing as reproduced with permission from [155] (Copyright 2018, Elsevier) where the authors investigated the

creep behavior of LPBF IN718 parts at 650 °C after homogenization, solution and double ageing treatments.

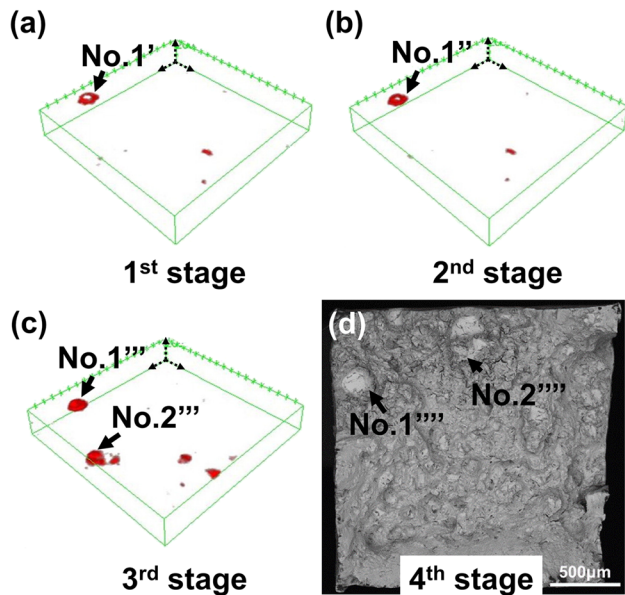


**Figure 36** Visualizations in porosity evolution at various stages of a creep test where (a–c) are 3D  $\mu$ -CT models taken after Stages 1–3 of the test, respectively, and (d) is the SEM image of the fracture surface at the end of the fourth stage. Adapted with permission from [156] (Copyright 2017, Elsevier) where the authors studied the effects of porosity on the creep behavior of LPBF IN718 parts using staged thermomechanical testing.

LPBF process-induced pores to creep life and performance.

### Wear behavior

Table 5 summarizes recent wear studies on where the influence of porosity was discussed or mentioned. It is important to state that wear is not an intrinsic material property, but it depends on the entire

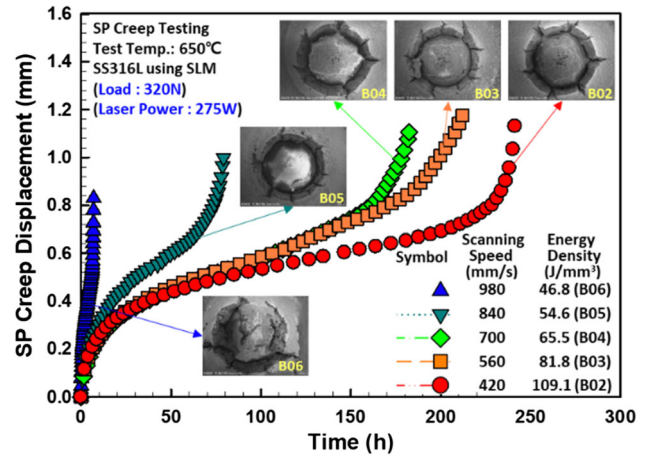


**Figure 37** Creep test results of LPBF 316L fabricated using different energy densities. Samples B02, B03, B04, B05 and B06 had densities of 7.88, 7.88, 7.85, 7.82 and 7.60 g/cm<sup>3</sup>, respectively. Reproduced with permission from [157] (Copyright 2021, Springer Nature) where the authors investigated the effects of different LPBF parameters on the creep behavior of LPBF 316L parts.

tribological system involved. In this regard, it is not surprising that studies have reported porosity to be detrimental, negligible or even beneficial. Regarding studies that report a negative influence, porosity is often stated to (i) increase friction [158, 159], (ii) increase contact pressure by reducing the actual contact area across a sliding interface [79, 160], (iii) reduce bulk hardness [161], and/or promote crack initiation and propagation [79, 160, 162, 163]. For instance, Li, Ramezani and Chen proposed that the amount of strain experienced (and therefore, the wear mechanisms involved) during wear loading or hardness testing of LPBF Ti64 can be related to its stress–strain behavior, as illustrated in Fig. 38, and



**Table 5** Observations of how porosity affects wear behavior of LPBF alloys either as reported or inferred from recent literature

Ref.	Alloy	Test Type	Effect of porosity on wear behavior
[158]	Ti64	Sliding	Ultrasonic nanocrystal surface modification (UNSM) is able to reduce surface roughness, increase surface hardness, and close surface pores Wear rate improvement was attributed to increased hardness and friction reduction was attributed to a smoother surface and pore closure
[162]	Ti64	Sliding	Ultrasonic surface rolling closed surface pores and increased surface hardness Pore closure improves wear performance by minimizing stress concentration points and reducing crack propagation probability
[161]	Ti64	Sliding	Wear rate can be related to stress–strain tensile behavior Porosity can influence hardness, which can then affect wear performance
[103]	Ti64	Sliding	In samples containing up to $\sim 0.27\%$ porosity (CT), wear rate and friction coefficient were not correlated with the porosity level or micro-hardness
[236]	Ti64	Sliding	$\sim 1.8\%$ porosity had no influence of wear rate or friction
[237]	IN718	Sliding	Wear rate and friction found to be lower in samples with lower porosity Role of porosity was not discussed as sliding performance was related to microstructure and hardness
[24]	IN718	Sliding	Wear rate decreased after HIP + solution treatment + double ageing Improved performance was attributed mainly to microstructural changes and improved hardness, with closure of pores noted Bottom section of samples had worse wear performance than middle and top sections. This was attributed to open pores
[163]	316L	Sliding	In samples containing up to 6.7% porosity, cracks tend to initiate and propagate from pre-existing pores, resulting in micro-fracturing being the dominant wear mechanism
[238]	316L	Sliding	Against a hard counterpart, pores can reduce bonding between melt-pools resulting in cracks that accelerate wear
[239]	316L	Sliding	The presence of porosity results in poorer sliding wear performance
[159]	316L	Sliding	Suggested that an ideal smooth surface free of porosity can minimize friction and wear
[160]	316L	Sliding	Porosity increases contact stresses by reducing the real contact area during sliding wear Pores can act as crack initiation sites during sliding Surface deformation as a post-treatment step can improve wear resistance by reducing sub-surface porosity and increase hardness
[240]	316L	Sliding	Used UNSM to close surface pores, reduce roughness and improve hardness Wear rate and friction were both reduced
[26, 164, 165]	316L	Sliding	Pores were proposed to improve wear resistance by trapping wear debris that could be compacted and cold-welded into the pores
[241]	316L	Cavitation Erosion	Large pores act as stress-concentration sites and can facilitate crack propagation Irregular-shaped pores can contain material fragments that are torn apart by cavitation-induced impact
[242]	316L	Erosion Corrosion	Small pores in LPBF 316L can result in weaker re-passivation Despite higher hardness and better pitting resistance, pores cause poorer erosion-corrosion compared to conventional 316L
[243]	316L	Cavitation Erosion	Argued that even if all pores could be removed, the elongated grain morphology would still promote cavitation-induced crack propagation
[244]	316L	Particle Erosion	LPBF 316L performed worse than wrought 316L regardless of impingement angle Poor performance generally attributed to porosity
[79]	AlSi10Mg	Sliding	Sub-surface LoF pore orientation can affect crack propagation leading to delamination Surface LoF pore orientation can alter the actual contact area and thus, the contact stresses The influence of porosity is also affected by sliding test conditions and microstructure
[21]	AlSi10Mg	Sliding	T6 treatment can cause an increase in porosity, resulting in LPBF AlSi10Mg performing worse than cast AlSi10Mg despite similar hardness
[245]	AlSi10Mg	Fretting Fatigue	Numerical study shows that sub-surface gas pores can be detrimental Commented that experiments are required to confirm findings

Table 5 continued

Ref.	Alloy	Test Type	Effect of porosity on wear behavior
[246]	AlSi10Mg	Cavitation Erosion	LoF pores in LPBF samples resulted in a much higher initial erosion rate due to rapid removal of unmelted powder Samples with lower porosity had lower wear losses at this stage After the initial erosion period, all LPBF samples stabilized at similar erosion rates Overall, all LPBF samples outperformed wrought AlSi10mg due to their higher hardness

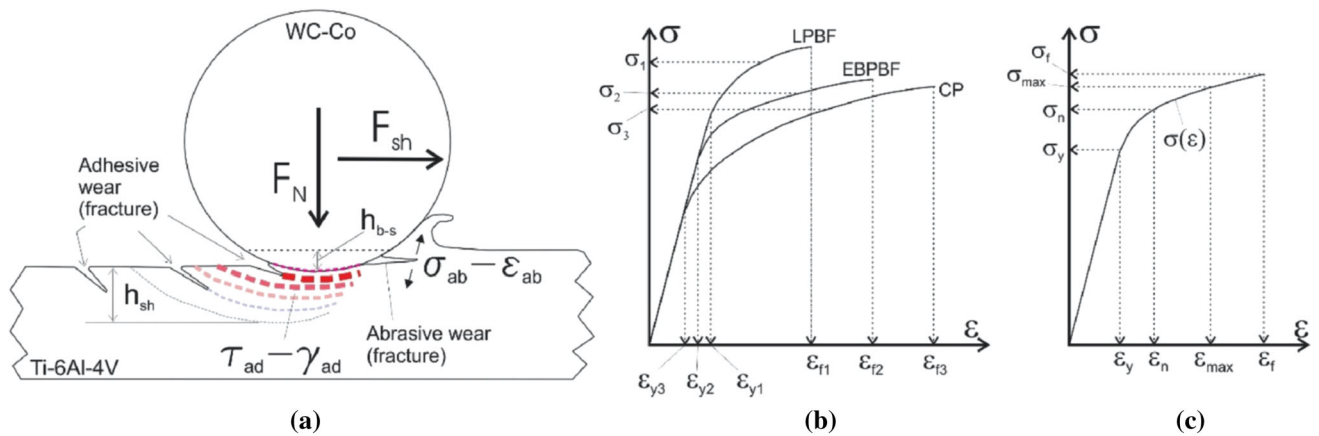


Figure 38 Schematic illustration of (a) force, stress and strain interactions during a sliding wear test which can result in adhesive or abrasive wear of Ti64 in relation to the (b) stress–strain behavior and (c) hardness response of LPBF, electron beam PBF

and conventionally processed Ti64. Reproduced with permission from [161] (Copyright 2019, Elsevier) where the authors studied the dry sliding wear behavior of LPBF Ti64 parts against WC–Co.

hardness can be significantly affected by porosity [161]. Conversely, Kan et al. illustrated how the orientation of surface LoF pores relative to the sliding direction could alter the actual contact area across the sliding interface, as shown in Fig. 39a and b [79]. Similarly, the degree of crack propagation facilitated by a sub-surface LoF pore can also be affected by its orientation, as illustrated in Fig. 39c and d.

As for the beneficial influence that porosity can play, Huang et al. found that LPBF 316L generally displayed better sliding wear resistance against GCr15 than wrought 316L and they proposed that the presence of pores in the former improved its wear resistance because worn debris could be trapped, compacted and cold welded into the pores [164]. However, it is plausible that the LPBF 316L could have performed well despite containing porosity by virtue of it being harder than the wrought 316L. Nonetheless, other studies have reported the phenomenon [26, 165]. The exact reason for this to occur

is not clear, though the fact that it is reported for LPBF 316L rather than the other alloys suggests that ductility could be playing a role. Certainly, more studies can be done to investigate the influence of porosity across a wider range of wear systems and loading conditions so as to identify the situations where wear performance is or is not severely affected by porosity.

### Concluding remarks

After a review of the literature on the influence of process-induced porosity on the mechanical properties of four alloys commonly produced by LPBF, broad general observations can be made. LoF pores are more detrimental among various pore types and affect vertically built samples more. Reducing porosity, however, only improves tensile properties up to a point, beyond which microstructural effects

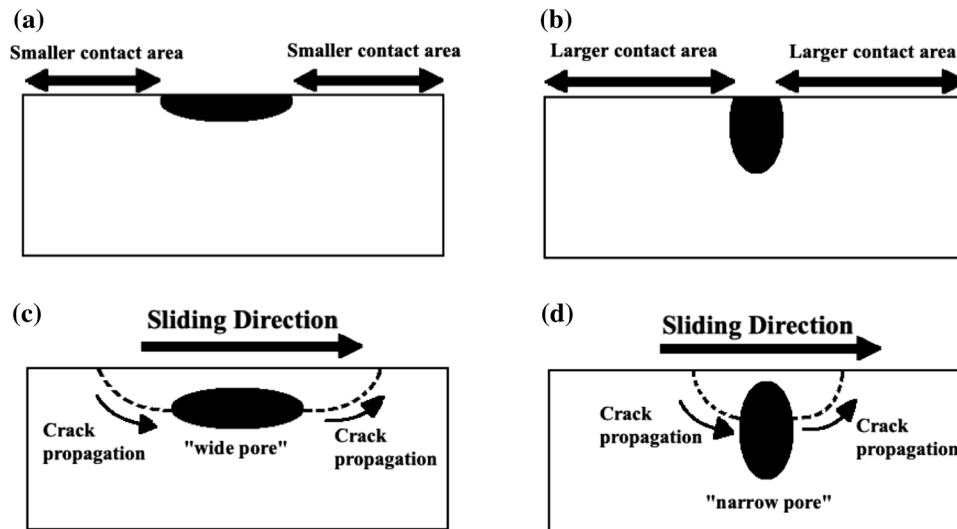


**Figure 39** Influence of LoF pore orientation on sliding wear interactions in LPBF AlSi10Mg where (a) and (b) shows how a surface pore orientation relative to the sliding interface can result in differences in the actual contact area across the sliding interface and therefore, the contact stresses experienced by the alloy, and

(c) and (d) shows how the orientation of a sub-surface pore can facilitate sub-surface cracking. Reproduced with permission from [79] (Copyright 2021, Elsevier) where the authors studied the effects of T6 treatment on the sliding wear performance of LPBF AlSi10Mg parts sliding against SiC and steel.

dominate. Where porosity compromises tensile properties, elastic modulus and strength are primarily affected by the morphology and amount of the pores rather than specific microstructure–porosity interactions, while total elongation is much more sensitive to the presence of porosity though the degree of sensitivity is dependent on the alloy's toughness or ductility. In most cases, assuming a good surface finish, fatigue behavior appears to be governed by strength under high-stress loading, but as the loading decreases, surface/sub-surface pores become critical. When the loading is decreased sufficiently, bulk porosity starts to matter. Thus, depending on the intended fatigue application, an appropriate post-processing treatment can be chosen to improve service life. The main microstructural considerations that affect fatigue life in relation to the presence of pores are also different for each alloy—the morphology and size of hard precipitates in IN718 and AlSi10Mg,  $\alpha$  and  $\beta$  boundary interactions for Ti64 and dislocation interactions along slip bands for 316L. Impact and fracture toughness are negatively affected by bulk porosity, but care must be taken to close the pores via HIP because these properties are also affected by the combination of strength and ductility. The presence of pores can also affect these properties by altering the crack propagation path from the original microstructure-directed path.

As for creep, while porosity is known to be detrimental, studies that specifically relate pore type, size, amount, and orientation to creep life are lacking. Lastly, the majority of wear studies noted the detrimental nature of pores and some noted that porosity (assuming its low enough) can be negligible. A small number of studies noted that porosity can be beneficial, though the conditions for this to be true are unclear.

## Funding

Open Access funding enabled and organized by CAUL and its Member Institutions. The authors did not receive any funding for this work.

## Declarations

**Conflict of interest** The authors also declare that there are no conflicting relationships or interests that have influenced this work.

**Open Access** This article is licensed under a Creative Commons Attribution 4.0 International License, which permits use, sharing, adaptation, distribution and reproduction in any medium or format, as long as you give appropriate credit to the original

author(s) and the source, provide a link to the Creative Commons licence, and indicate if changes were made. The images or other third party material in this article are included in the article's Creative Commons licence, unless indicated otherwise in a credit line to the material. If material is not included in the article's Creative Commons licence and your intended use is not permitted by statutory regulation or exceeds the permitted use, you will need to obtain permission directly from the copyright holder. To view a copy of this licence, visit <http://creativecommons.org/licenses/by/4.0/>.

## References

- [1] ASTM (2015) ASTM52900-15 standard terminology for additive manufacturing—general principles—terminology. ASTM Int West Conshohocken
- [2] Tuncer N, Bose A (2020) Solid-state metal additive manufacturing: a review. *JOM* 72:3090–3111. <https://doi.org/10.1007/s11837-020-04260-y>
- [3] Zhang B, Li Y, Bai Q (2017) Defect formation mechanisms in selective laser melting: a review. *Chin J Mech Eng* 30(3):515–527. <https://doi.org/10.1007/s10033-017-0121-5>
- [4] Kok Y, Tan XP, Wang P, Nai MLS, Loh NH, Liu E, Tor SB (2018) Anisotropy and heterogeneity of microstructure and mechanical properties in metal additive manufacturing: a critical review. *Mater Des* 139:565–586. <https://doi.org/10.1016/j.matdes.2017.11.021>
- [5] Guraya T, Singamneni S, Chen ZW (2019) Microstructure formed during selective laser melting of IN738LC in key-hole mode. *J Alloys Compd* 792:151–160. <https://doi.org/10.1016/j.jallcom.2019.03.419>
- [6] Cunningham R, Narra SP, Montgomery C, Beuth J, Rollett A (2017) Synchrotron-based X-ray microtomography characterization of the effect of processing variables on porosity formation in laser power-bed additive manufacturing of Ti-6Al-4V. *JOM* 69(3):479–484. <https://doi.org/10.1007/s11837-016-2234-1>
- [7] Montalbano T, Briggs BN, Waterman JL, Nimer S, Peitsch C, Sopcisak J, Trigg D, Storck S (2021) Uncovering the coupled impact of defect morphology and microstructure on the tensile behavior of Ti-6Al-4V fabricated via laser powder bed fusion. *J Mater Process Technol* 294:117113. <https://doi.org/10.1016/j.jmatprotec.2021.117113>
- [8] Giovagnoli M, Silvi G, Merlin M, Di Giovanni MT (2021) Optimisation of process parameters for an additively manufactured AlSi10Mg alloy: limitations of the energy density-based approach on porosity and mechanical properties estimation. *Mater Sci Eng A* 802:140613. <https://doi.org/10.1016/j.msea.2020.140613>
- [9] Yi JH, Kang JW, Wang TJ, Wang X, Hu YY, Feng T, Feng YL, Wu PY (2019) Effect of laser energy density on the microstructure, mechanical properties, and deformation of Inconel 718 samples fabricated by selective laser melting. *J Alloys Compd* 786:481–488. <https://doi.org/10.1016/j.jallcom.2019.01.377>
- [10] Snell R, Tammam-Williams S, Chechik L, Lyle A, Hernández-Nava E, Boig C, Panoutsos G, Todd I (2020) Methods for rapid pore classification in metal additive manufacturing. *JOM* 72(1):101–109. <https://doi.org/10.1007/s11837-019-03761-9>
- [11] Wilson-Heid A, Novak T, Beese A (2019) Characterization of the effects of internal pores on tensile properties of additively manufactured austenitic stainless steel 316L. *Exp Mech* 59(6):793–804. <https://doi.org/10.1007/s11340-018-00465-0>
- [12] Wang P, Tan X, He C, Nai MLS, Huang R, Tor SB, Wei J (2018) Scanning optical microscopy for porosity quantification of additively manufactured components. *Addit Manuf* 21:350–358. <https://doi.org/10.1016/j.addma.2018.03.019>
- [13] Romano S, Abel A, Gumpinger J, Brandão AD, Beretta S (2019) Quality control of AlSi10Mg produced by SLM: Metallography versus CT scans for critical defect size assessment. *Addit Manuf* 28:394–405. <https://doi.org/10.1016/j.addma.2019.05.017>
- [14] Suryawanshi J, Prashanth KG, Ramamurthy U (2017) Mechanical behavior of selective laser melted 316L stainless steel. *Mater Sci Eng A* 696:113–121. <https://doi.org/10.1016/j.msea.2017.04.058>
- [15] Tapia G, Elwany AH, Sang H (2016) Prediction of porosity in metal-based additive manufacturing using spatial Gaussian process models. *Addit Manuf* 12:282–290. <https://doi.org/10.1016/j.addma.2016.05.009>
- [16] Liverani E, Toschi S, Ceschini L, Fortunato A (2017) Effect of selective laser melting (SLM) process parameters on microstructure and mechanical properties of 316L austenitic stainless steel. *J Mater Process Technol* 249:255–263. <https://doi.org/10.1016/j.jmatprotec.2017.05.042>
- [17] Alsalla HH, Smith C, Hao L (2018) Effect of build orientation on the surface quality, microstructure and mechanical properties of selective laser melting 316L stainless steel. *Rapid Prototyp J* 24(1):9–17. <https://doi.org/10.1108/RPJ-04-2016-0068>
- [18] Jian ZM, Qian GA, Paolino DS, Tridello A, Berto F, Hong YS (2021) Crack initiation behavior and fatigue performance up to very-high-cycle regime of AlSi10Mg fabricated by selective laser melting with two powder sizes. *Int J*



- Fatigue 143:106013. <https://doi.org/10.1016/j.ijfatigue.2020.106013>
- [19] Awd M, Siddique S, Johannsen J, Emmelmann C, Walther F (2019) Very high-cycle fatigue properties and microstructural damage mechanisms of selective laser melted AlSi10Mg alloy. *Int J Fatigue* 124:55–69. <https://doi.org/10.1016/j.ijfatigue.2019.02.040>
- [20] Yang KV, Rometsch P, Jarvis T, Rao J, Cao S, Davies C, Wu X (2018) Porosity formation mechanisms and fatigue response in Al-Si-Mg alloys made by selective laser melting. *Mater Sci Eng A* 712:166–174. <https://doi.org/10.1016/j.msea.2017.11.078>
- [21] Tonolini P, Montesano L, Tocci M, Pola A, Gelfi M (2021) Wear behavior of als10mg alloy produced by laser-based powder bed fusion and gravity casting. *Adv Eng Mater* 2100147. <https://doi.org/10.1002/adem.202100147>
- [22] Mfusi BJ, Mathe NR, Tshabalala LC, Popoola PA (2019) The effect of stress relief on the mechanical and fatigue properties of additively manufactured AlSi10Mg parts. *Metals* 9(11):1216. <https://doi.org/10.3390/met9111216>
- [23] Shen H, Rometsch P, Wu X, Huang A (2020) Influence of gas flow speed on laser plume attenuation and powder bed particle pickup in laser powder bed fusion. *JOM* 72(3):1039–1051. <https://doi.org/10.1007/s11837-020-04020-y>
- [24] Holland S, Wang X, Chen J, Cai W, Yan F, Li L (2019) Multiscale characterization of microstructures and mechanical properties of Inconel 718 fabricated by selective laser melting. *J Alloys Compd* 784:182–194. <https://doi.org/10.1016/j.jallcom.2018.12.380>
- [25] Kan WH, Gao M, Zhang X, Liang E, Chiu NSL, Lim CVS, Huang A (2022) The influence of porosity on Ti-6Al-4V parts fabricated by laser powder bed fusion in the pursuit of process efficiency. *Int J Adv Manuf Technol* 1–22. <https://doi.org/10.1007/s00170-021-08374-8>
- [26] Shin W-S, Son B, Song W, Sohn H, Jang H, Kim Y-J, Park C (2021) Heat treatment effect on the microstructure, mechanical properties, and wear behaviors of stainless steel 316L prepared via selective laser melting. *Mater Sci Eng A* 806:140805. <https://doi.org/10.1016/j.msea.2021.140805>
- [27] Lavery NP, Cherry J, Mehmood S, Davies H, Girling B, Sackett E, Brown SGR, Siens J (2017) Effects of hot isostatic pressing on the elastic modulus and tensile properties of 316L parts made by powder bed laser fusion. *Mater Sci Eng A* 693:186–213. <https://doi.org/10.1016/j.msea.2017.03.100>
- [28] Damon J, Dietrich S, Vollert F, Gibmeier J, Schulze V (2018) Process dependent porosity and the influence of shot peening on porosity morphology regarding selective laser melted AlSi10Mg parts. *Addit Manuf* 20:77–89. <https://doi.org/10.1016/j.addma.2018.01.001>
- [29] Sanaei N, Fatemi A (2021) Defects in additive manufactured metals and their effect on fatigue performance: a state-of-the-art review. *Prog Mater Sci* 117:100724. <https://doi.org/10.1016/j.pmatsci.2020.100724>
- [30] Al-Maharma AY, Patil SP, Markert B (2020) Effects of porosity on the mechanical properties of additively manufactured components: a critical review. *Mater Res Expr* 7:122001. <https://doi.org/10.1088/2053-1591/abcc5d>
- [31] du Plessis A, Yadroitsava I, Yadroitsev I (2020) Effects of defects on mechanical properties in metal additive manufacturing: a review focusing on X-ray tomography insights. *Mater Des* 187:108385. <https://doi.org/10.1016/j.matdes.2019.108385>
- [32] Song B, Zhao X, Li S, Han C, Wei Q, Wen S, Liu J, Shi Y (2015) Differences in microstructure and properties between selective laser melting and traditional manufacturing for fabrication of metal parts: a review. *Front Mech Eng* 10(2):111–125. <https://doi.org/10.1007/s11465-015-0341-2>
- [33] Lewandowski JJ, Seifi M (2016) Metal additive manufacturing: a review of mechanical properties. *Annu Rev Mater Res* 46:151–186. <https://doi.org/10.1146/annurev-matsci-070115-032024>
- [34] Harun WSW, Kamariah MSIN, Muhamad N, Ghani SAC, Ahmad F, Mohamed Z (2018) A review of powder additive manufacturing processes for metallic biomaterials. *Powder Technol* 327:128–151. <https://doi.org/10.1016/j.powtec.2017.12.058>
- [35] Harun WSW, Manam NS, Kamariah MSIN, Sharif S, Zulkifly AH, Ahmad I, Miura H (2018) A review of powdered additive manufacturing techniques for Ti-6Al-4V biomedical applications. *Powder Technol* 331:74–97. <https://doi.org/10.1016/j.powtec.2018.03.010>
- [36] Sing SL, An J, Yeong WY, Wiria FE (2016) Laser and electron-beam powder-bed additive manufacturing of metallic implants: a review on processes, materials and designs. *J Orthop Res* 34(3):369–385. <https://doi.org/10.1002/jor.23075>
- [37] Gorsse S, Hutchinson C, Gouné M, Banerjee R (2017) Additive manufacturing of metals: a brief review of the characteristic microstructures and properties of steels, Ti-6Al-4V and high-entropy alloys. *Sci Technol Adv Mater* 18(1):584–610. <https://doi.org/10.1080/14686996.2017.1361305>
- [38] Cao S, Zou Y, Lim CVS, Wu X (2021) Review of laser powder bed fusion (LPBF) fabricated Ti-6Al-4V: process, post-process treatment, microstructure, and property. *Light Adv Manuf* 2(2):1–20. <https://doi.org/10.37188/lam.2021.020>

- [39] Shipley H, McDonnell D, Culleton M, Coull R, Lupoi R, O'Donnell G, Trimble D (2018) Optimisation of process parameters to address fundamental challenges during selective laser melting of Ti-6Al-4V: a review. *Int J Mach Tools Manuf* 128:1–20. <https://doi.org/10.1016/j.ijmachtools.2018.01.003>
- [40] Liu S, Shin YC (2019) Additive manufacturing of Ti6Al4V alloy: a review. *Mater Des* 164:107552. <https://doi.org/10.1016/j.matdes.2018.107552>
- [41] Cao F, Zhang T, Ryder MA, Lados DA (2018) A review of the fatigue properties of additively manufactured Ti-6Al-4V. *JOM* 70(3):349–357. <https://doi.org/10.1007/s11837-017-2728-5>
- [42] Agius D, Kourousis KI, Wallbrink C (2018) A review of the as-built SLM Ti-6Al-4V mechanical properties towards achieving fatigue resistant designs. *Metals* 8(1):75. <https://doi.org/10.3390/met8010075>
- [43] Fotovvati B, Namdari N, Dehghanghadikolaei A (2018) Fatigue performance of selective laser melted Ti6Al4V components: state of the art. *Mater Res Expr* 6(1):012002. <https://doi.org/10.1088/2053-1591/aae10e>
- [44] Sanchez S, Smith P, Xu Z, Gaspard G, Hyde CJ, Wits WW, Ashcroft IA, Chen H, Clare AT (2021) Powder bed fusion of nickel-based superalloys: a review. *Int J Mach Tools Manuf* 165:103729. <https://doi.org/10.1016/j.ijmachtools.2021.103729>
- [45] Hosseini E, Popovich VA (2019) A review of mechanical properties of additively manufactured Inconel 718. *Addit Manuf* 30:100877. <https://doi.org/10.1016/j.addma.2019.100877>
- [46] Wang X, Gong X, Chou K (2017) Review on powder-bed laser additive manufacturing of Inconel 718 parts. *Proc Inst Mech Eng B J Eng Manuf* 231(11):1890–1903. <https://doi.org/10.1115/MSEC2015-9322>
- [47] Karia M, Popat M, Sangani K (2017) Selective laser melting of Inconel super alloy-a review. In: *AIP Conference Proceedings*, 1. AIP Publishing LLC, 020013. <https://doi.org/10.1063/1.4990166>
- [48] Zitelli C, Folgarait P, Di Schino A (2019) Laser powder bed fusion of stainless steel grades: a review. *Metals* 9(7):731. <https://doi.org/10.3390/met9070731>
- [49] Ko G, Kim W, Kwon K, Lee T-K (2021) The corrosion of stainless steel made by additive manufacturing: a review. *Metals* 11(3):516. <https://doi.org/10.3390/met11030516>
- [50] Rao BS, Rao TB (2021) Mechanical and tribological properties of 3D printed Al-Si alloys and composites: a review. *Silicon* 1–32. <https://doi.org/10.1007/s12633-021-01340-9>
- [51] Fiocchi J, Tuissi A, Biffi CA (2021) Heat treatment of aluminium alloys produced by laser powder bed fusion: a review. *Mater Des* 204:109651. <https://doi.org/10.1016/j.matdes.2021.109651>
- [52] Michi RA, Plotkowski A, Shyam A, Dehoff RR, Babu SS (2021) Towards high-temperature applications of aluminium alloys enabled by additive manufacturing. *Int Mat Rev* 1–48. <https://doi.org/10.1080/09506608.2021.1951580>
- [53] Aboulkhair NT, Simonelli M, Parry L, Ashcroft I, Tuck C, Hague R (2019) 3D printing of aluminium alloys: additive manufacturing of aluminium alloys using selective laser melting. *Prog Mater Sci* 106:100578. <https://doi.org/10.1016/j.pmatsci.2019.100578>
- [54] Altıparmak SC, Yardley VA, Shi Z, Lin J (2021) Challenges in additive manufacturing of high-strength aluminium alloys and current developments in hybrid additive manufacturing. *Int J Lightweight Mater Manuf* 4(2):246–261. <https://doi.org/10.1016/j.ijlmm.2020.12.004>
- [55] Kotadia HR, Gibbons G, Das A, Howes PD (2021) A review of laser powder bed fusion additive manufacturing of aluminium alloys: microstructure and properties. *Addit Manuf* 46:102155. <https://doi.org/10.1016/j.addma.2021.102155>
- [56] Trevisan F, Calignano F, Lorusso M, Pakkanen J, Aversa A, Ambrosio EP, Lombardi M, Fino P, Manfredi D (2017) On the selective laser melting (SLM) of the AlSi10Mg alloy: process, microstructure, and mechanical properties. *Materials* 10(1):76. <https://doi.org/10.3390/ma10010076>
- [57] Najmon JC, Raeisi S, Tovar A (2019) 2 - Review of additive manufacturing technologies and applications in the aerospace industry. In: Froes F, Boyer R (Eds.) *Additive manufacturing for the aerospace industry*. Elsevier, pp 7–31. doi:<https://doi.org/10.1016/B978-0-12-814062-8.00002-9>
- [58] Cao S, Chu R, Zhou X, Yang K, Jia Q, Lim CVS, Huang A, Wu X (2018) Role of martensite decomposition in tensile properties of selective laser melted Ti-6Al-4V. *J Alloys Compd* 744:357–363. <https://doi.org/10.1016/j.jallcom.2018.02.111>
- [59] Kusano M, Miyazaki S, Watanabe M, Kishimoto S, Bulgarevich DS, Ono Y, Yumoto A (2020) Tensile properties prediction by multiple linear regression analysis for selective laser melted and post heat-treated Ti-6Al-4V with microstructural quantification. *Mater Sci Eng A* 787:139549. <https://doi.org/10.1016/j.msea.2020.139549>
- [60] Sabban R, Bahl S, Chatterjee K, Suwas S (2019) Globularization using heat treatment in additively manufactured Ti-6Al-4V for high strength and toughness. *Acta Mater* 162:239–254. <https://doi.org/10.1016/j.actamat.2018.09.064>
- [61] Yeh A-C, Lu K-W, Kuo C-M, Bor H-Y, Wei C-N (2011) Effect of serrated grain boundaries on the creep property of

- Inconel 718 superalloy. *Mater Sci Eng A* 530:525–529. <https://doi.org/10.1016/j.msea.2011.10.014>
- [62] Zhao X, Chen J, Lin X, Huang W (2008) Study on microstructure and mechanical properties of laser rapid forming Inconel 718. *Mater Sci Eng A* 478(1–2):119–124. <https://doi.org/10.1016/j.msea.2007.05.079>
- [63] Amato KN, Gaytan SM, Murr LE, Martinez E, Shindo PW, Hernandez J, Collins S, Medina F (2012) Microstructures and mechanical behavior of Inconel 718 fabricated by selective laser melting. *Acta Mater* 60(5):2229–2239. <https://doi.org/10.1016/j.actamat.2011.12.032>
- [64] Zhang D, Niu W, Cao X, Liu Z (2015) Effect of standard heat treatment on the microstructure and mechanical properties of selective laser melting manufactured Inconel 718 superalloy. *Mater Sci Eng A* 644:32–40. <https://doi.org/10.1016/j.msea.2015.06.021>
- [65] McGuire MF (2008) *Stainless steels for design engineers*. ASM International
- [66] Salman OO, Gammer C, Chaubey AK, Eckert J, Scudino S (2019) Effect of heat treatment on microstructure and mechanical properties of 316L steel synthesized by selective laser melting. *Mater Sci Eng A* 748:205–212. <https://doi.org/10.1016/j.msea.2019.01.110>
- [67] Rometsch P, Jia Q, Yang KV, Wu X (2019) Aluminum alloys for selective laser melting—towards improved performance. In: *Additive manufacturing for the aerospace industry*. Elsevier, pp 301–325. <https://doi.org/10.1016/B978-0-12-814062-8.00016-9>
- [68] Martin JH, Yahata BD, Hundley JM, Mayer JA, Schaedler TA, Pollock TM (2017) 3D printing of high-strength aluminium alloys. *Nature* 549(7672):365–369. <https://doi.org/10.1038/nature23894>
- [69] Aboulkhair NT, Everitt NM, Maskery I, Ashcroft I, Tuck C (2017) Selective laser melting of aluminum alloys. *MRS Bull* 42(4):311–319. <https://doi.org/10.1557/mrs.2017.63>
- [70] Aboulkhair NT, Maskery I, Tuck C, Ashcroft I, Everitt NM (2016) The microstructure and mechanical properties of selectively laser melted AlSi10Mg: the effect of a conventional T6-like heat treatment. *Mater Sci Eng A* 667:139–146. <https://doi.org/10.1016/j.msea.2016.04.092>
- [71] Yu X, Wang L (2018) T6 heat-treated AlSi10Mg alloys additive-manufactured by selective laser melting. *Procedia Manuf* 15:1701–1707. <https://doi.org/10.1016/j.promfg.2018.07.265>
- [72] Wei P, Chen Z, Zhang S, Fang X, Lu B, Zhang L, Wei Z (2021) Effect of T6 heat treatment on the surface tribological and corrosion properties of AlSi10Mg samples produced by selective laser melting. *Mater Charact* 171:110769. <https://doi.org/10.1016/j.matchar.2020.110769>
- [73] Girelli L, Tocci M, Conte M, Giovanardi R, Veronesi P, Gelfi M, Pola A (2019) Effect of the T6 heat treatment on corrosion behavior of additive manufactured and gravity cast AlSi10Mg alloy. *Mater Corros* 70(10):1808–1816. <https://doi.org/10.1002/maco.201910890>
- [74] Majeed A, Zhang Y, Lv J, Peng T, Atta Z, Ahmed A (2020) Investigation of T4 and T6 heat treatment influences on relative density and porosity of AlSi10Mg alloy components manufactured by SLM. *Comput Ind Eng* 139:106194. <https://doi.org/10.1016/j.cie.2019.106194>
- [75] Kan WH, Nadot Y, Foley M, Ridosz L, Proust G, Cairney JM (2019) Factors that affect the properties of additively-manufactured AlSi10Mg: porosity versus microstructure. *Addit Manuf* 29:100805. <https://doi.org/10.1016/j.addma.2019.100805>
- [76] Tradowsky U, White J, Ward RM, Read N, Reimers W, Attallah MM (2016) Selective laser melting of AlSi10Mg: influence of post-processing on the microstructural and tensile properties development. *Mater Des* 105:212–222. <https://doi.org/10.1016/j.matdes.2016.05.066>
- [77] Bagherifard S, Beretta N, Monti S, Riccio M, Bandini M, Guagliano M (2018) On the fatigue strength enhancement of additive manufactured AlSi10Mg parts by mechanical and thermal post-processing. *Mater Des* 145:28–41. <https://doi.org/10.1016/j.matdes.2018.02.055>
- [78] Maskery I, Aboulkhair N, Tuck C, Wildman R, Ashcroft I, Everitt N, Hague R (2015) Fatigue performance enhancement of selectively laser melted aluminium alloy by heat treatment. In: *26th annual international solid freeform fabrication symposium*, Austin, Texas, USA pp 1017–1025
- [79] Kan WH, Huang S, Man Z, Yang L, Huang A, Chang L, Nadot Y, Cairney JM, Proust G (2021) Effect of T6 treatment on additively-manufactured AlSi10Mg sliding against ceramic and steel. *Wear* 482–483:203961. <https://doi.org/10.1016/j.wear.2021.203961>
- [80] Li W, Li S, Liu J, Zhang A, Zhou Y, Wei Q, Yan C, Shi Y (2016) Effect of heat treatment on AlSi10Mg alloy fabricated by selective laser melting: microstructure evolution, mechanical properties and fracture mechanism. *Mater Sci Eng A* 663:116–125. <https://doi.org/10.1016/j.msea.2016.03.088>
- [81] Wang LF, Sun J, Yu XL, Shi Y, Zhu XG, Cheng LY, Liang HH, Yan B, Guo LJ (2018) Enhancement in mechanical properties of selectively laser-melted AlSi10Mg aluminum alloys by T6-like heat treatment. *Mater Sci Eng A* 734:299–310. <https://doi.org/10.1016/j.msea.2018.07.103>
- [82] Larrosa NO, Wang W, Read N, Loretto MH, Evans C, Carr J, Tradowsky U, Attallah MM, Withers PJ (2018) Linking microstructure and processing defects to mechanical properties of selectively laser melted AlSi10Mg alloy. *Theor*

- Appl Fract Mech 98:123–133. <https://doi.org/10.1016/j.tafmec.2018.09.011>
- [83] Girelli L, Tocci M, Gelfi M, Pola A (2019) Study of heat treatment parameters for additively manufactured AlSi10Mg in comparison with corresponding cast alloy. *Mater Sci Eng A* 739:317–328. <https://doi.org/10.1016/j.msea.2018.10.026>
- [84] Park T-H, Baek M-S, Hyer H, Sohn Y, Lee K-A (2021) Effect of direct aging on the microstructure and tensile properties of AlSi10Mg alloy manufactured by selective laser melting process. *Mater Charact* 176:111113. <https://doi.org/10.1016/j.matchar.2021.111113>
- [85] Rosenthal I, Shneck R, Stern A (2018) Heat treatment effect on the mechanical properties and fracture mechanism in AlSi10Mg fabricated by additive manufacturing selective laser melting process. *Mater Sci Eng A* 729:310–322. <https://doi.org/10.1016/j.msea.2018.05.074>
- [86] Baek M-S, Kreethi R, Park T-H, Sohn Y, Lee K-A (2021) Influence of heat treatment on the high-cycle fatigue properties and fatigue damage mechanism of selective laser melted AlSi10Mg alloy. *Mater Sci Eng A* 819:141486. <https://doi.org/10.1016/j.msea.2021.141486>
- [87] Liu W, Chen C, Shuai S, Zhao R, Liu L, Wang X, Hu T, Xuan W, Li C, Yu J, Wang J, Ren Z (2020) Study of pore defect and mechanical properties in selective laser melted Ti6Al4V alloy based on X-ray computed tomography. *Mater Sci Eng A* 797:139981. <https://doi.org/10.1016/j.msea.2020.139981>
- [88] Panin AV, Kazachenok MS, Panin SV, Berto F (2020) Scale levels of quasi-static and dynamic fracture behavior of Ti-6Al-4V parts built by various additive manufacturing methods. *Theor Appl Fract Mech* 110:102781. <https://doi.org/10.1016/j.tafmec.2020.102781>
- [89] Pal S, Gubeljak N, Hudak R, Lojen G, Rajtukova V, Predan J, Kokol V, Drstvensek I (2019) Tensile properties of selective laser melting products affected by building orientation and energy density. *Mater Sci Eng A* 743:637–647. <https://doi.org/10.1016/j.msea.2018.11.130>
- [90] Stef J, Poulon-Quintin A, Redjaimia A, Ghanbaja J, Ferry O, De Sousa M, Gouné M (2018) Mechanism of porosity formation and influence on mechanical properties in selective laser melting of Ti-6Al-4V parts. *Mater Des* 156:480–493. <https://doi.org/10.1016/j.matdes.2018.06.049>
- [91] Saeidi K, Neikter M, Olsen J, Shen ZJ, Akhtar F (2017) 316L stainless steel designed to withstand intermediate temperature. *Mater Des* 135:1–8. <https://doi.org/10.1016/j.matdes.2017.08.072>
- [92] Laursen CM, DeJong SA, Dickens SM, Exil AN, Susan DF, Carroll JD (2020) Relationship between ductility and the porosity of additively manufactured AlSi10Mg. *Mater Sci Eng A* 795:139922. <https://doi.org/10.1016/j.msea.2020.139922>
- [93] Delahaye J, Tchuindjang JT, Lecomte-Beckers J, Rigo O, Habraken AM, Mertens A (2019) Influence of Si precipitates on fracture mechanisms of AlSi10Mg parts processed by Selective Laser Melting. *Acta Mater* 175:160–170. <https://doi.org/10.1016/j.actamat.2019.06.013>
- [94] Voisin T, Calta NP, Khairallah SA, Forien J-B, Balogh L, Cunningham RW, Rollett AD, Wang YM (2018) Defect-dictated tensile properties of selective laser melted Ti-6Al-4V. *Mater Des* 158:113–126. <https://doi.org/10.1016/j.matdes.2018.08.004>
- [95] Ch SR, Raja A, Nadig P, Jayaganthan R, Vasa NJ (2019) Influence of working environment and built orientation on the tensile properties of selective laser melted AlSi10Mg alloy. *Mater Sci Eng A* 750:141–151. <https://doi.org/10.1016/j.msea.2019.01.103>
- [96] Sun W, Ye Ma, Huang W, Zhang W, Qian X (2020) Effects of build direction on tensile and fatigue performance of selective laser melting Ti6Al4V titanium alloy. *Int J Fatigue* 130:105260. <https://doi.org/10.1016/j.ijfatigue.2019.105260>
- [97] Ren S, Chen Y, Liu T, Qu X (2019) Effect of build orientation on mechanical properties and microstructure of Ti-6Al-4V manufactured by selective laser melting. *Metall Mater Trans A* 50(9):4388–4409. <https://doi.org/10.1007/s11661-019-05322-w>
- [98] Cao S, Chen Z, Lim CVS, Yang K, Jia Q, Jarvis T, Tomus D, Wu X (2017) Defect, microstructure, and mechanical property of Ti-6Al-4V alloy fabricated by high-power selective laser melting. *JOM* 69(12):2684–2692. <https://doi.org/10.1007/s11837-017-2581-6>
- [99] Baghi AD, Nafisi S, Hashemi R, Eborndorff-Heidepriem H, Ghomashchi R (2021) Experimental realisation of build orientation effects on the mechanical properties of truly as-built Ti-6Al-4V SLM parts. *J Manuf Process* 64:140–152. <https://doi.org/10.1016/j.jmapro.2021.01.027>
- [100] Röttger A, Geenen K, Windmann M, Binner F, Theisen W (2016) Comparison of microstructure and mechanical properties of 316L austenitic steel processed by selective laser melting with hot-isostatic pressed and cast material. *Mater Sci Eng A* 678:365–376. <https://doi.org/10.1016/j.msea.2016.10.012>
- [101] Blinn B, Ley M, Buschhorn N, Teutsch R, Beck T (2019) Investigation of the anisotropic fatigue behavior of additively manufactured structures made of AISI 316L with short-time procedures PhyBaLLIT and PhyBaLCHT. *Int J Fatigue* 124:389–399. <https://doi.org/10.1016/j.ijfatigue.2019.03.022>



- [102] Hilaire A, Andrieu E, Wu X (2019) High-temperature mechanical properties of alloy 718 produced by laser powder bed fusion with different processing parameters. *Addit Manuf* 26:147–160. <https://doi.org/10.1016/j.addma.2019.01.012>
- [103] Kaschel FR, Celikin M, Dowling DP (2020) Effects of laser power on geometry, microstructure and mechanical properties of printed Ti-6Al-4V parts. *J Mater Process Technol* 278:116539. <https://doi.org/10.1016/j.jmatprotec.2019.116539>
- [104] Kantzos C, Pauza J, Cunningham R, Narra SP, Beuth J, Rollett A (2019) An investigation of process parameter modifications on additively manufactured inconel 718 parts. *J Mater Eng Perform* 28(2):620–626. <https://doi.org/10.1007/s11665-018-3612-3>
- [105] Mathe NR, Tshabalala LC, Hoosain S, Motibane L, du Plessis A (2021) The effect of porosity on the mechanical properties of Ti-6Al-4V components manufactured by high-power selective laser melting. *Int J Adv Manuf Technol* 115:3589–3597. <https://doi.org/10.1007/s00170-021-0732-6>
- [106] Ronneberg T, Davies CM, Hooper PA (2020) Revealing relationships between porosity, microstructure and mechanical properties of laser powder bed fusion 316L stainless steel through heat treatment. *Mater Des* 189:108481. <https://doi.org/10.1016/j.matdes.2020.108481>
- [107] Choo H, White LP, Xiao X, Sluss CC, Morin D, Garlea E (2021) Deformation and fracture behavior of a laser powder bed fusion processed stainless steel: In situ synchrotron x-ray computed microtomography study. *Addit Manuf* 40:101914. <https://doi.org/10.1016/j.addma.2021.101914>
- [108] Smith BA, Laursen CM, Bartanus J, Carroll JD, Pataky GJ (2021) The interplay of geometric defects and porosity on the mechanical behavior of additively manufactured components. *Exp Mech* 61(4):685–698. <https://doi.org/10.1007/s11340-021-00696-8>
- [109] Zhang K, Kan WH, Liu Y, Gao X, Zhu Y, Lim SCV, Peng H, Huang A (2021) Microstructure control by heat treatment for better ductility and toughness of Ti-6Al-4V produced by laser powder bed fusion. *Aust J Mech Eng* 19(5):680–691. <https://doi.org/10.1080/14484846.2004654>
- [110] Wu M-W, Lai P-H (2016) The positive effect of hot isostatic pressing on improving the anisotropies of bending and impact properties in selective laser melted Ti-6Al-4V alloy. *Mater Sci Eng A* 658:429–438. <https://doi.org/10.1016/j.msea.2016.02.023>
- [111] Yu H, Li F, Wang Z, Zeng X (2019) Fatigue performances of selective laser melted Ti-6Al-4V alloy: influence of surface finishing, hot isostatic pressing and heat treatments. *Int J Fatigue* 120:175–183. <https://doi.org/10.1016/j.ijfatigue.2018.11.019>
- [112] Godec M, Zaefferer S, Podgornik B, Šinko M, Tchernychova E (2020) Quantitative multiscale correlative microstructure analysis of additive manufacturing of stainless steel 316L processed by selective laser melting. *Mater Charact* 160:110074. <https://doi.org/10.1016/j.matchar.2019.110074>
- [113] Chao Q, Thomas S, Birbilis N, Cizek P, Hodgson PD, Fabijanic D (2021) The effect of post-processing heat treatment on the microstructure, residual stress and mechanical properties of selective laser melted 316L stainless steel. *Mater Sci Eng A* 821:141611. <https://doi.org/10.1016/j.msea.2021.141611>
- [114] Leuders S, Lienenke T, Lammers S, Tröster T, Niendorf T (2014) On the fatigue properties of metals manufactured by selective laser melting — The role of ductility. *J Mater Res* 29(17):1911–1919. <https://doi.org/10.1557/jmr.2014.157>
- [115] Seifi M, Salem AA, Satko DP, Grylls R, Lewandowski JJ (2018) Effects of post-processing on microstructure and mechanical properties of SLM-processed IN-718. In: *Proceedings of the 9th international symposium on superalloy 718 & Derivatives: Energy, Aerospace, and Industrial Applications*. Springer, pp 515–526. [https://doi.org/10.1007/978-3-319-89480-5\\_33](https://doi.org/10.1007/978-3-319-89480-5_33)
- [116] Popovich VA, Borisov EV, Popovich AA, Sufiarov VS, Masaylo DV, Alzina L (2017) Impact of heat treatment on mechanical behaviour of Inconel 718 processed with tailored microstructure by selective laser melting. *Mater Des* 131:12–22. <https://doi.org/10.1016/j.matdes.2017.05.065>
- [117] Bagehorn S, Wehr J, Maier HJ (2017) Application of mechanical surface finishing processes for roughness reduction and fatigue improvement of additively manufactured Ti-6Al-4V parts. *Int J Fatigue* 102:135–142. <https://doi.org/10.1016/j.ijfatigue.2017.05.008>
- [118] Mower TM, Long MJ (2016) Mechanical behavior of additive manufactured, powder-bed laser-fused materials. *Mater Sci Eng A* 651:198–213. <https://doi.org/10.1016/j.msea.2015.10.068>
- [119] Andreau O, Pessard E, Koutiri I, Penot J-D, Dupuy C, Saintier N, Peyre P (2019) A competition between the contour and hatching zones on the high cycle fatigue behaviour of a 316L stainless steel: analyzed using X-ray computed tomography. *Mater Sci Eng A* 757:146–159. <https://doi.org/10.1016/j.msea.2019.04.101>
- [120] Hamidi Nasab M, Giussani A, Gastaldi D, Tirelli V, Vedani M (2019) Effect of surface and subsurface defects on fatigue behavior of AlSi10Mg alloy processed by laser powder bed fusion (L-PBF). *Metals* 9(10):1063. <https://doi.org/10.3390/met9101063>

- [121] Aboulkhair NT, Maskery I, Tuck C, Ashcroft I, Everitt NM (2016) Improving the fatigue behaviour of a selectively laser melted aluminium alloy: influence of heat treatment and surface quality. *Mater Des* 104:174–182. <https://doi.org/10.1016/j.matdes.2016.05.041>
- [122] Benedetti M, Torresani E, Leoni M, Fontanari V, Bandini M, Pederzoli C, Potrich C (2017) The effect of post-sintering treatments on the fatigue and biological behavior of Ti-6Al-4V ELI parts made by selective laser melting. *J Mech Behav Biomed Mater* 71:295–306. <https://doi.org/10.1016/j.jmbbm.2017.03.024>
- [123] Benedetti M, Fontanari V, Bandini M, Zanini F, Carmignato S (2018) Low- and high-cycle fatigue resistance of Ti-6Al-4V ELI additively manufactured via selective laser melting: Mean stress and defect sensitivity. *Int J Fatigue* 107:96–109. <https://doi.org/10.1016/j.ijfatigue.2017.10.021>
- [124] Wycisk E, Siddique S, Herzog D, Walther F, Emmelmann C (2015) Fatigue performance of laser additive manufactured Ti-6Al-4V in very high cycle fatigue regime up to  $10^9$  cycles. *Front Mater* 2:72. <https://doi.org/10.3389/fmats.2015.00072>
- [125] Song Z, Gao W, Wang D, Wu Z, Yan M, Huang L, Zhang X (2021) Very-high-cycle fatigue behavior of inconel 718 alloy fabricated by selective laser melting at elevated temperature. *Materials* 14(4):1001. <https://doi.org/10.3390/ma14041001>
- [126] Voloskov B, Evlashin S, Dagesyan S, Abaimov S, Akhatov I, Sergeichev I (2020) Very high cycle fatigue behavior of additively manufactured 316L stainless steel. *Materials* 13(15):3293. <https://doi.org/10.3390/ma13153293>
- [127] Solberg K, Guan S, Razavi SMJ, Welo T, Chan KC, Berto F (2019) Fatigue of additively manufactured 316L stainless steel: the influence of porosity and surface roughness. *Fatigue Fract Eng Mater Struct* 42(9):2043–2052. <https://doi.org/10.1111/ffe.13077>
- [128] Ardi DT, Guowei L, Maharjan N, Mutiargo B, Leng SH, Srinivasan R (2020) Effects of post-processing route on fatigue performance of laser powder bed fusion Inconel 718. *Addit Manuf* 36:101442. <https://doi.org/10.1016/j.addma.2020.101442>
- [129] Xu ZW, Liu A, Wang XS (2019) The influence of building direction on the fatigue crack propagation behavior of Ti6Al4V alloy produced by selective laser melting. *Mater Sci Eng A* 767:138409. <https://doi.org/10.1016/j.msea.2019.138409>
- [130] Xu ZW, Wang Q, Wang XS, Tan CH, Guo MH, Gao PB (2020) High cycle fatigue performance of AlSi10Mg alloy produced by selective laser melting. *Mech Mater* 148:103499. <https://doi.org/10.1016/j.mechmat.2020.103499>
- [131] Bao J, Wu S, Withers PJ, Wu Z, Li F, Fu Y, Sun W (2020) Defect evolution during high temperature tension-tension fatigue of SLM AlSi10Mg alloy by synchrotron tomography. *Mater Sci Eng A* 792:139809. <https://doi.org/10.1016/j.msea.2020.139809>
- [132] Watring DS, Carter KC, Crouse D, Raeymaekers B, Spear AD (2019) Mechanisms driving high-cycle fatigue life of as-built Inconel 718 processed by laser powder bed fusion. *Mater Sci Eng A* 761:137993. <https://doi.org/10.1016/j.msea.2019.06.003>
- [133] Edwards P, Ramulu M (2014) Fatigue performance evaluation of selective laser melted Ti-6Al-4V. *Mater Sci Eng A* 598:327–337. <https://doi.org/10.1016/j.msea.2014.01.041>
- [134] Kumar P, Ramamurty U (2019) Microstructural optimization through heat treatment for enhancing the fracture toughness and fatigue crack growth resistance of selective laser melted Ti6Al4V alloy. *Acta Mater* 169:45–59. <https://doi.org/10.1016/j.actamat.2019.03.003>
- [135] Masuo H, Tanaka Y, Morokoshi S, Yagura H, Uchida T, Yamamoto Y, Murakami Y (2018) Influence of defects, surface roughness and HIP on the fatigue strength of Ti-6Al-4V manufactured by additive manufacturing. *Int J Fatigue* 117:163–179. <https://doi.org/10.1016/j.ijfatigue.2018.07.020>
- [136] Ngnekou JND, Nadot Y, Henaff G, Nicolai J, Ridosz L (2017) Influence of defect size on the fatigue resistance of AlSi10Mg alloy elaborated by selective laser melting (SLM). *Procedia Struct Integr* 7:75–83. <https://doi.org/10.1016/j.prostr.2017.11.063>
- [137] Ngnekou JND, Nadot Y, Henaff G, Nicolai J, Kan WH, Cairney JM, Ridosz L (2019) Fatigue properties of AlSi10Mg produced by additive layer manufacturing. *Int J Fatigue* 119:160–172. <https://doi.org/10.1016/j.ijfatigue.2018.09.029>
- [138] Romano S, Brückner-Foît A, Brandão A, Gumpinger J, Ghidini T, Beretta S (2018) Fatigue properties of AlSi10Mg obtained by additive manufacturing: defect-based modelling and prediction of fatigue strength. *Eng Fract Mech* 187:165–189. <https://doi.org/10.1016/j.engfracmech.2017.11.002>
- [139] Wan HY, Zhou ZJ, Li CP, Chen GF, Zhang GP (2018) Enhancing fatigue strength of selective laser melting-fabricated inconel 718 by tailoring heat treatment route. *Adv Eng Mater* 20(10):1800307. <https://doi.org/10.1002/adem.201800307>
- [140] Luo YW, Zhang B, Li CP, Chen GF, Zhang GP (2019) Detecting void-induced scatter of fatigue life of selective laser melting-fabricated inconel 718 using miniature specimens. *Mater Res Express* 6(4):046549. <https://doi.org/10.1088/2053-1591/aafded>

- [141] Schneller W, Leitner M, Springer S, Grün F, Taschauer M (2019) Effect of HIP treatment on microstructure and fatigue strength of selectively laser melted AlSi10Mg. *J Manuf Mater Process* 3(1):16. <https://doi.org/10.3390/jmmp3010016>
- [142] Di Giovanni MT, de Menezes JTO, Bolelli G, Cerri E, Castrodeza EM (2019) Fatigue crack growth behavior of a selective laser melted AlSi10Mg. *Eng Fract Mech* 217:106564. <https://doi.org/10.1016/j.engfracmech.2019.106564>
- [143] Zhang C, Zhu H, Liao H, Cheng Y, Hu Z, Zeng X (2018) Effect of heat treatments on fatigue property of selective laser melting AlSi10Mg. *Int J Fatigue* 116:513–522. <http://doi.org/10.1016/j.ijfatigue.2018.07.016>
- [144] Bao J, Wu Z, Wu S, Withers PJ, Li F, Ahmed S, Benaarbia A, Sun W (2021) Hot dwell-fatigue behaviour of additively manufactured AlSi10Mg alloy: Relaxation, cyclic softening and fracture mechanisms. *Int J Fatigue* 151:106408. <http://doi.org/10.1016/j.ijfatigue.2021.106408>
- [145] Yan X, Yin S, Chen C, Huang C, Bolot R, Lupoi R, Kuang M, Ma W, Coddet C, Liao H, Liu M (2018) Effect of heat treatment on the phase transformation and mechanical properties of Ti6Al4V fabricated by selective laser melting. *J Alloys Compd* 764:1056–1071. <https://doi.org/10.1016/j.jallcom.2018.06.076>
- [146] Elangeswaran C, Cutolo A, Muralidharan GK, Vanmeensel K, Van Hooreweder B (2020) Microstructural analysis and fatigue crack initiation modelling of additively manufactured 316L after different heat treatments. *Mater Des* 194:108962. <https://doi.org/10.1016/j.matdes.2020.108962>
- [147] Zhang M, Sun C-N, Zhang X, Goh PC, Wei J, Li H, Hardacre D (2017) Competing influence of porosity and microstructure on the fatigue property of laser powder bed fusion stainless steel 316L. In: *Solid freeform fabrication symposium*. University of Texas Austin USA, pp 365–376
- [148] Wu M-W, Lai P-H, Chen J-K (2016) Anisotropy in the impact toughness of selective laser melted Ti–6Al–4V alloy. *Mater Sci Eng A* 650:295–299. <https://doi.org/10.1016/j.msea.2015.10.045>
- [149] Vilardell AM, Fredriksson G, Yadroitsev I, Krakhmalev P (2019) Fracture mechanisms in the as-built and stress-relieved laser powder bed fusion Ti6Al4V ELI alloy. *Opt Laser Technol* 109:608–615. <https://doi.org/10.1016/j.optlste.2018.08.042>
- [150] Park SY, Kim KS, Kim MC, Kassner ME, Lee KA (2020) Effect of post-heat treatment on the tensile and cryogenic impact toughness properties of inconel 718 manufactured by selective laser melting. *Adv Eng Mater* 23(3):2001005. <https://doi.org/10.1002/adem.202001005>
- [151] Girelli L, Giovagnoli M, Tocci M, Pola A, Fortini A, Merlin M, La Vecchia GM (2019) Evaluation of the impact behaviour of AlSi10Mg alloy produced using laser additive manufacturing. *Mater Sci Eng A* 748:38–51. <https://doi.org/10.1016/j.msea.2019.01.078>
- [152] Ardila LC, Garcíandia F, González-Díaz JB, Álvarez P, Echeverría A, Petite MM, Deffley R, Ochoa J (2014) Effect of IN718 recycled powder reuse on properties of parts manufactured by means of selective laser melting. *Phys Procedia* 56:99–107. <https://doi.org/10.1016/j.phpro.2014.08.152>
- [153] Reijonen J, Björkstrand R, Riipinen T, Que Z, Metsä-Kortelainen S, Salmi M (2021) Cross-testing laser powder bed fusion production machines and powders: variability in mechanical properties of heat-treated 316L stainless steel. *Mater Des* 204:109684. <https://doi.org/10.1016/j.matdes.2021.109684>
- [154] Hartunian P, Eshraghi M (2018) Effect of build orientation on the microstructure and mechanical properties of selective laser-melted Ti-6Al-4V alloy. *J Manuf Mater Process* 2(4):69. <https://doi.org/10.3390/jmmp2040069>
- [155] Xu Z, Hyde CJ, Tuck C, Clare AT (2018) Creep behaviour of inconel 718 processed by laser powder bed fusion. *J Mater Process Technol* 256:13–24. <https://doi.org/10.1016/j.jmatprotec.2018.01.040>
- [156] Xu Z, Hyde CJ, Thompson A, Leach RK, Maskery I, Tuck C, Clare AT (2017) Staged thermomechanical testing of nickel superalloys produced by selective laser melting. *Mater Des* 133:520–527. <https://doi.org/10.1016/j.matdes.2017.08.009>
- [157] Bae JH, Yu JM, Lok V, Yoon KB (2021) Effects of processing parameters on creep behavior of 316L stainless steel produced using selective laser melting. *J Mech Sci Technol* 35:3803–3812. <https://doi.org/10.1007/s12206-021-2103-x>
- [158] Amanov A (2021) Advancement of tribological properties of Ti–6Al–4V alloy fabricated by selective laser melting. *Tribol Int* 155:106806. <https://doi.org/10.1016/j.triboint.2020.106806>
- [159] Upadhyay RK, Kumar A (2020) Scratch and wear resistance of additive manufactured 316L stainless steel sample fabricated by laser powder bed fusion technique. *Wear* 458–459:203437. <https://doi.org/10.1016/j.wear.2020.203437>
- [160] Kumar V, Joshi MD, Pruncu C, Singh I, Hosmani SS (2021) Microstructure and tribological response of selective laser melted AISI 316L stainless steel: the role of severe surface deformation. *J Mater Eng Perform* 30:5170–5183. <https://doi.org/10.1007/s11665-021-05730-3>

- [161] Li H, Ramezani M, Chen ZW (2019) Dry sliding wear performance and behaviour of powder bed fusion processed Ti–6Al–4V alloy. *Wear* 440–441:203103. <https://doi.org/10.1016/j.wear.2019.203103>
- [162] Wang Z, Xiao Z, Huang C, Wen L, Zhang W (2017) Influence of ultrasonic surface rolling on microstructure and wear behavior of selective laser melted Ti–6Al–4V alloy. *Materials* 10(10):1203. <https://doi.org/10.3390/ma10101203>
- [163] Sun Y, Moroz A, Alrbaey K (2014) Sliding wear characteristics and corrosion behaviour of selective laser melted 316L stainless steel. *J Mater Eng Perform* 23(2):518–526. <https://doi.org/10.1007/s11665-013-0784-8>
- [164] Huang Y, Yang S, Gu J, Xiong Q, Duan C, Meng X, Fang Y (2020) Microstructure and wear properties of selective laser melting 316L. *Mater Chem Phys* 254:123487. <https://doi.org/10.1016/j.matchemphys.2020.123487>
- [165] Li H, Ramezani M, Li M, Ma C, Wang J (2018) Tribological performance of selective laser melted 316L stainless steel. *Tribol Int* 128:121–129. <https://doi.org/10.1016/j.triboint.2018.07.021>
- [166] Boig CA (2018) The application of additive manufacturing to nickel-base superalloys for turbocharger applications. Ph.D. thesis, University of Sheffield
- [167] Kuo Y-L, Horikawa S, Kakehi K (2017) The effect of interdendritic  $\delta$  phase on the mechanical properties of Alloy 718 built up by additive manufacturing. *Mater Des* 116:411–418. <https://doi.org/10.1016/j.matdes.2016.12.026>
- [168] Trosch T, Ströbner J, Völkl R, Glatzel U (2016) Microstructure and mechanical properties of selective laser melted Inconel 718 compared to forging and casting. *Mater Lett* 164:428–431. <https://doi.org/10.1016/j.matlet.2015.10.136>
- [169] Wang YM, Voisin T, McKeown JT, Ye J, Calta NP, Li Z, Zeng Z, Zhang Y, Chen W, Roehling TT (2018) Additively manufactured hierarchical stainless steels with high strength and ductility. *Nat Mater* 17(1):63–71. <https://doi.org/10.1038/nmat5021>
- [170] Wang X, Sanchez-Mata O, Atabay SE, Muñoz-Lerma JA, Attarian Shandiz M, Brochu M (2021) Crystallographic orientation dependence of Charpy impact behaviours in stainless steel 316L fabricated by laser powder bed fusion. *Addit Manuf* 46:102104. <https://doi.org/10.1016/j.addma.2021.102104>
- [171] Yang T, Liu T, Liao W, MacDonald E, Wei H, Zhang C, Chen X, Zhang K (2020) Laser powder bed fusion of AlSi10Mg: Influence of energy intensities on spatter and porosity evolution, microstructure and mechanical properties. *J Alloys Compd* 849:156300. <https://doi.org/10.1016/j.jallcom.2020.156300>
- [172] Wei P, Wei Z, Chen Z, Du J, He Y, Li J, Zhou Y (2017) The AlSi10Mg samples produced by selective laser melting: single track, densification, microstructure and mechanical behavior. *Appl Surf Sci* 408:38–50. <https://doi.org/10.1016/j.apsusc.2017.02.215>
- [173] Finfrock CB, Exil A, Carroll JD, Deibler L (2018) Effect of hot isostatic pressing and powder feedstock on porosity, microstructure, and mechanical properties of selective laser melted AlSi10Mg. *Metallogr Microstruct Anal* 7(4):443–456. <https://doi.org/10.1007/s13632-018-0456-z>
- [174] Ertuğrul O, Öter ZÇ, Yılmaz MS, Şahin E, Coşkun M, Tarakçı G, Koç E (2020) Effect of HIP process and subsequent heat treatment on microstructure and mechanical properties of direct metal laser sintered AlSi10Mg alloy. *Rapid Prototyp J* 24(1):9–17. <https://doi.org/10.1108/RPJ-04-2016-0068>
- [175] Ali H, Ghadbeigi H, Mumtaz K (2018) Effect of scanning strategies on residual stress and mechanical properties of Selective Laser Melted Ti6Al4V. *Mater Sci Eng A* 712:175–187. <https://doi.org/10.1016/j.msea.2017.11.103>
- [176] Zhang M, Sun C-N, Zhang X, Goh PC, Wei J, Hardacre D, Li H (2017) Fatigue and fracture behaviour of laser powder bed fusion stainless steel 316L: Influence of processing parameters. *Mater Sci Eng A* 703:251–261. <https://doi.org/10.1016/j.msea.2017.07.071>
- [177] Leicht A, Rashidi M, Klement U, Hryha E (2020) Effect of process parameters on the microstructure, tensile strength and productivity of 316L parts produced by laser powder bed fusion. *Mater Charact* 159:110016. <https://doi.org/10.1016/j.matchar.2019.110016>
- [178] Hirata T, Kimura T, Nakamoto T (2020) Effects of hot isostatic pressing and internal porosity on the performance of selective laser melted AlSi10Mg alloys. *Mater Sci Eng A* 772:138713. <https://doi.org/10.1016/j.msea.2019.138713>
- [179] Ferro P, Meneghello R, Razavi SMJ, Berto F, Savio G (2020) Porosity inducing process parameters in selective laser melted AlSi10Mg aluminium alloy. *Phys Mesomech* 23(3):256–262. <https://doi.org/10.1134/S1029959920030108>
- [180] Zhao L, Santos Macias JG, Ding L, Idrissi H, Simar A (2019) Damage mechanisms in selective laser melted AlSi10Mg under as built and different post-treatment conditions. *Mater Sci Eng A* 764:138210. <https://doi.org/10.1016/j.msea.2019.138210>
- [181] Hacısalihoğlu I, Yıldız F, Çelik A (2021) The effects of build orientation and hatch spacing on mechanical properties of medical Ti–6Al–4V alloy manufactured by selective laser melting. *Mater Sci Eng A* 802:140649. <https://doi.org/10.1016/j.msea.2020.140649>
- [182] Röttger A, Boes J, Theisen W, Thiele M, Esen C, Edelmann A, Hellmann R (2020) Microstructure and mechanical



- properties of 316L austenitic stainless steel processed by different SLM devices. *Int J Adv Manuf Technol* 108: 769–783. <https://doi.org/10.1007/s00170-020-05371-1>
- [183] Chen J, Hou W, Wang X, Chu S, Yang Z (2020) Microstructure, porosity and mechanical properties of selective laser melted AlSi10Mg. *Chin J Aeronaut* 33(7):2043–2054. <https://doi.org/10.1016/j.cja.2019.08.017>
- [184] Pei C, Shi D, Yuan H, Li H (2019) Assessment of mechanical properties and fatigue performance of a selective laser melted nickel-base superalloy Inconel 718. *Mater Sci Eng A* 759:278–287. <https://doi.org/10.1016/j.msea.2019.05.007>
- [185] Lee J, Lee M, Jung ID, Choe J, Yu JH, Kim S, Sung H (2020) Correlation between microstructure and tensile properties of STS 316L and Inconel 718 fabricated by selective laser melting (SLM). *J Nanosci Nanotechnol* 20(11):6807–6814. <https://doi.org/10.1166/jnn.2020.18792>
- [186] Schröder J, Mishurova T, Fritsch T, Serrano-Munoz I, Evans A, Sprengel M, Klaus M, Genzel C, Schneider J, Bruno G (2021) On the influence of heat treatment on microstructure and mechanical behavior of laser powder bed fused Inconel 718. *Mater Sci Eng A* 805:140555. <https://doi.org/10.1016/j.msea.2020.140555>
- [187] Tang M, Pistorius PC (2017) Anisotropic mechanical behavior of AlSi10Mg parts produced by selective laser melting. *JOM* 69(3):516–522. <https://doi.org/10.1007/s11837-016-2230-5>
- [188] Wood P, Libura T, Kowalewski ZL, Williams G, Serjouei A (2019) Influences of horizontal and vertical build orientations and Post-Fabrication processes on the fatigue behavior of stainless steel 316L produced by selective laser melting. *Materials* 12(24):4203. <https://doi.org/10.3390/ma12244203>
- [189] Carlton HD, Haboub A, Gallegos GF, Parkinson DY, MacDowell AA (2016) Damage evolution and failure mechanisms in additively manufactured stainless steel. *Mater Sci Eng A* 651:406–414. <https://doi.org/10.1016/j.msea.2015.10.073>
- [190] Zhao X, Li S, Zhang M, Liu Y, Sercombe TB, Wang S, Hao Y, Yang R, Murr LE (2016) Comparison of the microstructures and mechanical properties of Ti–6Al–4V fabricated by selective laser melting and electron beam melting. *Mater Des* 95:21–31. <https://doi.org/10.1016/j.matdes.2015.12.135>
- [191] Greitemeier D, Palm F, Syassen F, Melz T (2017) Fatigue performance of additively manufactured TiAl6V4 using electron and laser beam melting. *Int J Fatigue* 94:211–217. <https://doi.org/10.1016/j.ijfatigue.2016.05.001>
- [192] Günther J, Leuders S, Koppa P, Tröster T, Henkel S, Biermann H, Niendorf T (2018) On the effect of internal channels and surface roughness on the high-cycle fatigue performance of Ti-6Al-4V processed by SLM. *Mater Des* 143:1–11. <https://doi.org/10.1016/j.matdes.2018.01.042>
- [193] de Jesus J, Martins Ferreira JA, Borrego L, Costa JD, Capela C (2021) Fatigue failure from inner surfaces of additive manufactured Ti-6Al-4V components. *Materials* 14(4):737. <https://doi.org/10.3390/ma14040737>
- [194] Kasperovich G, Hausmann J (2015) Improvement of fatigue resistance and ductility of TiAl6V4 processed by selective laser melting. *J Mater Process Technol* 220:202–214. <https://doi.org/10.1016/j.jmatprotec.2015.01.025>
- [195] Chastand V, Quaegebeur P, Maia W, Charkaluk E (2018) Comparative study of fatigue properties of Ti-6Al-4V specimens built by electron beam melting (EBM) and selective laser melting (SLM). *Mater Charact* 143:76–81. <https://doi.org/10.1016/j.matchar.2018.03.028>
- [196] Walker KF, Liu Q, Brandt M (2017) Evaluation of fatigue crack propagation behaviour in Ti-6Al-4V manufactured by selective laser melting. *Int J Fatigue* 104:302–308. <https://doi.org/10.1016/j.ijfatigue.2017.07.014>
- [197] Qian G, Jian Z, Pan X, Berto F (2020) In-situ investigation on fatigue behaviors of Ti-6Al-4V manufactured by selective laser melting. *Int J Fatigue* 133:105424. <https://doi.org/10.1016/j.ijfatigue.2019.105424>
- [198] Kumar P, Ramamurty U (2020) High cycle fatigue in selective laser melted Ti-6Al-4V. *Acta Mater* 194:305–320. <https://doi.org/10.1016/j.actamat.2020.05.041>
- [199] Zhang P, He AN, Liu F, Zhang K, Jiang J, Zhang DZ (2019) Evaluation of low cycle fatigue performance of selective laser melted titanium alloy Ti–6Al–4V. *Metals* 9(10):1041. <https://doi.org/10.3390/met9101041>
- [200] Sheridan L, Scott-Emuakpor OE, George T, Gockel JE (2018) Relating porosity to fatigue failure in additively manufactured alloy 718. *Mater Sci Eng A* 727:170–176. <https://doi.org/10.1016/j.msea.2018.04.075>
- [201] Prithvirajan V, Sangid MD (2018) The role of defects and critical pore size analysis in the fatigue response of additively manufactured IN718 via crystal plasticity. *Mater Des* 150:139–153. <https://doi.org/10.1016/j.matdes.2018.04.022>
- [202] Wan HY, Luo YW, Zhang B, Song ZM, Wang LY, Zhou ZJ, Li CP, Chen GF, Zhang GP (2020) Effects of surface roughness and build thickness on fatigue properties of selective laser melted Inconel 718 at 650 °C. *Int J Fatigue* 137:105654. <https://doi.org/10.1016/j.ijfatigue.2020.105654>
- [203] Periane S, Duchosal A, Vaudreuil S, Chibane H, Morandeau A, Xavier MA, Leroy R (2021) Influence of heat treatment on the fatigue resistance of Inconel 718 fabricated by selective laser melting (SLM). *Mater Today Proc*

- 46(17):7860–7865. <https://doi.org/10.1016/j.matpr.2021.02.447>
- [204] Aydinöz ME, Brenne F, Schaper M, Schaak C, Tillmann W, Nellesen J, Niendorf T (2016) On the microstructural and mechanical properties of post-treated additively manufactured Inconel 718 superalloy under quasi-static and cyclic loading. *Mater Sci Eng A* 669:246–258. <https://doi.org/10.1016/j.msea.2016.05.089>
- [205] Elangeswaran C, Cutolo A, Muralidharan GK, de Formanoir C, Berto F, Vanmeensel K, Van Hooreweder B (2019) Effect of post-treatments on the fatigue behaviour of 316L stainless steel manufactured by laser powder bed fusion. *Int J Fatigue* 123:31–39. <https://doi.org/10.1016/j.ijfatigue.2019.01.013>
- [206] Kumar P, Jayaraj R, Suryawanshi J, Satwik UR, McKinnell J, Ramamurthy U (2020) Fatigue strength of additively manufactured 316L austenitic stainless steel. *Acta Mater* 199:225–239. <https://doi.org/10.1016/j.actamat.2020.08.033>
- [207] Afkhami S, Dabiri M, Piili H, Björk T (2021) Effects of manufacturing parameters and mechanical post-processing on stainless steel 316L processed by laser powder bed fusion. *Mater Sci Eng A* 802:140660. <https://doi.org/10.1016/j.msea.2020.140660>
- [208] Blinn B, Krebs F, Ley M, Teutsch R, Beck T (2020) Determination of the influence of a stress-relief heat treatment and additively manufactured surface on the fatigue behavior of selectively laser melted AISI 316L by using efficient short-time procedures. *Int J Fatigue* 131:105301. <https://doi.org/10.1016/j.ijfatigue.2019.105301>
- [209] Hatami S, Ma T, Vuoristo T, Bertilsson J, Lyckfeldt O (2020) Fatigue strength of 316 L stainless steel manufactured by selective laser melting. *J Mater Eng Perform* 29:3183–3194. <https://doi.org/10.1007/s11665-020-04859-x>
- [210] Zhang M, Sun C-N, Zhang X, Wei J, Hardacre D, Li H (2018) Predictive models for fatigue property of laser powder bed fusion stainless steel 316L. *Mater Des* 145:42–54. <https://doi.org/10.1016/j.matdes.2018.02.054>
- [211] Kunz J, Kaletsch A, Broeckmann C (2016) Influence of HIP post-treatment on the fatigue strength of 316L-steel produced by selective laser melting (SLM). In: European Congress and Exhibition on Powder Metallurgy. European PM conference proceedings. The European Powder Metallurgy Association, pp 1–6
- [212] Shrestha R, Simsiriwong J, Shamsaei N (2019) Fatigue behavior of additive manufactured 316L stainless steel parts: Effects of layer orientation and surface roughness. *Addit Manuf* 28:23–38. <https://doi.org/10.1016/j.addma.2019.04.011>
- [213] Tang M, Pistorius PC (2017) Oxides, porosity and fatigue performance of AlSi10Mg parts produced by selective laser melting. *Int J Fatigue* 94:192–201. <https://doi.org/10.1016/j.ijfatigue.2016.06.002>
- [214] Tang M, Pistorius PC (2019) Fatigue life prediction for AlSi10Mg components produced by selective laser melting. *Int J Fatigue* 125:479–490. <https://doi.org/10.1016/j.ijfatigue.2019.04.015>
- [215] Qian G, Jian Z, Qian Y, Pan X, Ma X, Hong Y (2020) Very-high-cycle fatigue behavior of AlSi10Mg manufactured by selective laser melting: Effect of build orientation and mean stress. *Int J Fatigue* 138:105696. <https://doi.org/10.1016/j.ijfatigue.2020.105696>
- [216] Yan Q, Song B, Shi Y (2020) Comparative study of performance comparison of AlSi10Mg alloy prepared by selective laser melting and casting. *J Mater Sci Technol* 41:199–208. <https://doi.org/10.1016/j.jmst.2019.08.049>
- [217] Beevers E, Brandão AD, Gumpinger J, Gschweidl M, Seyfert C, Hofbauer P, Rohr T, Ghidini T (2018) Fatigue properties and material characteristics of additively manufactured AlSi10Mg – effect of the contour parameter on the microstructure, density, residual stress, roughness and mechanical properties. *Int J Fatigue* 117:148–162. <https://doi.org/10.1016/j.ijfatigue.2018.08.023>
- [218] Brandão AD, Gumpinger J, Gschweidl M, Seyfert C, Hofbauer P, Ghidini T (2017) Fatigue properties of additively manufactured alsi10mg – surface treatment effect. *Procedia Struct Integr* 7:58–66. <https://doi.org/10.1016/j.prostr.2017.11.061>
- [219] Nadot Y, Nadot-Martin C, Kan WH, Boufadene S, Foley M, Cairney J, Proust G, Ridosz L (2020) Predicting the fatigue life of an AlSi10Mg alloy manufactured via laser powder bed fusion by using data from computed tomography. *Addit Manuf* 32:100899. <https://doi.org/10.1016/j.addma.2019.100899>
- [220] Ferro P, Fabrizi A, Berto F, Savio G, Meneghello R, Rosso S (2020) Defects as a root cause of fatigue weakening of additively manufactured AlSi10Mg components. *Theor Appl Fract Mech* 108:102611. <https://doi.org/10.1016/j.tafmec.2020.102611>
- [221] Piette TD, Warren RJ, Spangenberg AG, Hummelt EJ, Lados DA (2021) Microstructure evolution, fatigue crack growth, and ultrasonic fatigue in As-fabricated laser powder bed and conventionally cast Al–10Si–0.4Mg: a mechanistic understanding and integrated flaw-sensitive fatigue design methods. *Mater Sci Eng A* 825:141892. <https://doi.org/10.1016/j.msea.2021.141892>
- [222] Ch SR, Raja A, Jayaganthan R, Vasa NJ, Raghunandan M (2020) Study on the fatigue behaviour of selective laser

- melted AlSi10Mg alloy. *Mater Sci Eng A* 781:139180. <https://doi.org/10.1016/j.msea.2020.139180>
- [223] Wang Z, Wu W, Qian G, Sun L, Li X, Correia JAFO (2019) In-situ SEM investigation on fatigue behaviors of additive manufactured Al-Si10-Mg alloy at elevated temperature. *Eng Fract Mech* 214:149–163. <https://doi.org/10.1016/j.engfracmech.2019.03.040>
- [224] Uzan NE, Shneck R, Yeheskel O, Frage N (2017) Fatigue of AlSi10Mg specimens fabricated by additive manufacturing selective laser melting (AM-SLM). *Mater Sci Eng A* 704:229–237. <https://doi.org/10.1016/j.msea.2017.08.027>
- [225] Uzan NE, Ramati S, Shneck R, Frage N, Yeheskel O (2018) On the effect of shot-peening on fatigue resistance of AlSi10Mg specimens fabricated by additive manufacturing using selective laser melting (AM-SLM). *Addit Manuf* 21:458–464. <https://doi.org/10.1016/j.addma.2018.03.030>
- [226] Santos Macías JG, Elangeswaran C, Zhao L, Van Hooreweder B, Adrien J, Maire E, Buffière J-Y, Ludwig W, Jacques PJ, Simar A (2019) Ductilisation and fatigue life enhancement of selective laser melted AlSi10Mg by friction stir processing. *Scr Mater* 170:124–128. <https://doi.org/10.1016/j.scriptamat.2019.05.044>
- [227] Santos Macías JG, Elangeswaran C, Zhao L, Buffière J-Y, Van Hooreweder B, Simar A (2021) Fatigue crack nucleation and growth in laser powder bed fusion AlSi10Mg under as built and post-treated conditions. *Mater Des* 210:110084. <https://doi.org/10.1016/j.matdes.2021.110084>
- [228] Kumar D, Jhavar S, Arya A, Prashanth K, Suwas S (2021) Mechanisms controlling fracture toughness of additively manufactured stainless steel 316L. *Int J Fract*: 1–18. <https://doi.org/10.1007/s10704-021-00574-3>
- [229] Kuo Y-L, Nagahari T, Kakehi K (2018) The effect of post-processes on the microstructure and creep properties of alloy 718 built up by selective laser melting. *Materials* 11(6): 996. <https://doi.org/10.3390/ma11060996>
- [230] Yoon KB, Dao VH, Yu JM (2020) Effects of build direction on tensile and creep properties of 316L stainless steel produced by selective laser melting. *Fatigue Fract Eng Mater Struct* 43(11):2623–2636. <https://doi.org/10.1111/ffe.13322>
- [231] Dao VH, Yu JM, Yoon KB (2020) Anisotropic creep behavior of stainless steel produced by selective laser melting. *Mater Sci Eng A* 796:140040. <https://doi.org/10.1016/j.msea.2020.140040>
- [232] Yu JM, Dao VH, Yoon KB (2020) Investigation of creep behavior of 316L stainless steel produced by selective laser melting with various processing parameters. *J Mech Sci Technol* 34(8):3249–3259. <https://doi.org/10.1007/s12206-020-0717-z>
- [233] Yu JM, Dao VH, Yoon KB (2020) Effects of scanning speed on creep behaviour of 316L stainless steel produced using selective laser melting. *Fatigue Fract Eng Mater Struct* 43(10):2312–2325. <https://doi.org/10.1111/ffe.13298>
- [234] Read N, Wang W, Essa K, Attallah MM (2015) Selective laser melting of AlSi10Mg alloy: process optimisation and mechanical properties development. *Mater Des* 65:417–424. <https://doi.org/10.1016/j.matdes.2014.09.044>
- [235] Uzan NE, Shneck R, Yeheskel O, Frage N (2018) High-temperature mechanical properties of AlSi10Mg specimens fabricated by additive manufacturing using selective laser melting technologies (AM-SLM). *Addit Manuf* 24:257–263. <https://doi.org/10.1016/j.addma.2018.09.033>
- [236] Zhu Y, Chen X, Zou J, Yang H (2016) Sliding wear of selective laser melting processed Ti6Al4V under boundary lubrication conditions. *Wear* 368–369:485–495. <https://doi.org/10.1016/j.wear.2016.09.020>
- [237] Jia Q, Gu D (2014) Selective laser melting additive manufacturing of Inconel 718 superalloy parts: densification, microstructure and properties. *J Alloys Compd* 585:713–721. <https://doi.org/10.1016/j.jallcom.2013.09.171>
- [238] Zhu Y, Zou J, Chen X, Yang H (2016) Tribology of selective laser melting processed parts: stainless steel 316L under lubricated conditions. *Wear* 350–351:46–55. <https://doi.org/10.1016/j.wear.2016.01.004>
- [239] Tascioglu E, Karabulut Y, Kaynak Y (2020) Influence of heat treatment temperature on the microstructural, mechanical, and wear behavior of 316L stainless steel fabricated by laser powder bed additive manufacturing. *Int J Adv Manuf Technol* 107:1947–1956. <https://doi.org/10.1007/s00170-020-04972-0>
- [240] Amanov A (2020) Effect of local treatment temperature of ultrasonic nanocrystalline surface modification on tribological behavior and corrosion resistance of stainless steel 316L produced by selective laser melting. *Surf Coat Technol* 398:126080. <https://doi.org/10.1016/j.surfcoat.2020.126080>
- [241] Ding H, Tang Q, Zhu Y, Zhang C, Yang H (2020) Cavitation erosion resistance of 316L stainless steel fabricated using selective laser melting. *Friction* 9:1580–1598. <https://doi.org/10.1007/s40544-020-0443-7>
- [242] Laleh M, Hughes AE, Xu W, Gibson I, Tan MY (2019) Unexpected erosion-corrosion behaviour of 316L stainless steel produced by selective laser melting. *Corros Sci* 155:67–74. <https://doi.org/10.1016/j.corsci.2019.04.028>
- [243] Harges C, Pöhl F, Röttger A, Thiele M, Theisen W, Esen C (2019) Cavitation erosion resistance of 316L austenitic steel processed by selective laser melting (SLM). *Addit*

- Manuf 29:100786. <https://doi.org/10.1016/j.addma.2019.100786>
- [244] Azakli Z, Gümruk R (2021) Particle erosion performance of additive manufactured 316L stainless steel materials. *Tribol Lett* 69(4):1–16. <https://doi.org/10.1007/s11249-021-01503-0>
- [245] Talemi R (2020) A numerical study on effects of randomly distributed subsurface hydrogen pores on fretting fatigue behaviour of aluminium AlSi10Mg. *Tribol Int* 142:105997. <https://doi.org/10.1016/j.triboint.2019.105997>
- [246] Zou J, Zhu Y, Pan M, Xie T, Chen X, Yang H (2017) A study on cavitation erosion behavior of AlSi10Mg fabricated by selective laser melting (SLM). *Wear* 376–377:496–506. <https://doi.org/10.1016/j.wear.2016.11.031>

**Publisher's Note** Springer Nature remains neutral with regard to jurisdictional claims in published maps and institutional affiliations.